MEASUREMENT AND ANALYSIS OF SLIPSTREAMS FOR PASSENGER TRAINS

by

NAHIA DEL VALLE

A thesis submitted to The University of Birmingham for the degree of Doctor of Philosophy.

School of Electronic, Electrical and Computer Engineering
University of Birmingham
April 2012

ABSTRACT

This thesis presents a new experimental technique to determine the structure of train slipstreams. The highly turbulent, non stationary nature of slipstreams make their measurement difficult and time consuming as in order to identify the trends of behaviour several passages of the train have to be made. The new technique has been developed in order to minimise considerably the measuring time. It consists of a rotating rail rig to which a 1/50th scale model of a train is attached. Flow velocities are measured using two multi-hole Cobra probes, positioned close to the sides and top of the model. Tests were carried out at different model speeds. Velocity time histories for each configuration were obtained from ensemble averages of the results of a large number of runs (of the order of 80). From these it was possible to define velocity and turbulence intensity contours along the train as well as the displacement thickness of the boundary layer. Wavelet analysis was carried out on the experimental data to reveal details of the unsteady flow structure around the vehicle and obtain information on how the small scale turbulence within the boundary layer region is distributed along the different carriages. The rotating rail rig introduces however some problems such as the high curvature of the rig and subsequent need for a curved train, the existence of an ongoing airflow produced by the movement of the wheel and the train, and the difficulty to align the probes with the main stream of the flow, specially around the nose area, which affects the probe's acceptance rate. Another issue is the considerable difference in Reynolds number between the model scale and full scale tests, which is apparent in the results when comparing full scale and model scale data, especially results showing boundary layer development and wake behaviour. It is concluded that, although this methodology introduces some problems the results obtained with this technique are in good agreement with previous model and full scale measurements.

“I am an old man now, and when I die and go to heaven there are two matters on which I hope for enlightment. One is quantum electrodynamics, and the other is turbulent motion of fluids. And about the former I am rather optimistic”
(Horace Lamb, 1932)

ACKNOWLEDGEMENTS

I would like to acknowledge the School of Electronic, Electrical and Computer Engineering at the University of Birmingham for granting the studentship without which this work would not have been possible.

Special thanks to my principal supervisor Prof Clive Roberts for his supportive, caring and professional attitude, not only during the course of the PhD, but throughout all the years that I spent in Birmingham. I am most grateful for his continuous encouragement and support. I admire his ability to be deeply involved in an innumerable range of projects, without losing his attentiveness to his PhD students and co-workers. There should be a Clive Roberts in every department of the University.

I also want to acknowledge my sincere gratitude to my second supervisor, Prof Christopher Baker. His deep knowledge on fluid mechanics and vehicle aerodynamics has proved a great help in the development of this PhD. The joy and enthusiasm he has for research has been very inspiring. I am very thankful for his attentive guidance, keeping me focused on the objectives of this thesis, for his understanding, his patience, his continuous encouragement (especially with the experiments, when everything seemed to be going wrong) and precious attention. I am also deeply grateful to him for his help and support in presenting a paper for publication. It has been an honour to be his PhD student.

My sincere thanks to Mr Andy Dunn for his technical support and his sense of humour that made looking at a never ending rotating train a joyful experience. I deeply appreciate his willingness to help especially when modifications to the rig had to be done. I am most grateful for his patience, effort and support. It has been a pleasure to work with him.

Thanks as well to Mr Adnan Zentani for the construction of the rig and the train. I appreciate his efforts in modifying the rig when needed.

I would also like to thank Dr Paul Weston and Dr Edward Stewart for providing the position sensor. My deep gratitude for their invaluable suggestions in the experimental part of this investigation, for their kindness, their precious time, and their support. Special thanks to Dr Paul Weston for sharing his knowledge in Matlab coding. My appreciation as well to Dr Andrew Quinn for sharing his knowledge on fluid mechanics and for his valuable comments.

I would also like to express my gratitude to Mr Peter Mousley from Turbulent Flow Instrumentation, for his help and support in dealing with the probes measurements. I am most grateful for his time and patience. His advice proved vital for improving the data acquisition.

My thanks as well to Dr Hassan Hemida for carrying out a CFD simulation of the rotating train slipstream which shed more light on the outcomes of the present investigation.

I am very glad to have spent time at the Railway Research Centre of the University of Birmingham. Many members of it made it an exciting, friendly and inspiring place to work. Special thanks to Mr Rhys Davies, Dr Michael Burrow, Dr Andrew Tobias, Dr Mayorkinos Papaelias and Ms Sharon Berry.

On a personal level, I would like to express my appreciation to all my friends in England and Spain for enduring all my ups and downs and your continuous encouragement and support. To my family and my family in law for your constant love, support and for believing in me. My immense gratitude to my husband Nacho for his tremendous support, especially at the beginning when I spent innumerable weekends at the library whilst he was taking care of the kids. I love you deeply and thank God for having blessed me with your presence. My children Pablo, Maria, Patricia, and the one to be born in November also deserve a huge THANK YOU for helping me to discern what is most important, for your unconditional love and the light you bring into my life.

CONTENTS

LIST OF DEFINITIONS

t Time, normalised with train speed and carriage length
T Time, normalised with train speed and vehicle height
V Train speed
L Vehicle reference length
h Vehicle reference height
u Longitudinal measured velocity from ensemble averages
v_{tot} Overall measured velocity magnitude from ensemble averages
u^+ Dimensionless mean velocity in the inner region of the boundary layer
u_τ Friction velocity
u_e Free stream velocity
y^+ Normalised length normal to the wall
δ Boundary layer thickness
d^* Displacement thickness
ρ Air density
ν Kinematic viscosity of air
μ Dynamic viscosity of air
τ_ω Wall shear stress
k Von Karman constant
B Constant in Logarithmic Law of the wall
U_{pw} Potential velocity
U_i Instantaneous velocity field
$\bar{u}_i$ Mean velocity components from Reynolds decomposition
u'_i Fluctuating velocity components from Reynolds decomposition
P Static pressure
τ_{ij} Viscous stress tensor
S_{ij} Mean strain rate tensor
$-\rho\overline{u_i' u_j'}$ Reynolds stresses
μ_t turbulent eddy viscosity
K Mean turbulent kinetic energy
l_1 Mixing length
l Turbulence length proportional to l_1
Ri Richardson number
R_c Richardson number equivalent for curved flow
R Radius of the streamline
R Radius of curvature
S Curvature parameter of the mean flow
β Turbulence model constant
H Form parameter
θ Momentum thickness
$R_{u_i u_j}$ Shear stress correlation coefficient
x_t Time series in the autoregressive model
ϕ_i Autoregressive model coefficient
a_t White noise term
Re Reynolds number
F Non-dimensional oscillation frequency
St Strouhal number
α,λ Wake parameters
γ Dimensionless eddy viscosity
Cd Vehicle drag coefficient
x_n Time series values in wavelet analysis
n Time localised time index in wavelet analysis
s Scale in wavelet analysis
ψ_0 Wavelet function
ψ Scaled and translated version of the wavelet function
η Morlet wavelet non-dimensional time
w_0 Morlet wavelet wave number
y_{rms} Root mean square value
x Downstream distance
y Length normal to wall or distance from model side
y^* Lateral distance from train centreline
z Distance from train mid height
C_p Pressure coefficient
SD Standard deviation

CHAPTER 1

1. INTRODUCTION

Due to the viscosity of air, a moving train drags the surrounding air with it, resulting in a highly turbulent non-stationary change in the local air velocity. This induced airflow, or slipstream, begins as the head of the train passes and continues all along the train (in the form of a boundary layer) until after the train has passed (the wake) (Temple and Johnson, 2003). The extent of the magnitude of the induced air velocities is highly dependent on the type of train, speed of travel and distance from the train (Pope, 2006). Also pressure variations resulting from the moving train's flow field occur as the head and the tail of the train pass. Although the magnitude of these static pressure pulses are important in terms of the load exerted on structures close to the track, they are thought to occur too quickly to cause a person to lose his balance (Temple and Johnson, 2003). However, any object adjacent to the track, whether a structure or person, will be exposed to the slipstream and hence subjected to a force that is proportional to the square of the slipstream velocity which itself is proportional to the train speed. This poses a safety risk for passengers on platforms and trackside workers, and can cause problems for pushchairs and luggage trolleys on platforms.

1.1 Current UK situation

The Rail Safety & Standards Board (Pope, 2006; Figura-Hardy, 2007) summarized slipstream related incidents in the UK between 1972 and 2005 and found twenty four incidents involving flow induced forces mainly on wheeled items on station platforms (pushchairs, wheelchairs, trolleys) but also on passengers and their belongings. The highest risk comes from a freight train travelling at the upper end of its speed range, being ten times higher than the risk for

passenger trains (Baker et al., 2006). As summarized in Pope (2006) and Figura-Hardy (2007), incidents at platforms were mainly caused by freight trains and incidents at trackside were caused by both freight and passenger trains, as the exposure of the aerodynamically rough under-body produces a significant amount of additional turbulence resulting in higher local velocities and thus reducing differences between freight trains and other train categories (Baker et al., 2006). All these incidents were of low severity. However, on mixed railways, increasing train speeds (such as the new HS2 train in the UK (Rayney, 2011; Department of Transport, 2012), which will run at 350km/h compared to the current high speed train, the Class 390 Pendolino service running at 200km/h) can lead to an increase in passenger journeys (and therefore assumed passenger numbers on station platforms), which can also lead to an increased frequency of incidents at platforms and at trackside (Baker et al., 2006).

1.2 Current test procedures

A number of full scale and model scale tests have been carried out in the UK and elsewhere over recent years to measure the slipstream velocities and determine their effects on the station platform and at the trackside (Pope, 2006; Figura-Hardy, 2007). CEN EN 14067-4 (2009) outlines test procedures for aerodynamics on open track for both model scale and full scale experiments. Material from CEN (2009) has been incorporated into the Technical Specification for Interoperability (TSI, (EU, 2008)) giving limiting values, which are being developed to allow trains to run across national boundaries in the EU.

In this manner, according to the TSI (EU, 2008), for full scale tests, it is required that measurements be made at specific points on a platform and at the trackside for 20 train passes (following CEN (2009)). It is specified that the wind speed should be less than 2 m/s for each train pass, and that the train speed, for platform measurements, must be greater than 90% of the reference speed of 200 kph or of the full operational speed if this is lower than 200 kph

(for trackside tests, the reference speed is taken to be 300 kph). The maximum one second moving average velocity for each train pass is then calculated. From this ensemble of peak values, the mean and the standard deviation are then calculated. The value of the mean plus two standard deviations of the ensemble is then compared with a limiting value specified by the code.

The current EU sponsored project AEROTRAIN (briefly described in Quinn et al. (2011)) focuses on the TSI as a route to harmonise national requirements and converge methods in current European Standards. Specifically it aims at closing "open points" (see Chapter 2, Section 2.2.2 for further details) and reducing the costs and time to obtain the authorisation for new or modified rolling stock to enter service (i.e. reducing the number of measurement locations).

1.3 Current measuring methods

As mentioned above, there are two current approaches to the measurement of train slipstreams, as presented in Sterling et al. (2008), – either at full scale through the use of trackside anemometry at different distances from the train which can measure the three components of wind velocity, or at model scale, i.e. the moving model rig at the TRAIN facility (more details given in Baker, Dalley et al. (2001)) that fires model trains along a tests track, with the slipstream and wake velocities being measured by stationary hot film anemometry close to the track. This type of experimental set up solves the problem of the ground effect introduced in wind tunnel testing, where the relative motion between the vehicles and the ground is not correctly simulated. In principle such tests (at full and model scale) can give all the required information for the assessment of passenger safety etc. However, it is found that in both of these test techniques there is very considerable run to run variability in the data that is measured (as would be expected, since each run will provide one

realisation of a very turbulent flow field) and that to obtain adequate results a number of identical tests need to be carried out (at least 10 and ideally 20) with the results being ensemble averaged to obtain mean and standard deviations of time histories (Johnson et al., 2004; Baker, Dalley et al., 2001). Typical results from Baker, Dalley et al. (2001), obtained with 1/25th scale models on the TRAIN rig owned by DeltaRail in Derby, UK, are shown in Figure 1 for 5 individual runs and their average. The wide variability between individual train passages is apparent, but the ensemble mean can be seen to be well defined. Baker, Dalley et al. (2001) used such experiments to define the different flow regions around high speed trains – the upstream/nose region (for $t<2$), considered as two regions in Baker, Dalley et al. (2001), but as a combined region in what follows; a boundary-layer region ($2\leq t\leq 4$), a near-wake region ($4<t<10$) and a far-wake region ($t\geq 10$), where t is the dimensionless time defined in the figure caption. However, neither full scale nor model scale tests are straightforward to carry out. Clearly at full scale to arrange 10 to 20 passes of an identical train formation is logistically extremely difficult. In addition the ambient conditions should be the same in all tests, which at full scale are impossible to control. At model scale, tests are carried out within a controlled environment, and more runs can be done, but still it is only possible to carry out 8 to 10 runs of the moving model rig (TRAIN facility) each day. In both cases obtaining the same train or model velocity over a number of runs, so that the ensemble average can be calculated is far from straightforward.

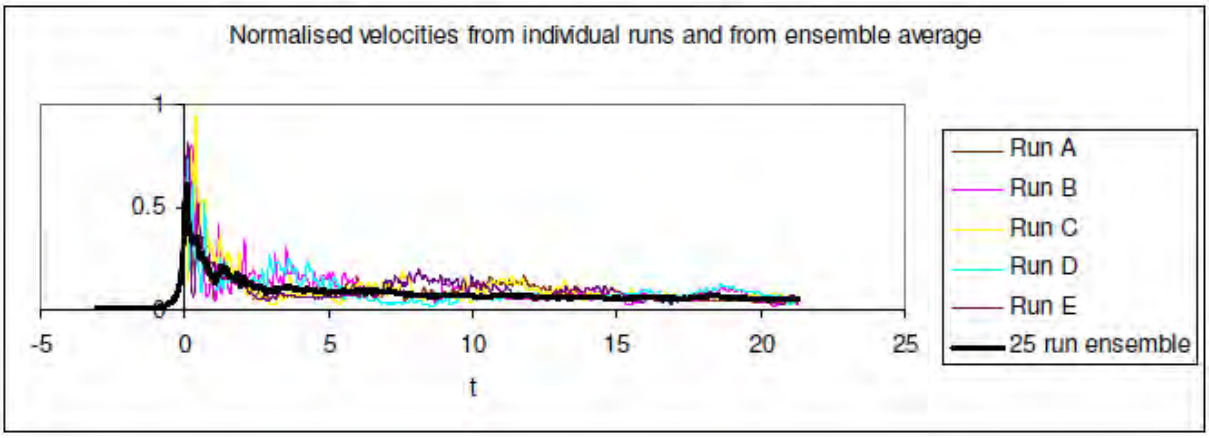

Figure 1. Model scale results for four carriage ICE train from the TRAIN rig from Baker, Dalley et al. (2001). The *x* axis shows time, t, normalised by vehicle velocity and train length, and *y* axis shows slipstream velocity normalized by vehicle velocity. The nose of the train passes at t = 0 and the tail at t = 4.

1.4 New technique: The rotating rail rig.

As shown in Section 1.3, the data obtained for each train type, operating speed and wind condition is usually sparse due to the random behaviour of the flow. Furthermore, the European Standards (Pope, 2006) state that to identify the trends of behaviour at least 20 comparable samples (in terms of train type, speed and wind condition) are required at each measurement point. This implies the spending of a significant amount of money and time on an issue that is not even seen as a major hazard within the overall railway risk in the UK (Baker, Sterling et al., 2006). Therefore, there is a need to obtain this information more rapidly and at a considerably lower cost.

This thesis presents a new technique that uses an experimental set up known as a rotating rail rig that in principle allows such tests to be carried out much more rapidly (see Section 3.1). It consists of a 3.61 m diameter rotating rail rig to which a 1/50th scale model of a four coach train is attached (as in earlier measurements – i.e. the moving model rig) see Figure 2.

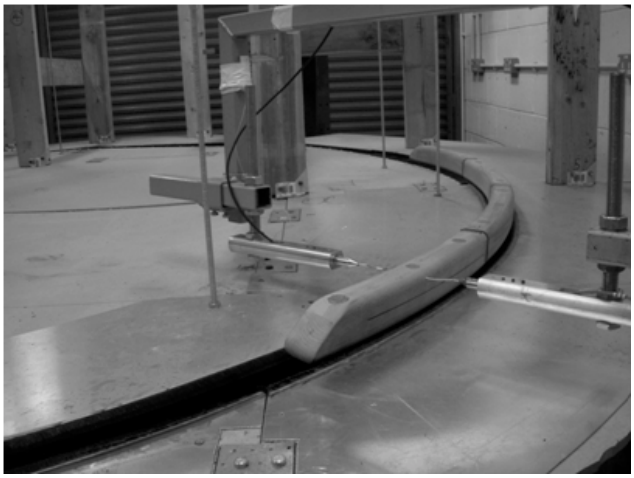

Figure 2. Rotating rail rig and train

Flow velocities are measured using Cobra probes (Turbulent Flow Instrumentation) at different positions from the model sides and top. Tests have been carried out at different model speeds of 7, 9.4, 14.2 and 16.5 m/s, the values being chosen as they were easily available and repeatable on the rig. As can be seen in Figure 2, the train used in the rig is curved. The high curvature of the rig made it extremely difficult to take flow measurements around a straight train, so it was finally decided to use a curved train (see Chapter 3 for further details). Obviously, the rotating rig results will be affected by the curvature of the train, with the boundary layer being thicker on the convex side of the train than in the concave side (as explained in Section 2.1.3). However, on the other hand, the rotating rig introduces a great advantage over the current full scale and model scale techniques: Multiple train passes can be achieved very quickly (one per revolution of the rig) and thus, in principle, experiments can be carried out much more rapidly (i.e. for tests carried out at 16.5m/s, 80 train passes can be achieved in under a minute).

Experiments have been carried out on this rig in order to measure, analyse, study and understand the unsteady flow field induced around the train so that fundamental knowledge on slipstreams could be obtained. However, it would be useful to study further the effects on the results introduced by the curvature of the rig. In this way, a series of CFD calculations

(Computational Fluid Dynamics) have been carried out and validated using the experimental results obtained on the rig (Hemida et al. (2010), attached here in the appendix). The current rig set up, experimental configurations and conditions are described in Chapter 3. The experimental results are shown in Chapter 4. This chapter includes the slipstreams velocity contours along the train, the velocity dependency with train speed and distance of the probe from the train surface, the displacement thickness, turbulence intensities and surface pressure. Wavelet analysis of the different runs is also carried out in this chapter. Chapter 5 includes a comparison of the rig results with existing experimental data on similar ICE-type trains at full scale and model scale. A comparison with CFD (Computational Fluid Dynamics) data is carried out in Chapter 6. Finally, Chapter 7 presents the conclusions and recommendations for further work.

CHAPTER 2

2. BASIC NOTIONS OF THE FLOW FIELD AROUND PASSENGER TRAINS AND ITS ANALYSIS

The highly turbulent non-stationary nature of the induced airflow, or slipstream, resulting from the movement of the train, makes it necessary to look first at the cause of turbulent flows. Existing literature on the flow around trains, data analysis and CFD is then reviewed in order to gain a better understanding of passenger train slipstreams and their analysis. Section 2.1 describes the structure of wall turbulent shear flow (the wall is introduced by the presence of the train) and examines the effect of wall curvature (introduced by the curvature of the train) on the flow. Afterwards, Section 2.2 sets out to investigate the overall flow-field around the train, in terms of the slipstream and wake characteristics. Section 2.3 describes the concept of wavelet transforms and explains why it is found that this is the most appropriate technique to obtain fundamental knowledge on the distribution of the energy of turbulence between the different frequencies that characterise the turbulent flow field around the train. Finally, Section 2.4 reviews the use of Computational Fluid Dynamics (CFD) in the investigation of turbulent flows.

2.1 Turbulent Flow

Hinze (1976) defined turbulent fluid motion as “an irregular condition of flow in which the various quantities show a random variation with time and space coordinates, so that statistically distinct average values can be discerned”.

2.1.1 Wall Turbulent Shear Flow

Hinze (1976) defined wall turbulence as turbulence whose structure is directly influenced by the presence of a solid boundary, which in this case is the train.

Before discussing the description of wall turbulence it is necessary to briefly recall the notion of boundary layer. When defining the boundary layer structure it is usually assumed that the body is stationary and the fluid flows around it. Thus, to comply with the existing literature, the conventional description of the boundary layer development and structure is given in what follows. However it has to be noted that in the present investigation, the opposite situation takes place, as it is the train that moves displacing the air surrounding it. As described in Anderson et al. (2009), the molecules of the fluid moving close to the surface of the body will be affected by viscous forces and shear stresses. At the very surface, friction will attach the fluid molecules to it, creating the no-slip condition. Hence, the fluid presents zero velocity at the wall and then rapidly increases to the free stream velocity, u_e. This layer corresponds with the boundary layer. The thickness of the boundary layer, δ, is normally defined as the distance from the surface where the flow velocity is 99% of the free stream velocity. Boundary layers can be laminar (layered) or turbulent (disordered) depending on the value of the Reynolds number (the ratio of inertial forces to viscous forces), $Re = u_e l/v$, where u_e is the free stream velocity, l is a characteristic length and v is the kinematic viscosity of the fluid. For lower Reynolds numbers, the streamwise velocity changes uniformly (laminar boundary layer) and for higher Reynolds numbers, the flow is characterised by random, three dimensional motions of the particles (turbulent boundary layer).

In the turbulent flow past a rigid body, two regions may be distinguished (Cebeci and Smith, 1974): the inner and the outer regions. The thickness of the inner region is around 10-20% of the entire boundary layer thickness (δ) and can be divided into three layers: a viscous sub-

layer (an extremely thin layer at the wall where the flow is predominantly viscous as the turbulent fluctuations, like mean velocities, become zero at the wall); a buffer region (flow partly viscous, partly turbulent with inertial effects of the order of the viscous effects; this is not a laminar-turbulent boundary layer transition); and a fully turbulent region (where the fluctuations give rise to the so called Reynolds stresses, see below, which dominate over the viscous effects that are now negligible). As stated by Duncan, Thom et al. (1970) in this region a wide spectrum of turbulence frequencies is found, with the larger low frequency eddies further away from the surface. These eddies extract energy from the mean flow passing it to the smaller eddies and the smallest dissipate energy as heat, due to the action of viscosity. The eddy shear stress reaches a maximum in this region; near the surface it is roughly constant and similar to the viscous stress in the viscous sub-layer.

The outer region contains 80% of the boundary layer thickness. As the free stream is approached, the flow at a given point becomes intermittently turbulent and some similarity with free turbulent flow may be expected at that point. Therefore, the shear stress in this region is relatively low.

The velocity profile definition in the inner region varies in the different sub-regions. Thus, in the viscous sub-layer, the dimensionless mean velocity, u^+, distribution is given by the law of the wall (Equation 1) (Hinze, 1974):

$$u^+ = y^+, \quad \text{where} \quad u^+ = \frac{u}{u_\tau}, \quad y^+ = y\frac{u_\tau}{\nu} \quad \text{and} \quad u_\tau = \sqrt{\frac{\tau_\omega}{\rho}} \tag{1}$$

here, u_τ is the friction velocity, y is the length normal to the surface of the body, ρ is the fluid's density, ν is the kinematic viscosity and τ_ω is the wall shear stress for the viscous sub-layer.

In the fully turbulent region the dimensionless mean velocity, u^+, distribution is given by the Logarithmic Law, (Equation 2):

$$u^+ = \frac{1}{k}\ln\left(y^+\right) + B = \frac{1}{k}\ln\left(\frac{yu_\tau}{\nu}\right) + B \tag{2}$$

where k is the Von Karman constant and B is a constant. For a smooth wall, recommended values of the constants k and B are 0.41 and 5 respectively (Anderson et al., 2009).

In the buffer layer, the velocity distribution is neither linear nor logarithmic. Figure 3 shows the different velocity profiles for the inner region of the turbulent boundary layer.

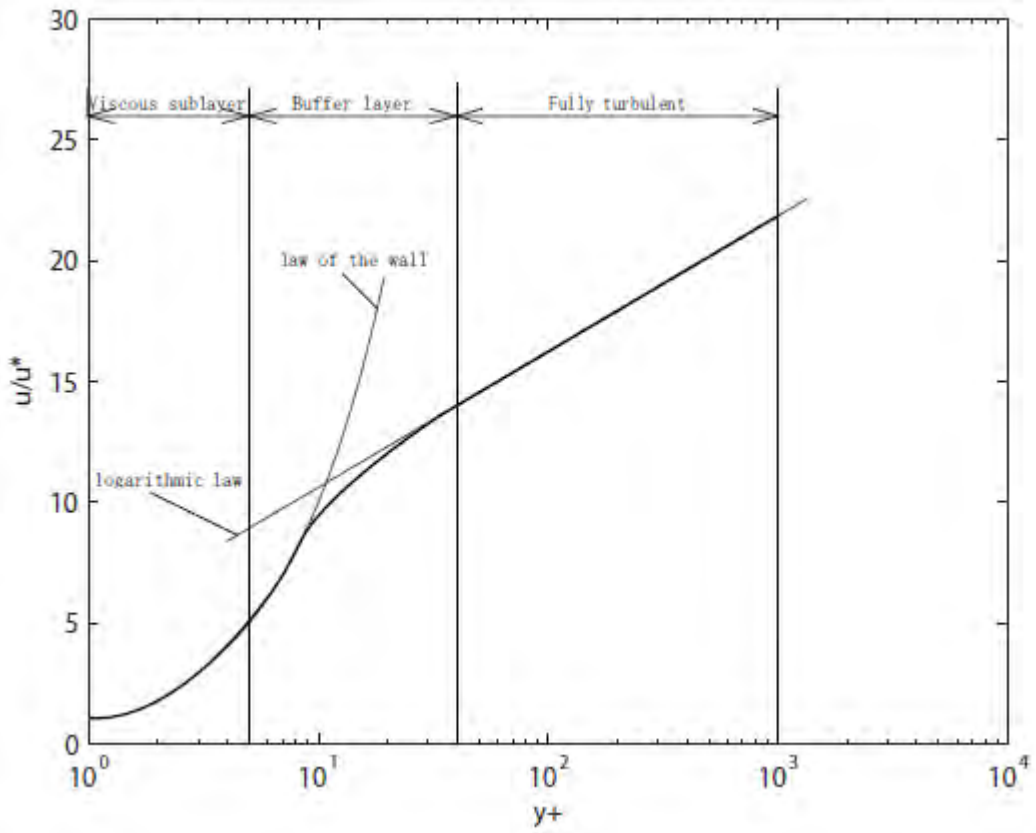

Figure 3. Velocity profiles in the inner region of the turbulent boundary layer (Anderson et al., 2009)]

In the outer region the mean velocity distribution is given by the velocity defect law (Equation 3),

$$\frac{u_e - u}{u_\tau} = f\left(\frac{y}{\delta}\right), \tag{3}$$

where $f(y/\delta)$ is a function to be found empirically and u_e is the velocity in the edge of the boundary layer.

2.1.2 Flow governing equations.

In the present investigation, an incompressible flow (i.e. constant density in response to stress) of a Newtonian fluid (for which the viscous stresses,τ_{ij}, are proportional to the strain rates,ε_{ij}, being the coefficient of viscosity, μ, the constant of proportionality) is considered.

The motion in any realisation of an incompressible turbulent flow is governed by the mass continuity equation (Equation 4) and the momentum conservation equation (Equation 5), also called the Navier-Stokes equations (Pope, 2000). These equations are presented here, in Cartesian tensor notation[1], for a 2D incompressible flow for simplicity:

$$\frac{\partial U_j}{\partial x_j} = 0 \tag{4}$$

$$\rho \frac{DU_i}{Dt} = -\frac{\partial P}{\partial x_i} + \frac{\partial}{\partial x_j}(\tau_{ij}) \rightarrow \frac{\partial U_i}{\partial t} + U_j \frac{\partial (U_i)}{\partial x_j} = -\frac{1}{\rho}\frac{\partial P}{\partial x_i} + \upsilon \frac{\partial^2 U_i}{\partial {x_j}^2} \tag{5}$$

Where $\frac{D}{Dt} = \frac{\partial}{\partial t} + U_i \frac{\partial}{\partial x_i}$ is the total derivative and expresses the total change (expressed in terms of the local change, that would occur in the absence of any motion, and the convective change) of a variable in the Eulerian framework. U_i is the instantaneous velocity field, P is the static pressure, τ_{ij} is the viscous stress tensor, $\tau_{ij}=2\mu S_{ij}$ (for a Newtonian fluid) and S_{ij} is the mean strain rate tensor, $S_{ij} = \frac{1}{2}(\frac{\partial U_i}{\partial x_j} + \frac{\partial U_j}{\partial x_i})$.

The left hand side of Equation 5 shows the change with time of the velocity in a unit volume, and the change due to a divergence in convective transport by the flow through the boundaries

[1] In Cartesian tensor notation, a general vector **x** is defined as **x** =(x_1,x_2,x_3), where x_i is the i^{th} component of **x**. The index i may take any of the values 1,2 or 3. A quantity with two indices (e.g. i and j) is called a tensor and has 9 components (therefore it is a 3X3 matrix). As an example, in the stress tensor t_{ij} , i denotes the surface (perpendicular to x_i) on which the stress acts and j marks the direction of the stress. Tij=[t_{11}, t_{22}, t_{33}; t_{21},t_{22},t_{23}; t_{31},t_{32},t_{33}]

of the control volume[2]. The right hand side of the equation shows the action of the pressure gradient forces on the outside surfaces of the unit control volume, as well as the transfer of momentum per unit mass by molecular effects (which results in a stress). The Navier–Stokes equations are inherently nonlinear, time-dependent and three-dimensional PDEs (Partial Differential Equations).

The above equations (Equations 4 and 5) apply to non-turbulent as well as turbulent flows. In order to show the turbulent motions and their interference with the mean motion, it is possible to carry out the Reynolds decomposition, in which the velocity field can be decomposed into its mean and fluctuation terms (Cebeci and Smith, 1974). In this way, the instantaneous velocity components (U_i) relative to the Cartesian axes (x,y,z) can be described as follows (Equation 6):

$$U_i = \bar{u}_i + u_i'. \tag{6}$$

where, ($\bar{u}_i$) are the mean velocities and (u'_i) are the disturbances, in Cartesian tensor notation.

By substituting Equation 6 into Equation 4 and Equation 5, and taking the average of the terms appearing in the resulting equations (taking into account that the mean of this disturbance is zero, as all the positive values are cancelled by the negative values.), the required equations for turbulent flow are obtained. Thus the final mean continuity and momentum equation, or Reynolds-Averaged Navier-Stokes equations (RANS), are obtained in the following forms (Cebeci and Smith, 1974):

$$\frac{\partial \overline{u_j}}{\partial x_j} = 0 \tag{7}$$

[2] A fixed region in space through which the fluid flows, used to study the masses and energies crossing the boundaries of the region. It is a mathematical abstraction.

$$\frac{\partial \overline{u_i}}{\partial t} + \overline{u}_j \frac{\partial \overline{u_i}}{\partial x_j} = \frac{1}{\rho} \frac{\partial}{\partial x_j} \left[-\overline{P}\delta_{ij} + \mu(\frac{\partial \overline{u_i}}{\partial x_j}) - \rho \overline{u_i' u_j'} \right] \quad (8)$$

It can be seen, that besides the well known terms referring to the mean motion, there occur on the right hand side of Equation 8 additional terms due to the turbulent motion. Comparing Equation 8 with Equation 5 it is possible to conclude that the turbulence terms, $-\rho \overline{u_i' u_j'}$, can be interpreted as stresses on an element of the fluid in addition to the stresses determined by the pressure and the viscous stresses. These turbulence stresses in Equation 8 are called the Reynolds stresses.

As these terms are fluctuation terms that are at present impossible to relate correctly to the dependent variables in the equations, different models to represent them are sought. The most popular models (Duncan, Thom et al., 1970) are the Boussinesq's eddy-viscosity concept (Equation 9) and Prandtl's mixing length theory (Equation 11). Using Boussinesq's theory, the Reynolds stresses caused by random turbulent motions are analogous to the viscous stresses arising from molecular motions. Therefore the transfer of momentum caused by the turbulent eddies is modelled with an effective eddy viscosity, μ_t. Prandtls's theory defines the eddy viscosity in terms of a length scale, l_1, along which a fluid particle will retain its initial values of velocity and vorticity before mixing with the surrounding fluid.

Boussinesq's eddy viscosity model:

$$-\rho \overline{u_i' u_j'} = \mu_t (\frac{\partial \overline{u_i}}{\partial x_j} + \frac{\partial \overline{u_j}}{\partial x_i}) \quad (9)$$

where the positive scalar coefficient μ_t is the turbulent eddy viscosity.

However, this expression implies that for $i=j$ the turbulent velocity is zero (i.e. there is no turbulence!), as for the continuity equation, $\frac{d\overline{u_i}}{dx_i} = 0$. Therefore, this theory is usually expressed substituting the Reynolds stress by the deviatoric Reynolds stress:

$$-\rho\overline{u'_i u'_j} + \frac{2}{3}\rho K\delta_{ij} = \mu_T\left(\frac{d\overline{u_i}}{dx_j} + \frac{d\overline{u_j}}{dx_i}\right) = 2\mu_T S_{ij} \tag{10}$$

where K is the mean turbulent kinetic energy, $K = \frac{1}{2}\overline{u_i' u_i'}$ and $S_{ij} = \frac{1}{2}\left(\frac{d\overline{u_i}}{dx_j} + \frac{d\overline{u_j}}{dx_i}\right)$.

The mixing length theory states:

$$-\rho\overline{u_i' u_j'} = const.\rho l_1^2\left(\frac{d\overline{u_i}}{dx_j}\right)\left|\frac{d\overline{u_i}}{dx_j}\right| \tag{11}$$

The unknown constant can be compounded with the equally unknown l_1^2, so that we have

$$-\rho\overline{u_i' u_j'} = .\rho l^2\left(\frac{d\overline{u_i}}{dx_j}\right)\left|\frac{d\overline{u_i}}{dx_j}\right|, \tag{12}$$

where l is proportional to the mixing length. It can be seen from Equation 11 that $\rho l^2\left|\frac{d\overline{u_i}}{dx_j}\right|$ can be regarded as an effective viscosity coefficient, μ_t. However, the mixing length, l_1, is unknown and must be determined.

The Boussinesq's hypothesis assumes μ_t to be isotropic, which is not strictly true. Only for simple shear flows, in which the mean velocity gradients and turbulence characteristics evolve slowly (following the mean flow), the hypothesis is more reasonable (Pope, 2000). Prandtl's theory assumes that the diffusion and convection of turbulent energy are negligibly small, so that the turbulent energy generated locally is equal to the dissipation, whilst it is shown (Doshi and Gill, 1970) that the diffusion and convection terms in the energy equation are, in general not negligible.

Although neither model bears close examination, they are the starting point for more detailed and comprehensive turbulence models. (Duncan, Thom et al., 1970; Cebeci and Smith, 1974; Hinze, 1975; Pope, 2000).

2.1.3 Curved flow

Turbulent flows along curved surfaces with finite curvature can be classified as complex shear flows due to the appearance of an extra strain rate introduced by the wall curvature (Lakshminarayana, 1986). The streamline curvature in the plane of the mean shear produces large changes in the turbulence structure of shear layers. These changes may be more important in magnitude than normal pressure gradients, property variations, or other explicit effects in the mean motion and the turbulence correlation equations for curved flows.

According to Bradshaw (1969) the effects of curvature on the mixing length or eddy viscosity are appreciable if the ratio boundary layer thickness (δ) - radius of curvature (R) exceeds 1/300. For the model scale tests described in this thesis on a four carriage 1/50th scale ICE2 train model it is expected that δ will be around 40mm. If the rotating rig presents a radius of curvature, R, of around 1800mm, then δ/R=1/45. It thus seems the flow will be affected by curvature.

Bradshaw (1969) stated that if streamlines of the mean flow are appreciably curved, energy may be transferred between the mean flow and the turbulent motion by simple mixing movements, in a way that resembles the transfer of energy by buoyancy forces in stratified flows. This analogy implies that the ordinary Richardson number (minus the ratio of turbulent energy produced by buoyancy forces to that produced by shearing forces), *Ri* (Equation 13), for stratified flow, has as equivalent in curved flow the parameter R_c (Equation 14).

The *Ri* number is defined as follows:

$$Ri = -\frac{g(\partial\rho / \partial y)}{\rho(\partial U / \partial y)^2} \tag{13}$$

where g is the acceleration due to gravity, ρ is density, y is a representative vertical lengthscale and U is velocity.

In curved flows, the ratio of the production of turbulence by centrifugal forces ('buoyant' production) to the 'shear' production is (Bradshaw, 1969):

$$R_c \cong \frac{2\frac{U}{R^2}(\partial(UR)/\partial y)}{(\partial U/\partial y)^2} = 2S(1+S), \tag{14}$$

where R is the radius of the streamline, y the independent variable measured normal to the surface, U is the component of velocity in the circumferential direction and $S = \frac{U}{R}\Big/\frac{\partial U}{\partial y}$ is the curvature parameter of the mean flow.

It is also important to bear in mind that as a result of the curvature of the train the flow field along the concave inner face and along the convex outer face of the train will be different as demonstrated by the tests carried out in blower tunnel rigs and curved channels by So and Mellor (1973); Meroney and Bradshaw (1975); Muck, Hoffmann et al. (1985); Hoffmann, Muck et al. (1985);Barlow and Johnston (1988); Gretler and Baltl (2000) and Kim and Rhode (2000). The same conclusion was achieved in experiments with rotating flows carried out by Taylor (1936); Townsend (1976) and Belotserkovskii (2004). The experiments along convex surfaces showed that the effect of convex curvature on the near wall turbulent flow is to suppress the outward diffusion of the turbulent kinetic energy (stabilizing) while the experiments along concave surfaces showed completely the opposite (destabilizing). It was also found that the wall-shear stress was larger on a concave surface than on a convex surface. These effects will be considered in the following sections.

2.1.3.1 Convex surfaces

A striking effect of convex curvature in a turbulent boundary layer, observed by So and Mellor (1973), was that the shear stress vanishes in a region where the velocity gradient is

still substantial. This seems to support the idea of a critical Richardson number ($R_c \cong 0.3$) beyond which turbulence cannot exist in a convex curved shear flow (So, 1975).

The study for moderate curvature (δ/R~0.01-0.02), developed by Meroney and Bradshaw (1975), supports the above study and adds some other main characteristics of flow along convex surfaces: low rate of boundary layer growth, significant decreases in the turbulence intensities across the boundary layer and therefore decrease in mixing activity. The Logarithmic Law in the inner region of the turbulent boundary layer holds in a modified form (Equation 15, assuming that the velocity profile, *u*, in the inner layer is proportional to $y^{1/5}$) along the surface so that mild curvature effects are reflected and the fact that a small change in curvature (1%) gives rise to a large change (10%) in integral properties (i.e. form Parameter[3], *H*, and momentum thickness[4], θ) of the flow field.

$$u^+[1-(5/3)\beta(y/R)] = \frac{1}{k}\ln\left(y^+\right) + C \tag{15}$$

where β is a constant to be found empirically (usually takes a value between 4 and 5 for concave walls and between 7 and 8 for convex walls (Bradshaw 1969, 1973)).

The work of Meroney and Bradshaw was followed by Muck, Hoffmann et al. (1985), which showed that the effect of stabilising streamline curvature on turbulence structures is mainly a quantitative attenuation in intensity (tends to suppress the growth of turbulent activity (Holloway and Tavoularis, 1991; Gretler and Baltl, 2000)) rather than a qualitative change in large-eddy configuration. Furthermore, this attenuation takes place without producing large

---

[3] $H = \delta^+/\theta$, where δ^+ is the displacement thickness, $\delta^+ = \int_0^\infty \left[1 - \frac{u(y)}{u_e(y)}\right] dy$. See Chapter 4 for further details.

[4] $\theta = \int_0^\infty \frac{u(y)}{u_e(y)}\left[1 - \frac{u(y)}{u_e(y)}\right] dy$, where $u_e(y)$ is the free stream velocity (velocity outside the boundary layer) and $u(y)$ is the measured velocity within the boundary layer.

changes in turbulent structure parameters. In this way, the response of a turbulent boundary layer to a convex curvature is rather fast.

2.1.3.2 Concave surfaces

Taylor (1936); Meroney and Bradshaw (1975); Hoffmann, Muck et al. (1985) and Barlow and Johnston (1988) found that the main characteristics of concave curved shear flow are as follows: the height of the boundary layer is extended by the action of longitudinal rolls in the turbulent boundary layer induced by the concave surface. Mixing across the turbulent boundary layer is enhanced, bringing high momentum fluid closer to the wall (and expelling lower momentum fluid away from the wall), increasing the turbulent energy across the boundary layer and causing a significant increase in skin friction. The shear stress correlation coefficient, $R_{u_i u_j} = \overline{u_i' u_j'} \Big/ (\overline{u_i'^2}\,\overline{u_j'^2})^{1/2}$, remains large for an extended distance from the wall before diminishing. In particular $\tau\omega'/\tau\omega$, the normalised r.m.s. wall shear is the same in the concave and flat cases, despite the strong influence of the large scale roll cells. Finally, the Logarithmic Law of the Wall appears to hold in a modified form (same as above for convex surfaces) when the span wise local friction velocity is used as the velocity scale.

Hoffmann, Muck et al. (1985) confirmed that concave curvature can lead to the quasi-inviscid generation of longitudinal (Taylor-Gortler) vortices (Figure 4 gives a clear idea of the vortex pattern) that wander about preferred lateral positions (flow measurements show clear spanwise variations, as shown in Figure 5) and that significant changes in the turbulence structure are induced both directly by the curvature and indirectly by the vortices (the effect of curvature on the turbulent structure is more important than that of the vortices)

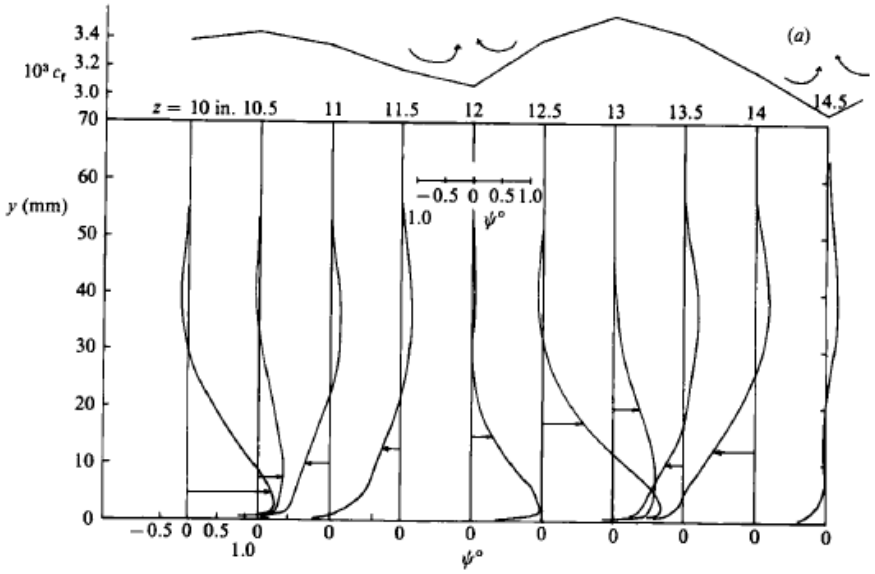

Figure 4. Yaw angle measurements with superimposed skin friction pattern, C_f, for reference. Measurements taken at a certain downstream distance, *x*. *y* is the distance from the wall and *z* is the vertical distance. Here 10 < *z* < 14.5 in. (254 < *z* < 368 mm). (Hoffmann et al. 1985)

a) **b)**

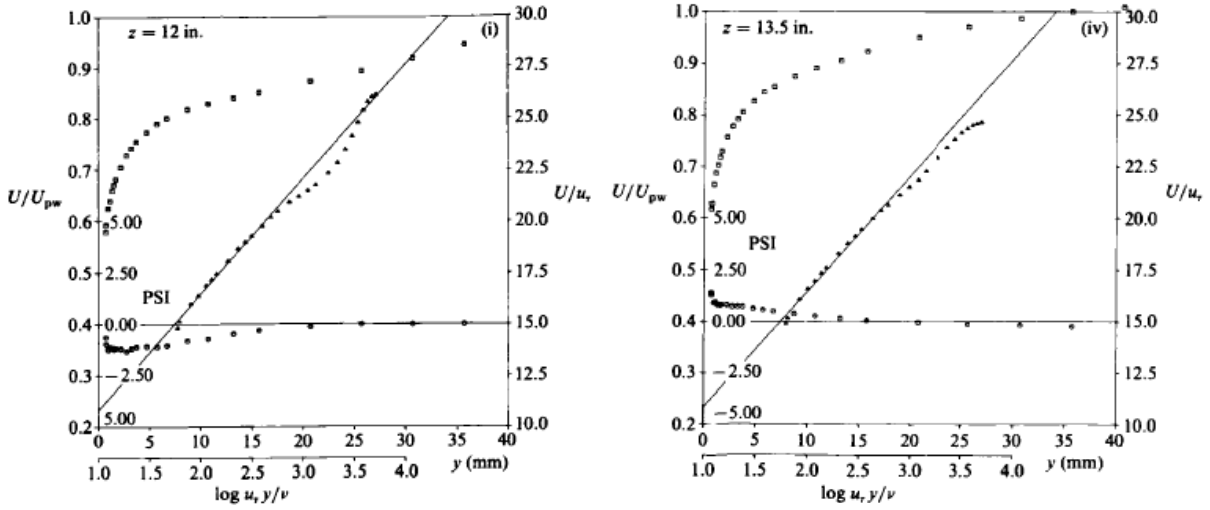

Figure 5. Mean velocity profiles. Inclined line is logarithmic law for a flat surface $u^+ = \frac{1}{0.141}\ln(y^+) + 5.2$. ***$U_{pw}$*, potential velocity; *$u_\tau$*, friction velocity; PSI, yaw angle; □ *U/U_{pw}* vs *y*; △ *U/u_τ* vs *$u_\tau y/\nu$*. (a) *x* = 1050 mm, *z* = 305 mm. (b) *x* = 1050 mm, *z* = 343 mm. (Hoffmann et al. 1985)**

The overall effect of curvature on the mean velocity profile is to reduce the 'wake' component (the deviation from the logarithmic law) because an increase in turbulent mixing

implies a decrease in mean velocity gradient. The response of a turbulent boundary layer to a concave surface is rather slow.

Alternatively, Barlow and Johnston (1988) stated that when the boundary layer entering the curve is free of spanwise non-uniformities (not the case of the above mentioned study where small disturbances were introduced far upstream, in order to fix the vortex structure, so that the primary effect of surface curvature on the turbulent structure could be distinguished from the secondary effects of the vortices) the flow is dominated by large eddies (inflows and outflows) and the effect of longitudinal vortices is small. These large eddies are quite unsteady, have a streamwise extent of only a few boundary layer thicknesses and do not cause significant spanwise variations in the mean properties of the boundary layer.

2.2 Flow around Trains: Slipstream and wake

2.2.1 The Slipstream

The slipstream, or induced airflow that results from the movement of the train in the atmosphere, begins as the head of the train passes and continues until after the tail of the train has passed (the wake). The airflow is predominantly in the direction of train travel, although there are also lateral and vertical components (Temple and Johnson, 2003). As mentioned in Section 1.3, Baker, Dalley et al. (2001) identified a number of different flow regions: the upstream/nose region, where there is a sharp velocity peak and the flow is essentially inviscid and three dimensional with low turbulence levels; a boundary layer region (along the roof and inner and outer sides of the train, reaching equilibrium along the first carriage and growing steadily from there onwards); a near wake region (large flow disturbances); and a far wake region (gradual decrease of velocities). Baker, Sterling et al. (2004) developed a theoretical model of mean flow behaviour of train slipstreams for each of these four regions. The model

considered a potential flow model for the first region, boundary layer theory for the second region, wake decay theory of Eskridge and Hunt (1979) for the fourth region and linear interpolation between the second and fourth region to simulate the third region. In order to simulate also the unsteady behaviour of the slipstream associated with the turbulent nature of the flow (that is, the local variation of the slipstream velocity) an autoregressive model, AR, of the fluctuations was developed. In general an AR model (Equation 16) expresses the current value of time series (i.e. x_t) as a finite, linear sum of a number of previous values of x_t plus a white noise term (with zero mean and finite variance, σ^2_a):

$$x_t = \sum_{i=1}^{p} \phi_i x_{t-i} + a_t \tag{16}$$

Where p is the order of the AR model, ϕ_i is the ith AR coefficient, and a_t is the white noise term (refer to Jordan 2008 for a complete explanation). As explained in Jordan et al. (2009) due to the time varying nature of the slipstream, in order to obtain the AR coefficient values, a process of trial and improvement was carried out. In this manner, the data was analysed in both the time and frequency domain: ensemble average wavelet spectra (see Section 2.3 for a description of wavelet analysis) of the data were compared to that of the simulated data. For full discussion see Jordan (2008).

Sterling, Baker et al. (2008) gather together results from a number of model scale tests carried out by some of the authors (Baker, Dalley et al., 2001) and from full scale tests carried out by Deutsche Bahn, DB, (Schulte-Werning et al., 1999). The different flow regions mentioned above can be easily observed in the ensemble average of slipstream velocity results obtained from both model and full scale tests. Figure 6 shows the ensemble average results obtained at the TRAIN facility for a four carriage 1/25th model scale ICE train, with the measurements being made at half train height for different lateral distances (y) from the side edge of the

train. The *x* axis shows an equivalent full scale value. Figures 7 and 8 show the results of full scale measurements for a 14 carriage ICE service train. Figure 7 shows the results for trackside measurements and Figure 8 shows measurements made above a platform. These figures are similar in form to Figure 6, although clearly the slipstreams extend over a greater distance. In all cases a nose peak and the boundary layer growth can be clearly seen. The trackside measurements, not surprisingly, show greater slipstream velocities than the platform measurements, which reflects the aerodynamically rough nature of the bogies and running gear. Perhaps the most obvious difference between the model scale results of Figure 6 and the full scale results of Figures 7 and 8 is the peak in velocity at the train tail. However, new data considered in Sterling, Baker et al. (2008) has revealed a large ensemble averaged velocity peak in the near wake region that was not apparent in the earlier work reported by Baker, Dalley et al. (2001), at least near the ground or platform surface. Sterling, Baker et al. (2008) show that the individual runs exhibited that this effect may be due to some sort of vortex shedding phenomenon. This intermittency implies that the ensemble averaging technique can be seriously misleading when applied to the near wake region, although the utility of this technique in other flow regions is apparent.

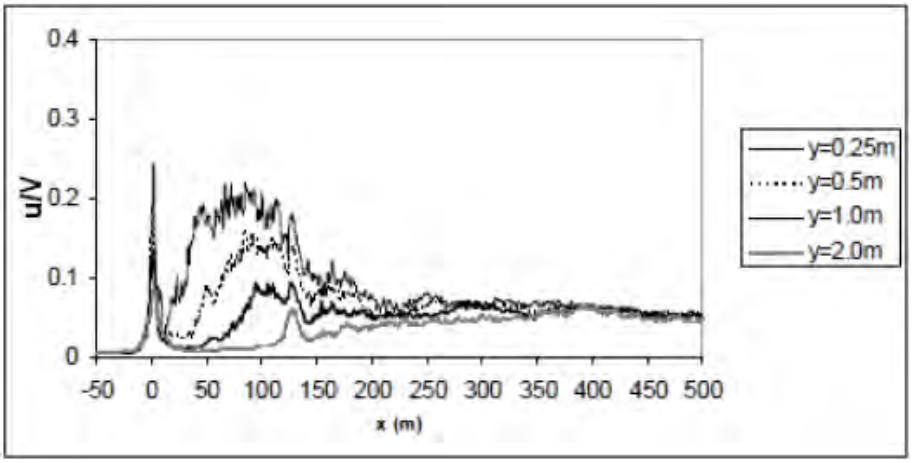

Figure 6. Model scale results for a four carriage ICE train from the TRAIN rig (Baker, dalley et al., 2001; Sterling, Baker et al., 2008). The x axis shows the equivalent full scale distance along the train, and the y axis shows the slipstream velocity u normalised by vehicle velocity V. The nose of train passes at x=0m and the tail of train passes at x= 100m. Measurements were made at half train height and at different lateral distances y from the side edge of the train.

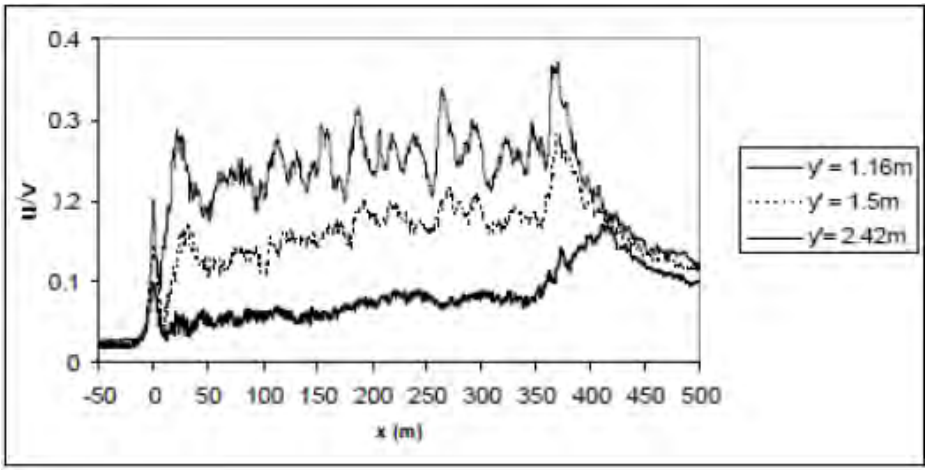

Figure 7.Full scale results for an ICE service train – trackside measurements (from Sterling, Baker et al. 2008). The x axis shows the full scale distance along the train, and the y axis shows slipstream velocity normalised by vehicle velocity. The nose of the train passes at x=0m and the tail of train passes at x= 360 m Measurements were made at a height of 0.5 m above the rail, and at various lateral distances y' from the rail edge.

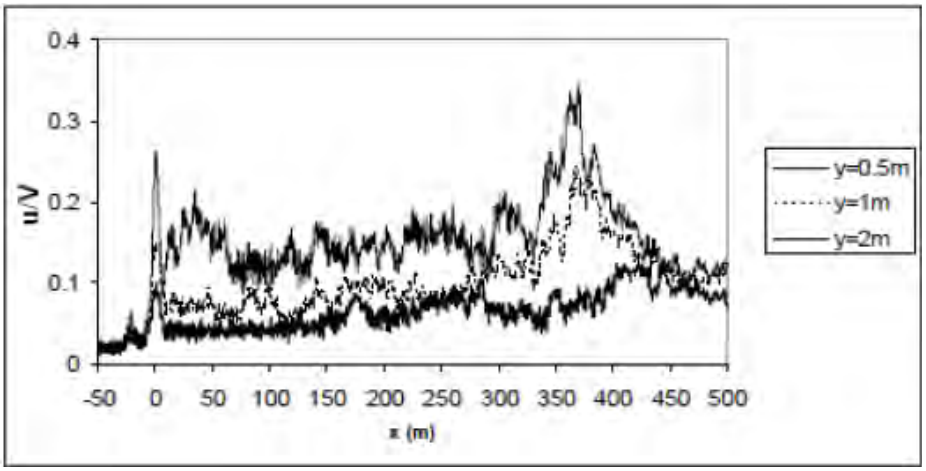

Figure 8. Full scale results for an ICE service train – platform measurements (from Sterling, Baker et al. 2008). The x axis shows the full scale distance along the train, and the y axis shows slipstream velocity normalised by vehicle velocity. The nose of the train passes at x=0 m and the tail of the train passes at x= 360 m. Measurements were made at a height of 1.0m above the platform, and at various lateral distances, y, from the platform side edge.

Such results are the basis on which an assessment can be made of the adequacy or otherwise of the results presented in this thesis. A comparison of model and full scale results with the results of the current investigation is carried out in Chapter 5.

As the train passes, and even for a time after it has passed, a person standing on a platform can experience wind gusts originating from the train. The strength of the slipstream gusts depends mainly on the train speed; distance of the object, or observer, from the train; ambient wind speed and direction, and shape and surface finish of the rolling stock (Pope, 2006).

Therefore, peak gusts may occur at different positions along the train. In general, the highest peaks are found at the trackside where the flow is most influenced by the unshielded wheel sets (Sterling, Baker et al. 2008). Furthermore, the highest slipstream velocities will arise in different regions depending on the train type. Thus for freight trains the largest slipstream velocities are found in the boundary layer zone, while for high-speed passenger trains the largest velocities are generated in the near wake, as found in Sterling, Baker et al. (2008). Baker, Sterling et al. (2006) carried out a review of existing full-scale gust experiments and wind engineering literature on safe wind speeds and concluded that the maximum safe gust speed for pedestrians is around 15m/s. However they found that slipstream velocities of 20 to 25m/s had been measured at designated positions of safety on the railways, and stated that this discrepancy is probably due to the coupled effect of different gust durations (the shorter the gust the higher the wind speed needed to blow a person over) and standing distances of people relative to passing trains (the closer to the train the higher the effect of the gust). Therefore it would seem that the short intense gusts generated by the passage of trains are less dangerous than the longer period gusts due to high wind conditions.

2.2.2 Wake

As mentioned before, the highest slipstream velocities are found in the near wake region for high speed trains. In order to better understand the flow behind the train it is necessary to examine the flow structures of the wake (made up by the near and far wake regions) of the train.

2.2.2.1 Near wake

In the near wake of the flow past bluff bodies, the flow conditions appear to be suitable for the existence of a region of absolute instability leading to regular vortex shedding.

The unsteady flow phenomenon of vortex shedding has been mainly studied behind 2D bluff structures of the type of circular, square and rectangular cylinders (Bearman and Trueman 1972; Griffin 1981; Bearman and Obasaju 1982; Lyn and Rodi 1994; Lyn, Rodi et al. 1995). These 2D tests are not realistic since vortex stretching (the lengthening of vortices in 3D fluid flow, associated with a corresponding increase of the component of vorticity in the stretching direction due to the conservation of angular momentum), the key mechanism of turbulent flows, is neglected here. However, they might be helpful to get a basic perception of the vortex phenomenon. Such is the case of the study carried out by Lyn and Rodi (1994), who developed a phase ensemble averaged study of the unsteady turbulent separated shear flow characteristics around 2D square cylinders and found that the flow comprises of a central shear layer, bounded above by an upper layer where the transition to an irrotational free stream occurs, and bounded below by a high-turbulence-intensity reverse flow region, which is similar to the separated shear layers behind a high speed train model.

In fact three dimensional structures are found in the wake of the flow past two dimensional bluff bodies at Reynolds Numbers of the order of Re=2500. As explained by Bearman (1997) this three dimensionality is characterised by vortex dislocation (it takes place when there is a spanwise variation in the frequency of vortex shedding and it is a means by which vortices of similar signs can connect with each other at a boundary between cells with different shedding frequencies), vortex looping (a vortex joins with one or more vortices of opposite sign on the other side of the wake) and oblique vortex shedding (vortices are shed at a small angle to the vehicle axis). At this Reynolds number, three-dimensionality is also related to shear layer instability and three dimensional motions associated with turbulence generated past the bluff body. However, the wake of a two dimensional bluff body is often dominated by transverse

vortices whilst the wake of a three dimensional body is dominated by streamwise vortices (Bearman 1997).

Results on a passenger car presented by Bearman (1997) show that the near wake flow consisted of a large number of unsteady longitudinal vortex structures and weak transverse ones which were shed regularly from the base.

Similar regions of instability may occur behind many complex three dimensional bluff body shapes, including a passenger train. In fact, in the slipstream study by Sterling, Baker et al. (2007), for both full scale and model scale ICE passenger trains, the measured slipstream velocity peaks showed an intermittent structure. This intermittency is consistent with some sort of periodic structure being shed from the rear of the vehicle and moving downstream (shedding is induced by a mismatch in the entrainment of fluid by the shear-layer and the re-injection of fluid from the reattachment zone). Therefore, measurements of the near wake velocities depend on the stage in the shedding cycle that the flow is undergoing at that instant. This run to run variability makes the ensemble averaging technique in the near wake seriously misleading. This is also observed by Gilhome, Saunders et al. (2001) who noted that large scale shedding of vortices usually results in shear-layer flapping, which explains why CFD (turbulence models generally solve mean flow fields, see Section 2.4 below) and time-averaged results on this region should be treated with caution.

Baker (2001) states that the near wake in a high speed train model is characterised by a large scale flow recirculation immediately behind the vehicle bounded by separated shear layers form the model surface. Longitudinal unsteady trailing vortex structures moving away from the train centre line are also found in this region. These vortices originate from various features of the upstream body and may interact with each other around the body and in the near wake. These unsteady flow mechanisms can be discerned at a variety of frequencies. In

this way, Baker shows that the separated shear layers from the train surface have a characteristic non-dimensional oscillation frequency $F = fh/V$ (where h is the height of the train, V is the vehicle speed and f is the frequency of the fluctuations) of around 0.5, within wide limits (this also holds true for other ground vehicles at model scale, such as lorries (Baker, 2001) and fastback cars (Bearman, 1997)). This oscillation decays along the wake, and a lower frequency F of around 0.03 becomes dominant (in the case of lorries, F is around 0.05). This is associated with a characteristic frequency of the entire wake structure (for different types of ground vehicles: trains, lorries and fastback cars).

To come to a clear understanding of the train wake flow phenomena, Schulte-Werning, Heine et al. (2003) showed results of the EU-funded research project RAPIDE for an ICE2 power car running in trailing position at up to 280 km/h for 1:1 scale conditions with Re 10^7. The authors used conventional unsteady RANS CFD techniques to study the forces on the tail cars of high speed trains and identified a steady near wake oscillation with the shedding of longitudinal vorticity from low levels in the rear of the train (see Figure 9). A well defined oscillation was found at a Strouhal[5] number of 0.14.

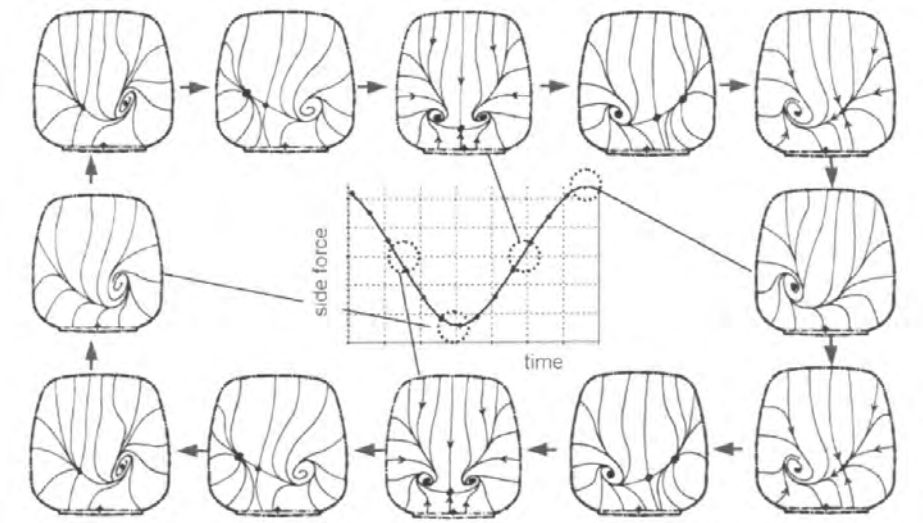

Figure 9. Cycle of the vortex shedding on the surface of the ICE trailing car. (Schulte-Werning, Heine et al., 2003)

[5] The Strouhal number is a dimensionless number describing oscillating flow mechanisms. $St=fL/V$. where f is the frequency of vortex shedding, L is the characteristic length and V is the velocity of the fluid

Sterling, Baker et al. (2008), after reviewing different full and model scale high speed train measurements and wake results, indicated the complexity of the wake flow, with the major unsteadiness at Strouhal numbers of 0.1-0.15 being dominant close to the ground, with other flow mechanism being significantly higher above the ground (0.5-1 in the case of the scale models for measurements at train mid height).

2.2.2.2 Far wake

The far wake is the region long after the train has passed. The flow is still disturbed by the passing train, but not as severely as in the near wake. As mentioned by Baker (2001), the far wake is defined by a gradual decay in wake ensemble–averaged velocities and standard deviations. It is important to note that whilst velocity measurements made nearest the train decay steadily, measurements made furthest away first increase and then decrease, showing the lateral spread of the wake (Baker, 2010). This effect can be seen in Figure 10 below, for model scale wake measurements on a 1/25th scale ICE2 train (Baker, Dalley et al., 2001). The *x* axis is defined as a dimensionless time, $T = tV/h$, where t is the time since the rear of the vehicle passed the measurement point, V is the train speed and h is vehicle height.

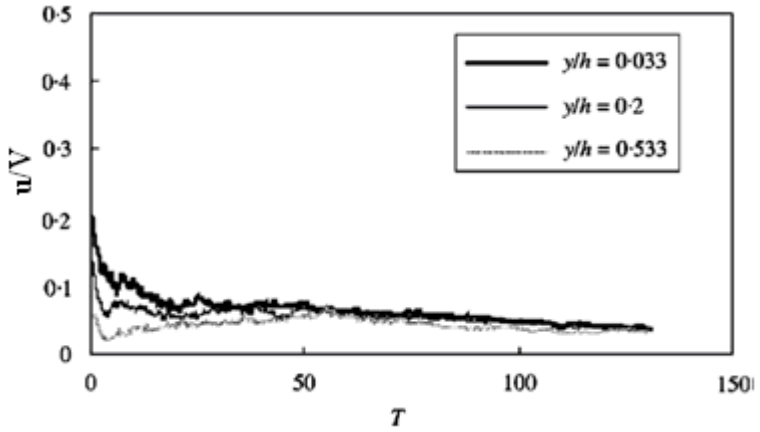

Figure 10. Wake measurements of a 1/25th scale ICE model (*y* is the distance from the train side, *h* is the train height) (Baker, Dalley et al., 2001)

In this region there is no sign of any instability due to the shear layer fluctuations and the majority of the fluctuating energy is at scales associated with an overall instability of the vehicle wake. The lower frequency oscillation is either associated with the mechanism of wake pumping, or with large-scale instability of the complete wake structure (Baker, 2001; Baker, 2010).

Eskridge and Hunt (1979) developed a self similarity theory[6] for the velocity deficit and turbulent energy fluctuations in the wake of vehicles. Later on, Eskridge and Thompson (1982) improved this wake theory, accounting for different length scales in the lateral and vertical directions (the same length scale was used in the previous theory) and using a non-constant eddy viscosity. However, Baker (2001) found that the mean velocity profiles could be reasonably represented by the self preserving solution of Eskridge and Hunt, as long as appropriate constants were selected. In this way, Baker (2001) developed a model for the longitudinal, lateral and vertical velocities in this decaying wake. The expressions for the velocities (Equations 17 and 18) were simple algebraic functions governed by two parameters of the distance along and across the wake:

$$U = \alpha \frac{Z}{T} \exp[-\lambda \frac{Y^2 + Z^2}{T^{0.5}}],\ V = \frac{\alpha}{2} \frac{YZ}{T^2} \exp[-\lambda \frac{Y^2 + Z^2}{T^{0.5}}] \tag{17}$$

$$W = \frac{\alpha}{2} \frac{YZ^2}{T^2} \exp[-\lambda \frac{Y^2 + Z^2}{T^{0.5}}] \tag{18}$$

[6] According to Hinze (1975) self preservation indicates that the turbulence maintains its structures during the development of the turbulent region in the downstream direction of the main flow. In this manner, similarity of mean-velocity profiles in successive sections of the wake flow can be found in the downstream direction when these velocities are expressed in dimensionless form via a velocity scale (i.e. the maximum mean-velocity difference). Lateral distances are also made dimensionless with the local width of the turbulent region as a scale.

Here U, V and W are respectively the dimensionless wake velocities in the longitudinal, lateral and vertical directions. α is given by $1/\gamma$, where γ is the dimensionless eddy viscosity, and λ is given by $1.61/\gamma^{0.5}\, C_D^{0.5}$ for a vehicle with its height equal to its width, where C_D is the vehicle drag coefficient. By fitting equation 17 to the measured slipstream data, it is possible to obtain the best fit values of α and λ.

Figure 11 shows the best fit curves to the model scale ICE data. The model data is the effective dimensionless velocity measured by the hot wire probes at the side of the vehicle, which correspond with the vector sum of U (the velocity in the vehicle direction of travel) and V (the velocity normal to the direction of travel). The agreement can be seen to be good, and suggests that the wake velocities are self similar when expressed in a suitably dimensionless format.

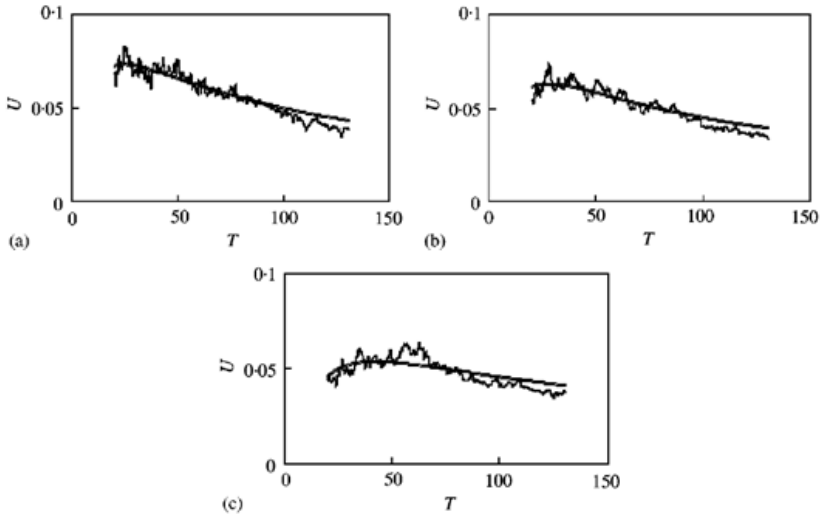

Figure 11. Best fit curves to wake velocities using the model of Baker (2001). (a) *y/h* = 0.033, (b) *y/h* = 0.2, (c) *y/h*= 0.533 (Baker, 2010)

2.2.3 Aerotrain Project

As mentioned in the Introduction, the current European AEROTRAIN project focuses on the Technical Specifications for Interoperability as a route to harmonise national requirements and converge methods in current European Standards. Specifically it aims at closing "open

points" and reducing the costs and time to obtain the authorisation for new or modified rolling stock to enter service.

The “open points” found in the TSI are briefly touched upon by Sterling, Baker et al. (2008). Firstly, there is the question as to whether the ensemble of one second maxima always contains samples taken from one region of the flow around the train (ideally the near wake region for high speed passenger trains) such that these samples can be considered to be part of the same statistical sample; secondly there is the question of whether a one second averaging time is wholly appropriate when determining whether or not a slipstream reaches dangerous levels as shorter period gusts of considerable energy (Jordan et al., 2009) could be filtered out; and thirdly, there is a concern that slipstream velocities may be significantly affected by ambient winds, an issue that is addressed by Quinn et al. (2011).

AEROTRAIN has five technical work packages concerned with open air pressure transients, aerodynamic loads on the track, cross wind effects on trains, pressure transients in tunnels, and train slipstreams. The work in the slipstreams work package involves the following aspects, as described by Quinn et al (2011).

- The collation of existing slipstream data from earlier projects – specifically material from UK tests carried out in the 1980s and 1990s (Figura-Hardy, 2007), and material from the RAPIDE project (Schulte-Werning et al., 1999, reported in Sterling, Baker et al., 2008).
- Measurement campaigns on lines in Spain and Germany, to measure the slipstreams for a variety of high speed train and conventional train types.
- The analysis of the data to determine a possible revised TSI methodology, i.e. to identify the magnitudes of slipstreams from different vehicles.

- The derivation of a methodology to assess single vehicles within trains with respect to their relevance / impact on the slipstream effects of a train set up.

When complete the AEROTRAIN project will provide data on which revisions to the current CEN / TSI methodology can be based, which will result in a simplification of the authorisation procedure for new trains and for single vehicles.

2.3 Data Analysis

Hinze (1975) states that a turbulent motion is composed of various sized eddies that have a certain kinetic energy, determined by their vorticity or by the intensity of the velocity fluctuation of the corresponding frequency. In fact, the smaller the eddy, the greater in general the velocity gradient in the eddy and the greater the viscous shear stress that counteracts the eddying motion. Thus, in each turbulent flow, there is a statistical lower limit to the size of the smallest eddy; there is a minimum scale of turbulence that corresponds to a maximum frequency in the turbulent motion. A question which arises is how the energy of turbulence will be distributed between the frequencies. Such a distribution is usually called an energy spectrum.

In order to establish the frequency content of the spectrum (to determine both the dominant modes of variability and how these modes vary in time), instead of applying the normal Fourier Transform (FT) to the turbulence components, Wavelet Analysis is used in the analysis of the present results obtained in the rotating rail rig.

2.3.1 Wavelet Analysis vs. Fourier Transform

A FT provides the spectral content of the signal, but it gives no information regarding where in time those spectral components appear. Therefore, a FT is not a suitable technique for non-stationary signals. As mentioned previously the slipstreams are related to a highly turbulent

non stationary flow field and thus a FT does not seem very adequate. Furthermore, it relies on the assumption that the signal can be decomposed into sinusoidal components (periodic signals), which is not the case in the present investigation. Even the WFT (Windowed Fourier Transform) which enables the Fast Fourier Transform to be computed at each time using only the data within a window, cannot be applied. The main problem with the WFT is that at low frequencies there are so few oscillations within the window that the frequency location is lost, and at high frequencies there are so many oscillations that the time localisation is lost (Torrence and Compo, 1998).

Wavelet analysis solves these problems by decomposing a time-series into time/frequency space simultaneously.

2.3.2 Wavelet transform

The wavelet transform is an inner product (or convolution) between an analysing wavelet at a given scale, s, and the signal to be analysed; therefore the wavelet coefficients combine information about both the signal and the wavelet. As shown in Valens (2004), in wavelet analysis a fully scalable modulated window is shifted along the signal and for every position the spectrum is calculated. In this manner, if the signal has a major component of the frequency corresponding to the current scale, then the wavelet transform coefficient computed at this point in the time-scale plane will be a relatively large number. This process is repeated many times with a slightly shorter (or longer) window for every new cycle. In the end the result will be a collection of time-scale representations of the signal (the scale being in a way the opposite of frequency), all with different resolutions (higher frequencies are better resolved in time, and lower frequencies are better resolved in frequency (Polikar, 2001).

Wavelet transforms are broadly classified into the discrete wavelet transform (DWT) and the continuous wavelet transform (CWT). The principal difference between the two is the

continuous transform operates over every possible scale and translation whereas the discrete uses a specific subset of all scale and translation values. Following Farge (1992), for analysing purposes the continuous wavelet transform is better suited because its redundancy (given that the scaled functions that are shifted over the signal do not form an orthogonal basis) allows good legibility of the information content of the signal. For compression or modelling purposes, the orthogonal wavelet transform or the newly developed wavelet packet technique, are preferable because they decompose the signal into a minimal number of independent coefficients.

The CWT was used by Torrence and Compo (1998) to analyse the El Niño-Southern Oscillation (ENSO) with excellent results and good statistical significance. They also developed a program (Torrence and Compo, n.d.) to calculate the continuous wavelet transform that was used later on by Baker, Dalley et al. (2001) to analyse the turbulent flow field around a $1/25^{th}$ scale ICE train model and also by Baker (2001) to study ground vehicle wakes. Results from the last two experiments will be compared with results from the present investigation (Chapter 5). Therefore, only the CWT will be the focus of this investigation. For details on the DWT, please refer to (Farge, 1992; Valens, 2004; and Polikar, 2001).

2.3.3 The Continuous Wavelet Transform

The continuous wavelet transform of a time series, X, (with values of x_n, at time index n and each value separated in time by a constant time interval δt) is defined as the convolution of x_n (Equation 19) with a scaled and translated version, ψ (Equation 21), of the wavelet function, ψ_0 (Equation 20).

$$W_n(s) = \sum_{n'=0}^{N-1} x_n \psi * \left[\frac{(n'-n)\delta t}{s} \right] \tag{19}$$

where (*) indicates the complex conjugate. By varying the wavelet scale, s, and translating along the localised time index, n, it is possible to create a picture showing both the amplitude of any features versus the scale and how this amplitude varies with time.

To be called a "wavelet" the analysing function has to satisfy the admissibility condition, which for an integrable function means that its average should be zero (Farge, 1992).

As detailed in Section 4.5, in the current investigation, the complex valued Morlet wavelet function, ψ_0 (Equation 19), is used. It consists of a plane wave modulated by a Gaussian envelope of unit width (Figure 12).

$$\psi_0(\eta) = \pi^{-1/4} e^{iw_0\eta} e^{-\eta^2/2} \tag{20}$$

Where ψ_0 is the wavelet value at non-dimensional time η, and w_0 is wave number, which gives the number of oscillations within the wavelet itself. The Morlet wavelet is only marginally admissible because it is of zero average only if very small correction terms are added. In practice, if $w_0 = 6$ is chosen, then the correction terms become unnecessary because they are of the same order as the typical computer round off errors (as explained by Farge (1992)).

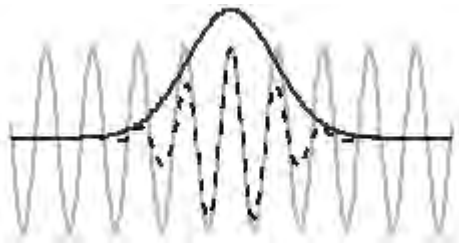

Figure 12. Morlet wavelet (black dashed) created from a Sine curve (gray) multiplied by a Gaussian envelope (black) (Torrence and Compo, 1998)

This wavelet function is also called the Mother wavelet as it is from this one that the scaled and translated wavelets, ψ, are defined (Equation 21):

$$\psi\left[\frac{(n'-n)\delta t}{s}\right] = \left(\frac{\delta t}{s}\right)^{1/2} \psi_0\left[\frac{(n'-n)\delta t}{s}\right] \quad (21)$$

In this equation, the factor $s^{-1/2}$ follows energy normalisation purposes so that the transformed signal has the same energy at every scale. As can be seen in Equation21, the scaling term, *s*, is used in the denominator, and therefore, scales $s > 1$ (low *f*) dilate the Mother wavelet, whereas scales $s < 1$ (high *f*) compress it.

As mentioned in (Torrence and Compo, 1998), it is possible to carry out the wavelet transform using Equation 19, however, it is much simpler to use the fact that the wavelet transform is the convolution between the signal and the scaled wavelet, and to carry out the wavelet transform in Fourier space using the FFT. Performing the wavelet transform in Fourier space assumes that the time series is periodic, however finite length data is being analysed, so errors will occur at the beginning and end of the wavelet power spectrum, ($|W_n(s)|^2$). As a solution, Torrence and Compo (1998) advise padding the end of the time series with zeroes before doing the wavelet transform, and removing them afterwards. All the steps to carry out the wavelet transform in Fourier space are detailed in (Torrence and Compo, 1998) and summarised here:

1. Choose a mother wavelet ($\psi_0(\eta)$).
2. Find the Fourier transform of the mother wavelet
3. Find the Fourier transform of the time series, x_n.
4. Choose a minimum scale (the smallest resolvable scale as a multiple of the time resolution, δt), and all other scales.
5. For each scale: compute first the scaled wavelet, ψ; then normalise it by dividing by the square-root of the total wavelet variance, multiply by the FT of the time series and then inverse transform back to real space.

6. Make the contour plot.

2.4 Computational Fluid Dynamics (CFD)

CFD is the use of computational methods to generate flow simulations. The advantage of using CFD is its ability to provide flow velocity and pressure measurements at any point within the computational domain, rather than just at sensor locations.

Although CFD simulations are out of the scope of this investigation, the paper on the LES of the actual rotating train (Hemida et al. 2010) and the possibilities that this technique introduces in the study of the flow around the rotating train (i.e. apply different radius of curvature to the rotating rig), make it worthy of a brief explanation.

As mentioned in Section 2.1, the motion in any realisation of an incompressible turbulent flow is governed by the mass continuity equation (Equation 4) and the conservation of momentum equation (Equation 5), also called the Navier-Stokes equations (Pope, 2000). These equations are inherently nonlinear, time-dependent and three-dimensional PDEs (Partial Differential Equations), which may be solved with suitable models for turbulent quantities or by computing them directly.

2.4.1 Turbulence models

There are different simulation approaches to solve the flow (Pope, 2000) such as Direct Numerical Simulation (DNS), Large-Eddy Simulation (LES) and Reynolds-averaged Navier-Stokes (RANS).

Direct Numerical Simulation (DNS): all turbulent phenomena at all length and time scales are resolved by numerically solving the N-S and continuity equations. Even the smallest scales have to be resolved. This implies a prohibitively high computer cost (Gatski, Hussaini et al.,

1996), since the time step and the grid space (see Section 2.4.2) have to be defined according to these smallest scales.

Reynolds Average Navier-Stokes (RANS): The fluctuating velocity fields within the turbulent flow can be of small scale and high frequency, which means that they are too computationally expensive to be simulated directly in practical engineering calculations (www.ansys.com). Instead, the instantaneous (exact) governing equations can be ensemble-averaged to remove the small scales, resulting in a modified set of equations that are computationally less expensive to solve. Behind the averaging of the equations lies the Reynolds decomposition, whereby an instantaneous quantity is decomposed into its time-averaged and fluctuating quantities (i.e. in the case of the velocity field, $U_i = \bar{u}_i + u_i'$), see Section 2.1. By substituting the instantaneous velocity by its mean and fluctuating components in the governing equations (Equations 4 and 5) and taking the average of the terms appearing in the resulting equations, the mean continuity and momentum equations (Equations 7 and 8), or Reynolds-averaged Navier-Stokes equations (RANS), are obtained. Thus, the modified governing equations now express the mass and the conservation of momentum of the averaged motion. In these modified equations, additional unknown variables (Reynolds stresses, $(\rho\overline{u_i'u_j'})$) are introduced (see Duncan, Thom et al, 1970; Cebeci and Smith, 1974; Pope, 2000, for further details) and consequently, the modified governing equations do not form a closed set and require additional relations. This is the so called closure problem. The simplest such closure scheme is to express the Reynolds Stress tensor in terms of the mean velocity itself. This is the eddy-viscosity representation proposed by Boussinesq and developed later by Taylor and Prandtl (Duncan, Thom et al., 1970; Hinze, 1976), as detailed in Section 2.1.

Large Eddy Simulation (LES): Generally, LES decomposes the structures of the flow into large and small scales. The large motions of the flow are directly simulated (in a time-

dependant simulation) while the influence of the small scale on the large scale motions is modeled. One could think of LES as applying DNS to the large scales and RANS to the small scales. The justification is that large eddies contain most of the energy, do most of the transporting of conserved properties and vary most from flow to flow; the smaller eddies are believed to be more universal, generally independent from what is happening on the larger scales, and should be easier to model (Gatski, Hussaini et al., 1996). Thus, the velocity field can be separated into a resolved and sub-grid part. The resolved part of the field represents the "large" eddies, while the sub-grid part of the velocity represents the "small scales" whose effect on the resolved field is included through a “sub-grid-scale model” (more details in Gatski, Hussaini et al., 1996). Therefore, it is essential to define a velocity field that contains only the large scale components of the total field. This is best done by filtering (Gatski, Hussaini et al., 1996), thus, eddies smaller than the size of the filter are removed. By using the kind of decomposition of the velocity field used in RANS modelling, i.e. writing the complete velocity field as a combination of the filtered field and a sub-grid scale field, new unknown variables are also introduced in the modified governing equations: the sub-grid scale Reynolds Stresses (SGSRS). Sub-grid scale modelling is therefore needed in order to identify these SGSRS and achieve closure. By far the most commonly used sub-grid scale model is the Smagorinsky model. This is an eddy viscosity model that can be thought of as an adaptation of the Boussinesq concept of Equation (9) to the sub-grid scale. More details in Gatski, Hussaini et al. (1996)

Figure 13 below shows the extent of modelling for each of the turbulence models defined above. DNS tries to solve numerically all time and length scales of the flow, which implies an overwhelming requirement for computer power. The rationale behind LES is that by modelling less of the turbulence (and resolving more), the error introduced by turbulence

modelling can be reduced (Pope, 2000). However, the need to accurately resolve the energy-containing turbulent eddies in both space and time domains which becomes most acute in near-wall regions, where the scales to be resolved become increasingly smaller, makes LES highly computationally expensive. Therefore, it is common to use RANS models instead of LES for their reduced computational effort and resources. However, inaccuracies must be accepted, as shown in the study developed by (Rodi, 1997). In this comparative study between RANS and LES calculations for high Reynolds complex flows (vortex shedding past a square cylinder and flow past a surface mounted cube), it was demonstrated that LES is more suited providing overall significantly better predictions. LES can also give information about the instantaneous flow that is out of the reach of RANS (Hemida et al., 2010). Technology advances are making LES more practical and less time consuming. In fact, LES has already been proven to be a reliable technique in prediction of the flow around simplified trains and bluff bodies (Hemida and Krajnovic, 2008; Hemida and Krajnovic, 2009; Hemida and Krajnovic, 2010). Furthermore, LES was used in (Hemida et al., 2010) to investigate the slipstream of the model train in the actual rotating rig used for experimentation in this study. Results of the simulation are compared to those obtained in the rig in Chapter 6.

Another simulation approach to solve the flow is the one known as DES (Detached Eddy Simulation), which is a hybrid LES/RANS type of turbulence model. The general idea is to use LES where the grid is fine enough to resolve the largest eddies and to use RANS where the grid is too coarse. Thus, RANS is used close to walls and LES far from walls. Muld (2010) used DES to analyse the flow structures in the near wake of an Aerodynamic Train Model (ATM) and found that for the ATM the flow is dominated by two counter rotating vortices behind the train at $St = 0.15$, similar to the 0.11 value found by Sterling, Baker et al.

(2008) for full scale tests of a 14 carriage ICE1 service train and to the 0.14 value found by Schulte-Werning et al. (2003) for and ICE2 passenger train.

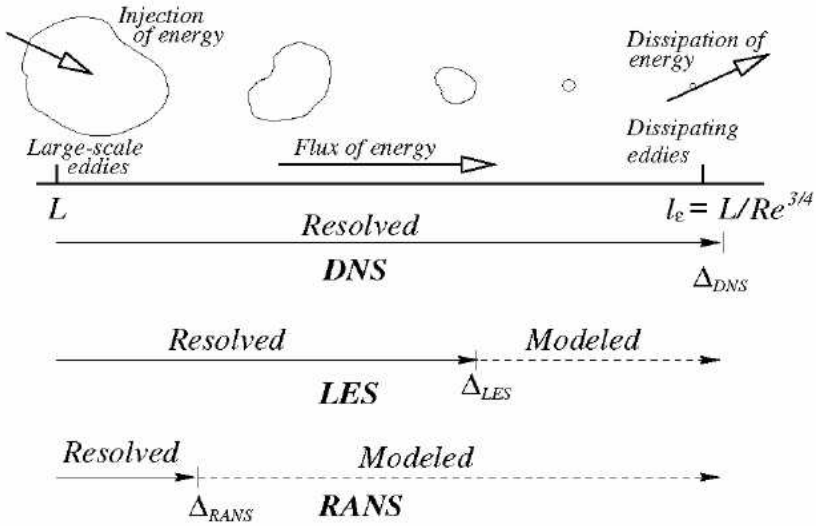

Figure 13. Extend of modeling for different turbulence models (Sodja, 2007).

2.4.2 Finite Volume Method

CFD softwares, such as Ansys (Ansys Inc., 2009) normally employ the Finite Volume Method to solve the flow governing equations. In this method, the solution domain is subdivided into discrete control volumes (cells, elements) through a computational grid, where the variable of interest is located at the centroid of the control volume. Then, formal integration of the governing equations of fluid flow over all the control volumes (cells) of the solution domain is carried out. Finite difference type approximations are introduced to replace each integrated equation by a set of linearised algebraic equations written, therefore, in terms of discrete nodal values of the dependent variables. These algebraic equations that represent the balance of fluxes of various flow variables across the finite control-volume faces are then solved by an iterative method to calculate the flow field. This method guarantees global conservation, as well as boundedness and transportiveness, of the fluid properties for the entire domain. Further details can be found in Majumdar et al. (1992), Versteeg and Malalasekera (1995) Pope (2000) and Basara (2000).

CHAPTER 3

3. APPARATUS AND ANALYSIS TECHNIQUES.

3.1 The rotating rail rig

The rotating rail rig consists of a 3.6 m diameter rail on a frame that can be rotated at up to 118 r.p.m., which corresponds to a rail speed of 22 m/s, see Figure 14. It was originally designed so that standard rail sections could be mounted on the frame to enable investigations into the removal of accreted organic matter using novel laser based techniques (Higgins, 2003), and has since been used to investigate conductor shoe icing with a stationary conductor shoe held above the rotating rail whilst the temperature was lowered to below freezing conditions.

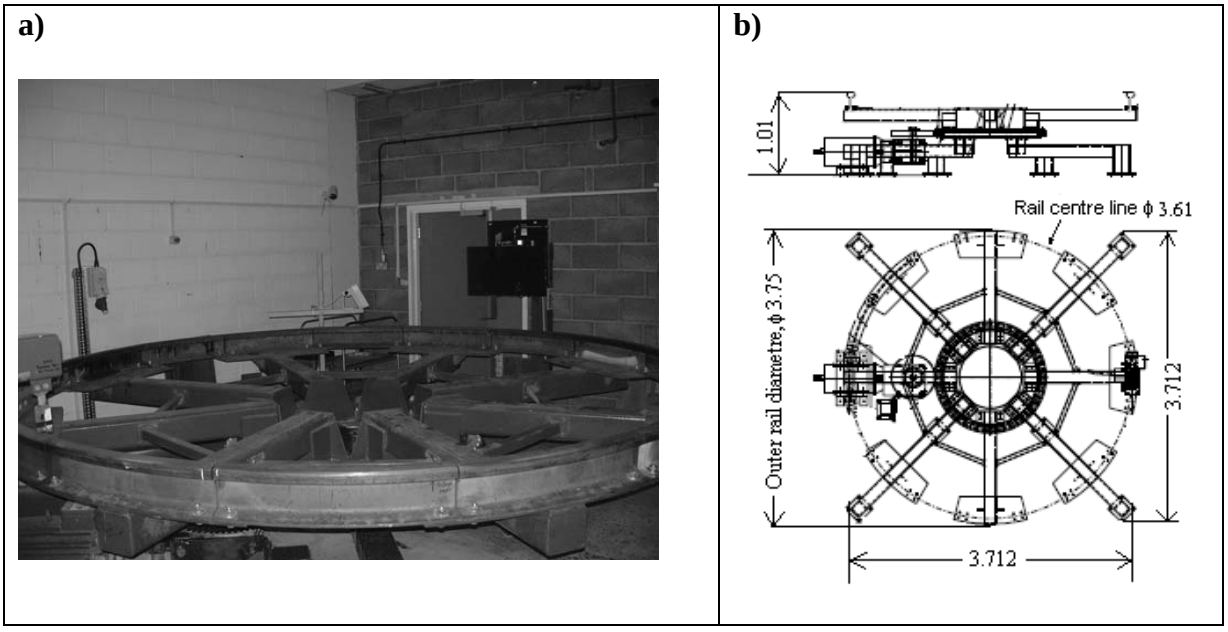

Figure 14. Rotating rail rig. a) In its original form, b) Rail schematic showing main dimensions (in meters).

In the current investigation a 1/50th train model was fixed to the rotating rail via a clamp and a bolt (two sets in each carriage), so that they both moved as a whole. In order to reduce the

turbulence arising from the rotation of the wheel, as well as to provide a ground plane over which the train moved, a wooden platform with a circular slot slightly bigger than the rail was positioned above the rig. The gap between the train and the platform was closed with brushes. The rig set up and rig components are shown in Figure 15. The most important aspect of this rig is of course that multiple train passes can be achieved very quickly (one per revolution of the rig) and thus experiments can be carried out much more rapidly than with the current full scale and model scale techniques.

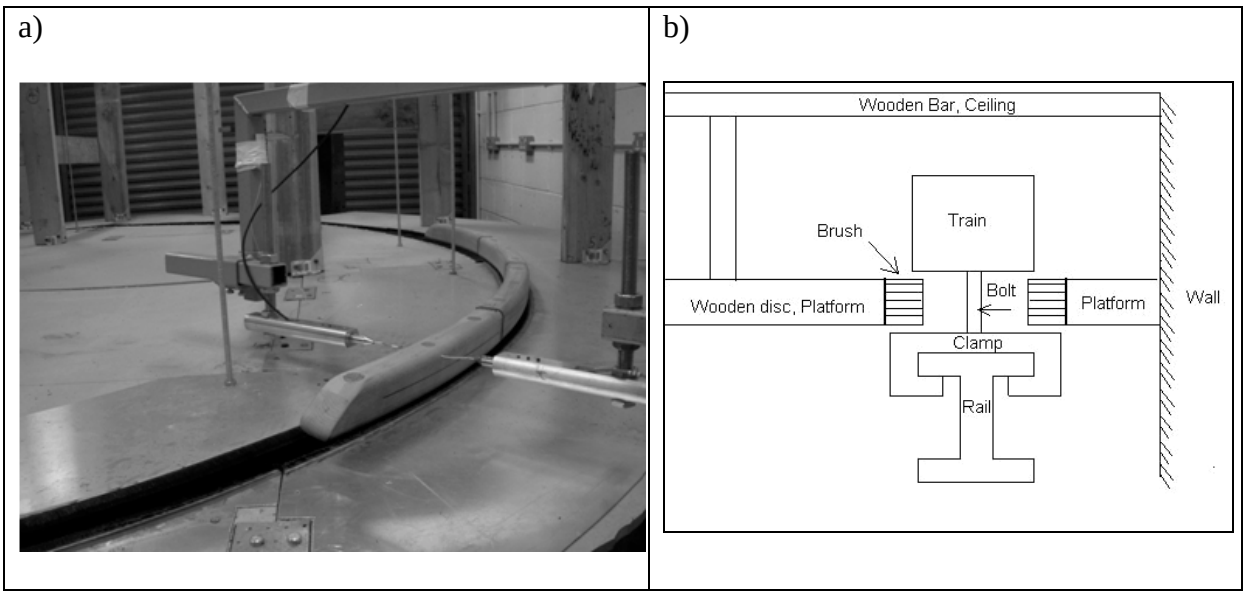

Figure 15. Rig set up a), and rig components, b), for aerodynamics experiments showing the wooden platform and the slot through which the train passes. The probes are located at either sides of the train. The train is formed of 4 carriages and its curved shape can be appreciated.

3.2 The train model

The train model has undergone significant changes in order to provide the best flow measurements possible. The preliminary experiments that were carried out used an existing $1/40^{th}$ scale four-carriage train model. The problem that emerged was that the length of the train carriages (about 50 cm) was relatively large in comparison to the radius of curvature of the rig, and thus there were sharp discontinuities in train orientation at the end of each carriage. Also, the cross section was not constant along the train, so there was a significant

variation in the probe measurement position from both the train top and sides. To tackle these problems, it was decided to construct a “curved” train so that measurements were provided along curved lines next to the vehicle. In addition, this new train was designed as a simplified 1/50th scale ICE2 train (Figure 16), so that results could be compared to those obtained at the TRAIN rig (Baker, Dalley et al., 2001), where a 1/25th scale four-coach ICE2 train model was employed. Obviously, the rotating rig results will be affected by the curvature of the train, with the boundary layer being thicker on the convex side of the train than in the concave side, as explained in Section 2.1.3.

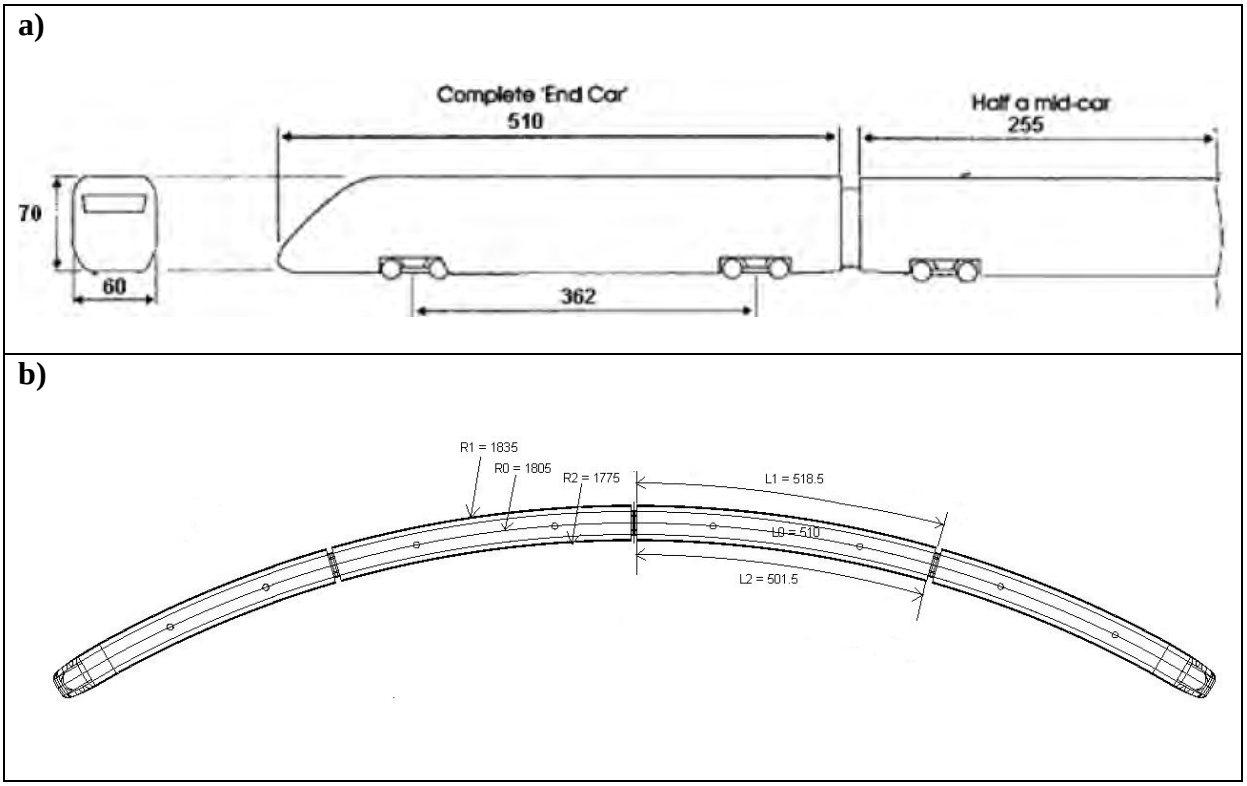

Figure 16. Train model. a) Dimensions at rail centerline. b) Plan view of the model. All dimensions in mm.

3.3 The probes

The slipstream and wake velocities were measured using stationary Cobra probes (provided by Turbulent Flow Instrumentation P/L). Whilst other types of flow instrumentation, such as Laser-Doppler Anemometry (LDA) and Particle Image Velocimetry (PIV), have been used in wind tunnel testing (Lawson et al., 2006) these are not necessarily suitable for wake flow measurements of model passenger vehicles due to the low rate of data capture when air is the working fluid (Shaw et al., 2000) and are not particularly suited to moving models testing. Hot wire anemometers overcome many of the limitations of LDA and PIV, but it seems (De Guzman, Fletcher et al., 1994; Mousley and Watkins, 2000; Watkins et al., 2002) that multi-hole pressure probes provide the benefits of the former, while being robust, requiring little calibration and introducing a 3-component velocity measurement system (at speeds from 2 m/s up to 100 m/s with an accuracy of measurements generally within ±0.5 m/s (Turbulent Flow Instrumentation Pty Ltd, n.d.)) able to provide local pressure away from the surface and offering a reasonably high frequency response (can carry out flow measurements at frequencies of more than 2 kHz), making them ideal to study highly turbulent flow fields (Watkins et al., 2002), like those around different types of full and model scale vehicles, as seen in Mousley and Watkins (2000), Gilhome, Saunders et al. (2001) and Quinn et al. (2010). The Cobra Probe remains relatively accurate to greater than 30% of the turbulence intensity (Turbulent Flow Instrumentation Pty Ltd, n.d.)

Two Cobra probes were positioned in the inner and outer side of the train. The probes were mounted on a support (which allowed for yaw and pitch angle rotation as well as displacement along the vertical and horizontal-radial axis, see Figure17 for probe angles and axes) fixed to the ground (and thus isolated from the mechanical vibrations caused by the rotating rail rig itself), as seen in Figure 18.

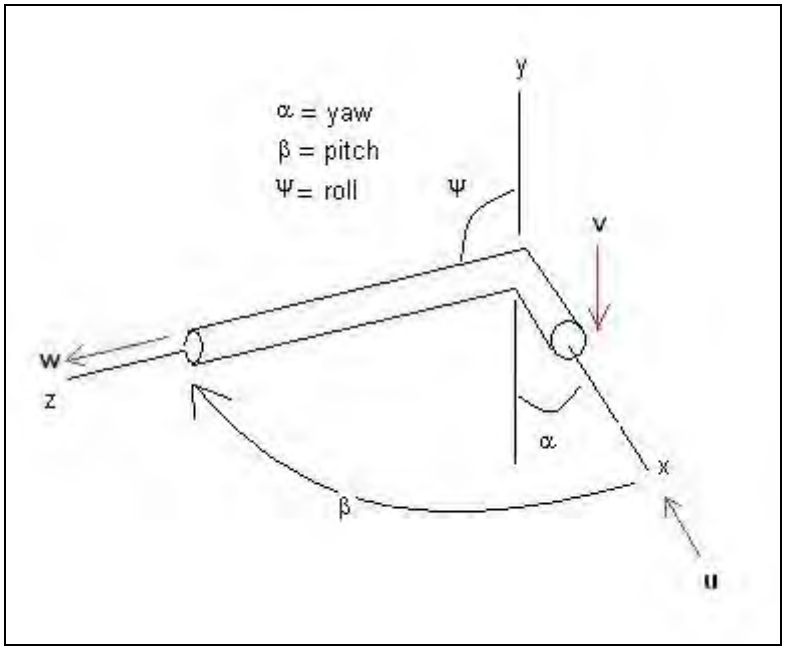

Figure 17. Probe angles and axes

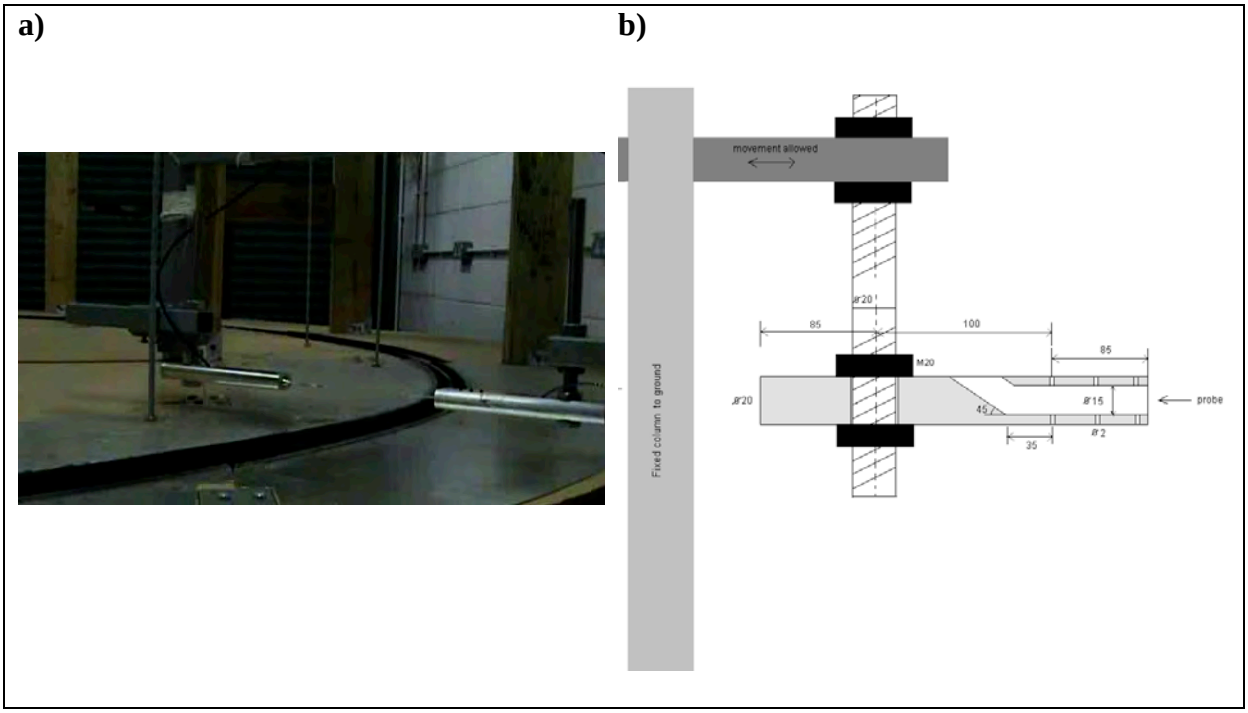

Figure 18. Probe support. a) rig set up, b) schematic drawing (dimensions in mm)

The probe's reference pressure port was vented to a location out of the flow , 2 m away from the testing area (via a 50 cm silicon tube inside a funnel fixed to the wall), so that pressure fluctuations did not interfere with the measurements. The possibility to position the probes at

different heights and distances from the train lateral and top surfaces, allowed a comprehensive study of the flow around the train to be carried out.

The principle of operation of the probes is to relate, via calibration tables, the ratios of the tap pressure fields detected at four 0.5mm pressure tap locations (see Figure 20) on the faceted head (connected via tubing to pressure transducers in the body of the Probe) to the magnitude of the instantaneous local velocity vector, the flow yaw and pitch angles and the instantaneous static pressure (Turbulent Flow Instrumentation Pty Ltd, n.d.). Data processing is performed by the included Device Control software.

Probes are supplied fully calibrated and ready to use. The transducers are very stable over time with typical calibration checks showing less than 0.1% change over 1-2 years (Turbulent Flow Instrumentation Pty Ltd, n.d.). A static calibration can be performed, in which a range of known pressures are applied to the probe's reference pressure port. However, no calibration was performed as the required tubing needed to connect the reference pressure port at the back of the probe to the device applying the known pressure needed changing in diameter considerably as the reference pressure port is of a very small diameter, 0.5 mm. This procedure was deemed impossible with the available equipment. Therefore, it was decided to check the probes against one another and check for any major inconsistencies. As shown in Figure 19, for measurements taken at train mid height (z = 0) and at 0.25 m equivalent full scale distance from the model outer side, the ensemble averages of the slipstream velocities captured by both probes were very similar. In order to quantify the difference between both ensembles it was decided to calculate the root mean square value (rms) of both sets of data, $y_{rms} = \sqrt{\frac{1}{n}(y_1^2 + y_2^2 + \cdots + y_n^2)}$ (n is the length of the series). It was found that for probe 1, the rms value of the ensemble was 0.135 whilst for probe 2 it was 0.137, a difference of 1.48%.

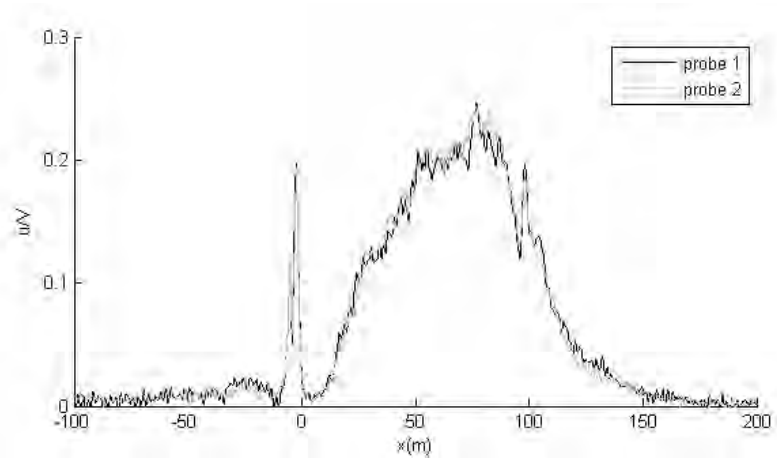

Figure 19. Probes comparison. Ensemble average of slipstream velocities measured at train mid height (z=0) and at y=0.25m from the model side

The calibrated range of the probe falls within a cone of ±45° of the probe *x* axis, see Figure 20. Thus, only flows whose direction resides within this ±45° cone are accepted (Turbulent Flow Instrumentation Pty Ltd, n.d.). Any other flows are rejected and measurements register a zero value of the flow velocities. The probe software includes a 'Percent Good Data' indicator that shows the percentage of samples that are within this ±45° calibrated range of the probe, and therefore acceptable. A percentage below 80% indicates that a good proportion of the data being sampled is not within the calibrated region of the probe. Percentages below 60% indicate a very low data acceptance rate. To improve the percentage of data in the calibrated region, the probe has to be pointed as close as possible to the mean flow direction (the display of the mean pitch and yaw angles helps to determine when the probe is best orientated as the mean pitch and yaw should both tend towards zero). In the present investigation, it was very difficult to place the probe so that it was continually facing the mainstream of the flow as the direction of the flow in the nose area varied in respect to that along the train and that of the wake. Therefore, some data was rejected as it fell beyond the ±45° cone of acceptance, especially around the nose area. In fact, looking at the individual laps within a given run, it was observed that the acceptance data percentage of the overall flow field was very low,

around 45-55% depending on the lap under consideration. As might be expected, carrying out the ensemble average of the 80 laps helped reduce the rejected data considerably being then only appreciable in the nose region of the flow (see Section 3.5 for further details).

Another factor influencing the data acceptance rate is the range of measured velocities. Taking into account that the probes performance range is from 2 m/s to 100 m/s and that the velocities that were being considered were 7, 9.45, 14.2 and 16.5 m/s (when the train passed but then considerably less as the train moved away from the probe) and considering as well the distance at some points of the probes from the train surfaces, it seems that the probes were working very close to their lower velocity limit for much of the test. The higher the train/wheel velocity the more data is accepted and the clearer the results (velocity traces) obtained. However, the maximum velocity allowed for the experiments was of 16.5 m/s, as velocities above 16.5 m/s endangered the stability of both the train and the structure mounted around the wheel.

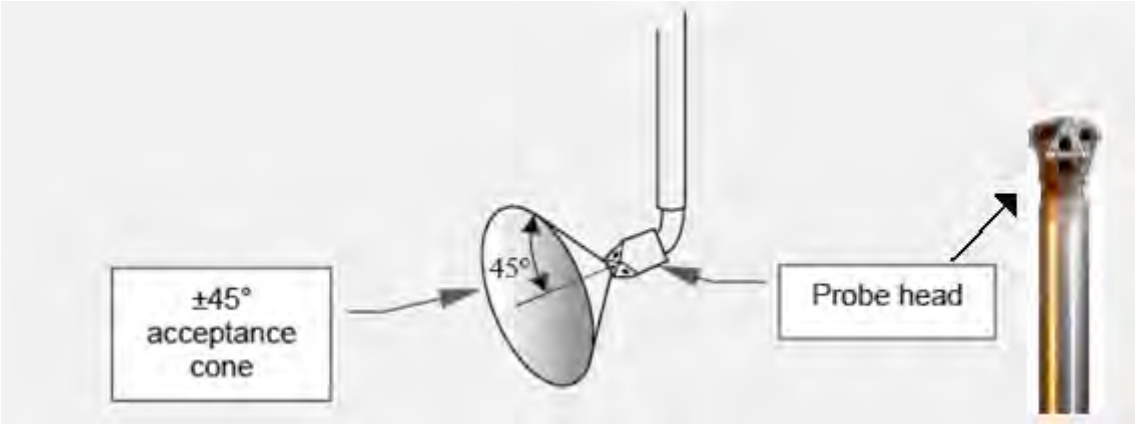

Figure 20. Cobra probe cone of acceptance and head detail. Flow direction must reside within $\pm 45^{\circ}$ of the probe x axis. (www.turbulentflow.com.au/downloads/Cat_CobraProbe.pdf)

Chen, Haynes et al. (2000) identified six different types of measurement errors that arise from using the probe: uncertainties in the calibration and transfer functions (see Hooper and Musgrove (1997) for a detailed definition of the latter), velocity gradients across the probe tip, blockage effect of the probe tip and the stem, wall vicinity effect, high turbulence levels in the

flow and probe misalignment. In the present case of study, the different flow directions that take place along the train, made it very difficult to position the probe so that it was continually facing the main stream of the flow, inducing a misalignment error especially around the nose of the train, where the flow direction was almost perpendicular to the direction of travel, whilst the probe was positioned parallel to it. Wall vicinity effects might be present for the closest measuring point at the side of the train (3 mm) as it was less than two probe diameters (2.6 mm) away from the wall. The errors of calibration and turbulence were rejected by the software of the probe itself, and the error of blockage effect was expected to be negligible.

Electrical noise was present with a signal to noise ratio (SNR[7]) of around 22Db. In order to reduce the noise, Matlab filtering (Butterworth filter, see MathWorks, Inc. (2008)) at 1 kHz was carried out after data collection.

3.4 Analysis techniques

In order to get measurements every 1-3 mm along the train in the *x* direction (0.05-0.15 m full scale equivalent, scaled on typical full scale and model scale speed measurements), depending on the train speed, sampling frequencies of 3 kHz were adequate. In order to avoid signal aliasing, the acquisition rate was set to 10 kHz and the output rate was set to 6 kHz. As mentioned before, 4 carriages of the 1/50th model scale train were used (with an average full scale length, L, of the four cars, allowing for the inter-carriage gaps, of 26 m).

The raw probe binary data files were converted to plain text files by using the Time History File Conversion utility provided by the probe software. Each text file corresponded to one run, of 80 laps, at a given distance from the train side or top and at a given wheel/train speed.

[7] SNR is the power ratio between the signal (meaningful information) and the background noise (unwanted signal) and is often expressed using the logarithmic decibel scale. $SNR = 10\log_{10}(P_{signal}/P_{noise}) = 20\log_{10}(A_{signal}/A_{noise})$, where P is average power and A is the root mean square value.

The file included all three components of velocity and the static pressure of the flow field for each sampling position.

A position sensor that gave an impulse signal every time the nose of the train passed was used in order to identify the train slipstreams within the signal. Matlab codes were then developed to align the different laps with the different pulses, establishing in that way the nose of the train as a common origin. It was then possible to create the ensemble-average mean velocity and ensemble-average standard deviations time series. Normalised velocities and standard deviations were also formed by dividing by train speed.

Using Matlab the effect of the train speed was assessed, as well as the spatial variation of velocity and a comparison between flows on the inner and outer surfaces of the train was carried out. Velocity and turbulence intensities contours at different cross sections along the train were also obtained. It was also possible to study the boundary layer displacement thickness at different cross sections along the train and the pressure distribution along the train. The frequency content of the probes readings (to determine both the dominant modes of variability and how those modes vary in time) and the wake structure of the flow field were studied using wavelet transforms (Torrence and Compo, 1998). All results are given in Chapter 4.

3.5 Tests.

As in previous studies (Baker, Dalley et al., 2001; Sterling, Baker et al., 2008) the coordinate system used is such that the *x*-axis follows the train direction of travel (as an individual sees it from the platform edge), with the origin taken to be when the nose of the train passes the measuring point (as indicated by the pulse shown in the position sensor placed on one of the four legs that sustain the wheel.). The *y*-axis is in the horizontal plane perpendicular to the track, with the origin taken at the train side edge and positive outwards from the train. The *z*

axis is vertically upwards, with its origin at train mid height (1.5 m above the ground plane). These definitions are consistent with previous work (Baker, Dalley et al., 2001; Sterling, Baker et al., 2008). However it is not wholly satisfactory and in some places in what follows a different y axis system will be used (y^*) with the origin at the train centre line. Taking into account the rig presented here is circular, then the x and y axis are tangent and perpendicular to the rail respectively. Note that all lengths from now on will be given as equivalent full scale values.

For side measurements, one probe was located in the inner concave side of the train and the other one on the outer convex side of the train (as shown in Figure 20). Measurements were taken at full scale equivalent distances of y = 0.15, 0.25, 0.5, 0.75, 1, 1.5 and 2 m from both train lateral surfaces. For roof measurements, the two probes were placed symmetrically at distances of y^* = 0.5, 1, 1.25, and 1.5 m from the train centre line so that the whole train width was covered. From there, measuring points would follow the lateral positions mentioned before for the side measurements. Equivalently, taking into account that z = 0 corresponds to train mid height, side measurements along the z-axis were taken at full scale values of z =-1, -0.5, 0, 0.5, 1 and 1.5 m. Similarly, top measurements were taken at z = 2, 2.25 and 2.5 m. In this way, a grid of measuring points was defined around the train, as seen in Figure 21 below.

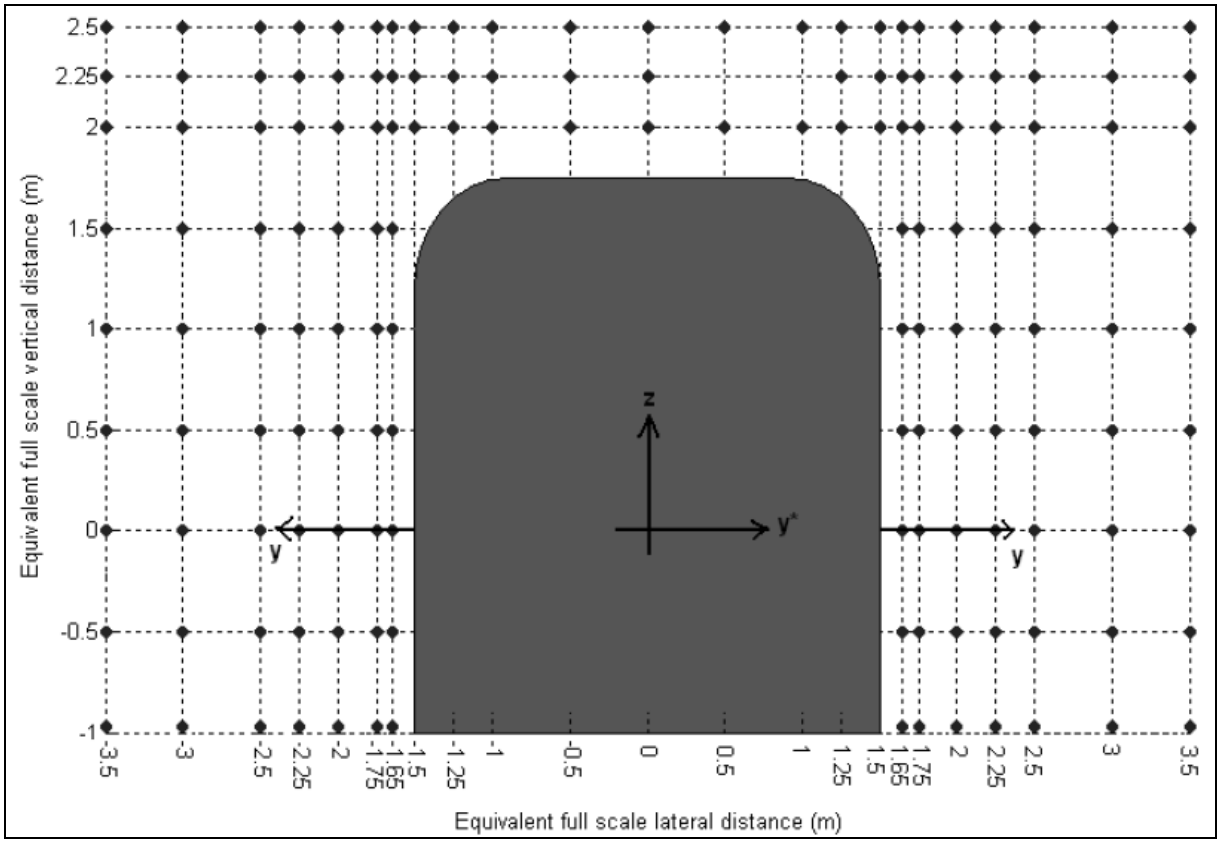

Figure 21. Measurement points around the train. The *y*-axis shows train lateral distance from the edge of the train and the *y axis shows train lateral distance from train centerline. The *z*-axis shows vertical distance from train mid height.**

Experiments were carried out at wheel (or train) velocities of 7, 9.45, 14.2 and 16.5 m/s. As stated in Section 3.2, velocities above 16.5 m/s endangered the stability of both the train and the structure mounted around the wheel, so this was the maximum velocity that could be achieved. Note that in general the overall velocity magnitude, except around the nose and tail of the train, was very close (to within 2%) to the magnitude of the longitudinal velocity component (the lateral and vertical components were negligibly small, not even reaching 0.08 of the train speed, and therefore staying well below the performing range of the probe). Thus, velocities presented in this paper are given in terms of the longitudinal velocity component. By doing so, the nose and wake peak are underestimated as the flow in these areas is highly three dimensional and all velocity components should have been considered. However, it was especially difficult to quantify the nose peak errors as the rejected velocities (due to the flow

direction being out of the ±45° cone acceptance range of the probe) took place all around the train nose peak, for either ensembles (v_{tot}/V and u/V). For 65% of the measurement points, the rejected velocities (seen as zeros in the velocity ensemble average) were found before and after the train nose peak (Figure 22(a)). It was found that the nose peak error would vary considerably from one measurement point to another, taking values from 5% up to 55%. In the case of Figure 22(a), for measurements taken at train mid height and 0.25 m from the model outer side, the nose peak error derived from using the longitudinal velocity component instead of the total velocity in the ensemble average was found to be 42%.

For the remaining 35% of the measurement points, it was impossible to quantify the nose peak error as the rejected velocities included the nose peak itself, as shown in Figure 22 (b) for measurements taken at train mid height and 0.75 m from the model outer side.

a)

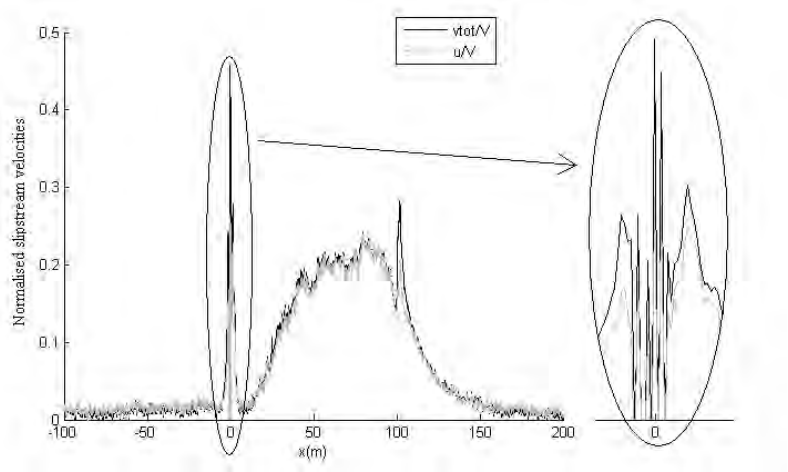

b)

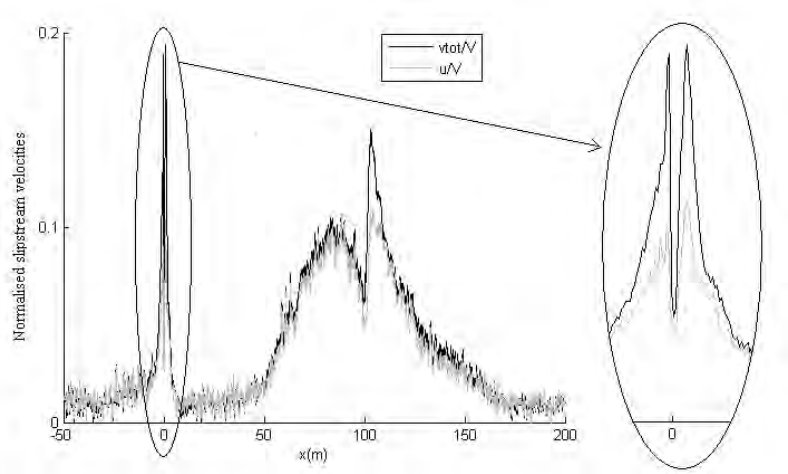

Figure 22.Comparison of train slipstreams ensemble average velocities given in terms of the total velocity or the longitudinal velocity component. a) measurements taken at train mid height, *z*=0 m, and *y*= 0.25 m from the train outer side. b) measurements taken at train mid height, *z*=0 m, and *y*=0.75 m from the train outer side.

In terms of the wake peak error, no rejected velocities were found in the wake area after carrying out the ensemble average of the 80 laps. All measuring points showed a greater value of the wake peak when the slipstream velocities ensemble average was given in terms of the total velocity, instead of the longitudinal velocity component. Different wake peak errors were found for different measuring points, with values ranging from 6-33%. However, these

results should be handled with care. As detailed in Sterling, Baker et al. (2008), the main source of uncertainty in this area comes from the ensemble averaging technique itself, as the velocity measured in the near wake region (particularly the cross flow velocity) depends crucially on the phase of the vortex shedding cycle as the measuring instrument is passed .

Taking all this into account it was decided to keep the slipstream results given by means of the longitudinal velocity component, as the results given in terms of the total velocity still present rejected data all around the nose area, and the wake peak value is purely nominal.

It was also decided to remove in what follows the rejected velocities from the slipstream results so that a clearer picture was obtained (as detailed in Section 3.4).

As mentioned before, to obtain adequate results a number of identical tests needs to be carried out (at least 10 and ideally 20) with the results being ensemble averaged to obtain mean and standard deviations of time histories (Johnson et al., 2004). Taking advantage of the capability of the rig, 80 laps were ensemble averaged. To check the repeatability of the measurements, the experiments were done three times (that is, three runs of 80 laps each) at same train speed and at a fixed measurement point. The root mean square value (rms), $y_{rms} = \sqrt{\frac{1}{n}(y_1^2 + y_2^2 + \cdots + y_n^2)}$, of the different run ensembles was found for a given number of laps in order to quantify the difference between the ensembles. It was found that with 20 laps the slipstreams velocity results would clearly differ from each other (Figure 23(a), with a rms value of 0.1687 for run 1, 0.1701 for run 2, and 0.1603 for run 3), with 40 laps the difference between the run ensembles was still noticeable (Figure 23 (b), with a rms value of 0.1595 for run1, 0.1654 for run 2 and 0.1609 for run 3), with 60 laps this difference was diminished (Figure 23(c), with a rms value of 0.1611 for run 1, 0.1622 for run 2 and 0.1598 for run 3) and with 80 laps, results were practically the same (Figure 23(d), with a rms value of 0.1608 for run 1, 0.1613 for run 2 and 0.1601 for run 3). For comparison purposes,

as different train velocities were tested, the ensemble mean velocity and standard deviations results were normalised by train speed. With this normalisation, the effect of the model speed was not significant, as shown in Section 4.2.

As mentioned in Section 3.4, the data acquisition rate was set to 10 kHz to avoid signal aliasing with the output rate set to 6 kHz, so that measurements were provided every 1-3mm along the train, depending on the train speed.

In order to reduce the noise, Matlab filtering at 1 kHz was carried out after data collection. The Butterworth filter (MathWorks, Inc., 2008) was used as recommended by CEN (2009) for model scale tests and as used by other authors in the study of train slipstreams (i.e. Sterling et al, 2008 and Quinn and Hayward, 2008). Filtering at 1 kHz was carried out as a result of trial and error so that the filtered signal still maintained the main features (i.e. nose and wake peaks) of the original signal and without showing much phase distortion.

In all tests, the train was allowed to go round for a reasonable time in order to let the airflow stabilise in the room before zeroing the probes and taking any measurements. As shown in the following chapter, there seems to be a low velocity ongoing airflow around the wheel due to the movement of the train and the wheel.

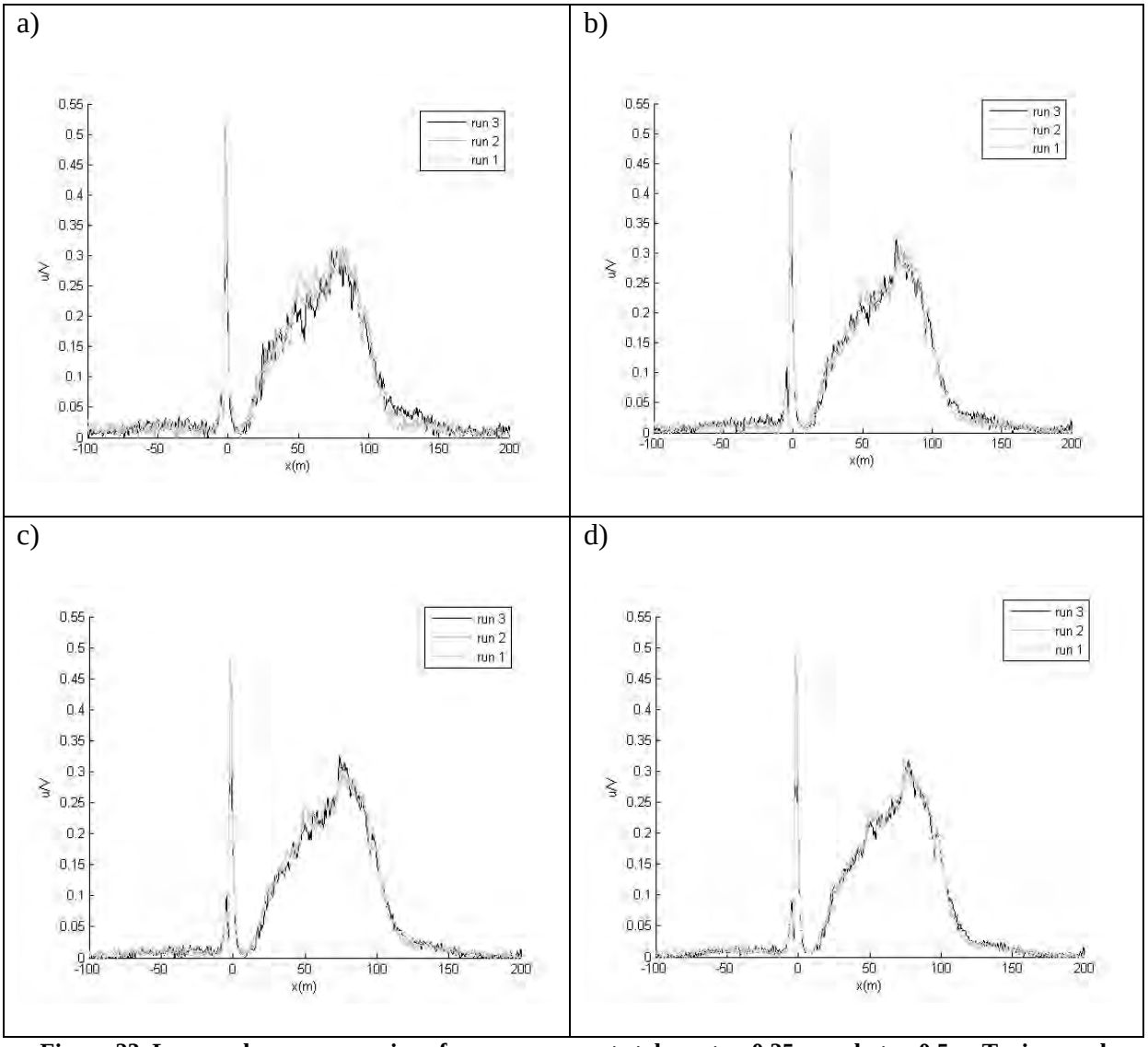

Figure 23. Laps and runs comparison for measurements taken at y=0.25m and at z=0.5m. Train speed 16.5m/s. x axis shows equivalent full scale distance along the train, and y axis shows slipstream velocity normalized by vehicle velocity. a) Slipstream velocity ensemble average of 20 laps for all three different runs, b) Slipstream velocity ensemble average of 40 laps, c) Slipstream velocity ensemble average of 60 laps, d) Slipstream velocity ensemble average of 80 laps.

CHAPTER 4

4. EXPERIMENTAL RESULTS AND ANALYSIS

From the tests carried out in the Rotating Rail Rig it was possible to obtain velocity time histories from ensemble averages of a large number of runs (of the order of 80). These velocity time histories allowed carrying out a detailed analysis of the train slipstream. As seen in the following sections, it was possible to assess the effect of the curvature of the train (Section 4.1), the effect of train speed (Section 4.2), the spatial variation of the slipstream velocities (Section 4.3), the thickening of the boundary layer along and around the train, the turbulence levels (Section 4.4) and the distribution of the different turbulence scales around the train (Section 4.5). It was also possible to study the pressure distribution of the flow field around the train (Section 4.6).

Firstly, however, it is necessary to mention, that in all tests, the slipstream velocity results obtained showed a different residual normalised velocity depending on the train speed, taking a lower value the higher the train speed. This residual airflow (see Figure 24 for typical measurements at y = 0.25 m and z = 0 m) was apparent before and after the train had passed, when it should be zero. The value of this normalised residual airflow was found for each measuring point by averaging the normalised velocity values obtained along a distance of five train carriages prior to the passing of the train. For train speeds of 16.5 m/s and 14.2 m/s the average normalised value for all measuring points was 0.071 and 0.079 respectively, with a corresponding standard deviation of 0.007 and 0.006. For lower vehicle speeds it was found that the average residual increased somewhat (to 0.116 at the lowest speed of 7 m/s, with a standard deviation of 0.014).

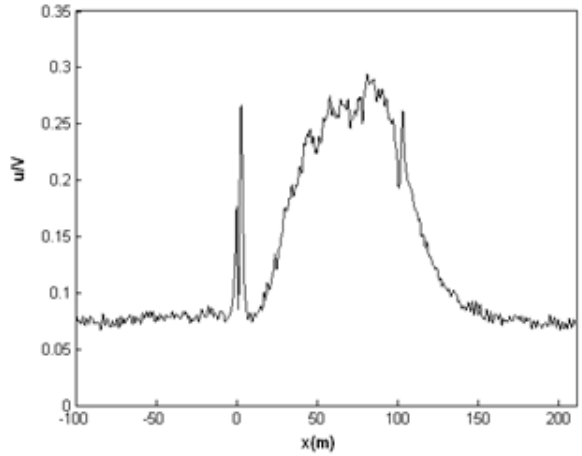

Figure 24. Set airflow. x axis shows equivalent full scale distance along the train, and y axis shows slipstream velocity normalized by vehicle velocity. Nose of train passes at *x* = 0 m and tail at *x*=104m. Train speed was 16.5m/s and measurements were made at half train height. *z* = 0 m, and at *y* = 0.25 m from the outer side edge of the train.

This residual normalised velocity was the result of an ongoing airflow produced both by the train and the movement of the wheel. It would have been desirable to reduce this effect, so that the train would enter a wind free zone when approaching the testing area. However, the different proposed solutions, i.e., place funnels to divert the airflow, use a fan to blow air directly into the testing area to remove the ongoing air, etc. were generally impracticable. Assuming that this set airflow was constant across the flow field, in what follows, the wind offset that the rig wrongly introduced has simply been subtracted from the results. Aside from this uncertainty due to experimental bias, the major uncertainties in the data that will be presented below are in the values of the ensemble averages of slipstream velocity. As noted previously the use of a large number of individual runs in forming the ensemble reduced this uncertainty to low values which are estimated to be of the order of 0.02 x model speed.

It is important to mention that due to the positioning of the probes (facing velocities in the train direction of travel), all slipstream results showed zero velocity values in the nose area as velocities were rejected for being out of the ±45° cone acceptance range of the probes, as discussed in Section 3.5. In order to obtain a clearer picture of the train slipstream velocities

time histories, it was decided to remove this rejected velocities effect by directly substituting the zero values by the maximum wind offset value obtained along a distance of five train carriages prior to the passing of the train. Further Matlab signal filtering also helped reducing these velocity drops effects. Although the nose and wake peaks were also smoothed by the filter, it was shown that the nose peak error introduced by the filter would vary from one measurement point to another, ranging from 6-22%. Figure 25 a) shows the original velocity ensemble average signal, for measurements taken at train mid height and 0.25 m from the train model side, with both the wind offset and the rejected velocities effect. Figure 25 b) shows the filtered signal with the wind offset and rejected velocities removed. The nose peak error, due to filtering, in this case is 22%.

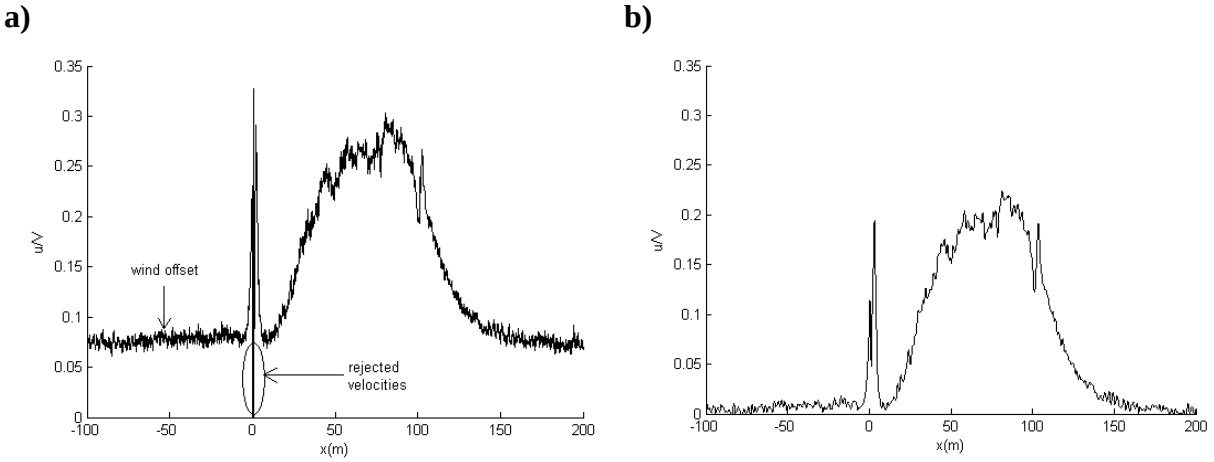

Figure 25. Normalised velocity ensemble average for measurements taken at *z* = 0 m and *y* = 0.25 m (outer side of the train). Train speed of 16.5 m/s. a) Ensemble average showing the set airflow and the rejected velocities. b) Ensemble average after removing the wind offset, the zero value velocities and applying 1 kHz filtering.

4.1 Comparison between flows on the inner and outer surfaces

As mentioned before, the rig introduces a curvature that has to be studied and dealt with. It was found that velocity time histories obtained for the inner concave side of the train differed greatly from the outer convex side of the train, all along the train and for all the different measuring points. Although both probes captured the different flow regions around the train

(a nose region, a boundary-layer region, a near-wake region and a far-wake region) it was seen that slipstream velocities along the convex side were greater and extended for longer than along the concave side of the train, as seen in Figures 26(a) and 26(b), where slipstreams velocities measured at train mid height and at different lateral distances were ensemble averaged and normalised (for comparison purposes).

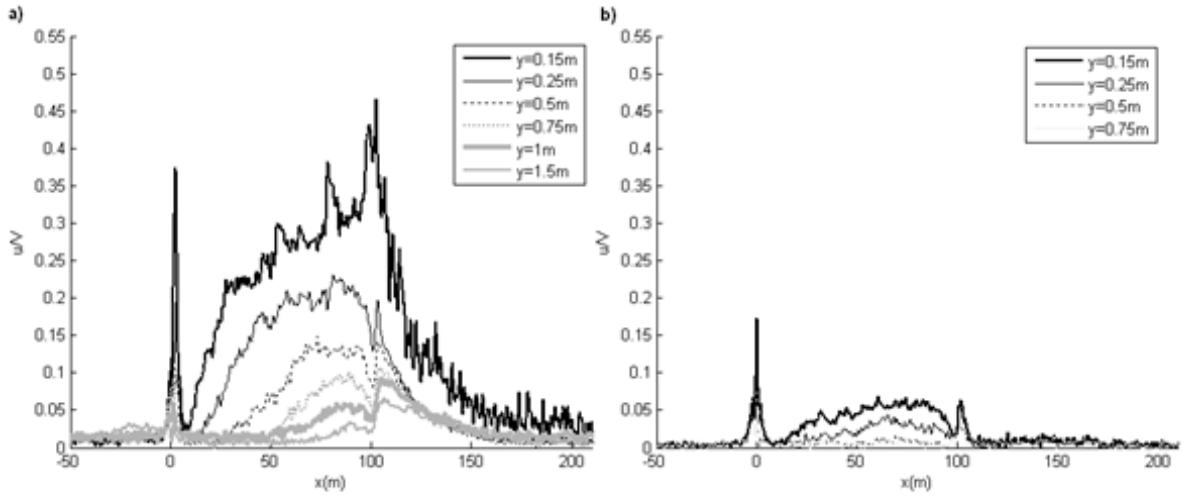

Figure 26. Ensemble average normalised velocities at train mid height and at different lateral distances from the train surface. Train speed=16.5m/s. (a) Outer probe. (b) Inner probe.

It is noticeable that the convex side results showed greater slipstreams velocities than the concave side, as described in Section 2.1.3. In fact, slipstreams velocities for the concave side of the train were 5 times smaller in the boundary layer than for its convex counterpart. In addition, the boundary layer velocities fell to zero for $y > 0.25$ m from the train inner concave side, whilst the outer convex side still showed a boundary layer region for y up to 1 m from the model side. Also, in the convex side, the slipstream velocities seemed to decrease slowly after the tail peak entering the far wake region, whilst the concave side results showed that after the tail peak, velocities fell straight to zero, not allowing for a far wake region to develop. What is more, comparing results from both sides to those obtained in the TRAIN rig, it was noticeable that the convex side results showed a good resemblance to the latter, as

shown in the following chapter. Taking all this into account, in the following sections only the convex side measurements are discussed in any detail.

4.2 Effect of train speed

To check for the effect of train speed in the results, the wheel was spun at velocities of 7, 9.45, 14.2 and 16.5 m/s. These velocities with the train height (0.07 m) gave a Reynolds number (hV/v − h is the train height) range of 3.27 x 10^4 to 7.7 x 10^4, where v is the kinematic viscosity of air. Slipstreams velocities were measured at all points around the train. The ensemble-average mean velocity time series were found for each experimental configuration and then normalised by train speed. Figure 27 shows how by normalizing the slipstreams velocities by train speed the difference in the results was not large, with normalised velocity values in the different flow regions taking almost the same values for the different train speeds.

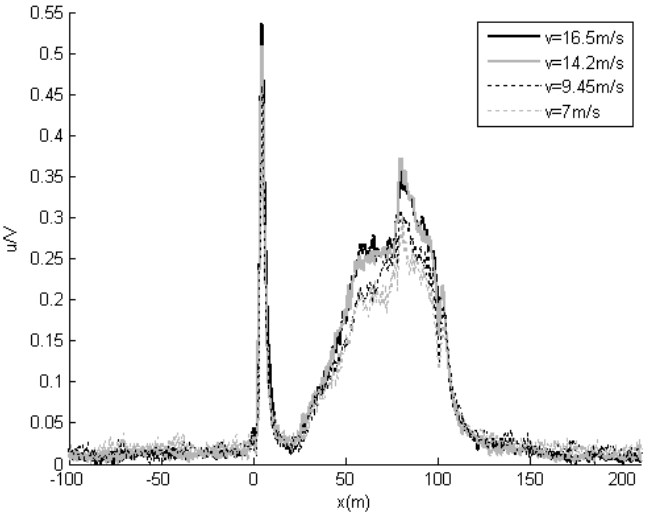

Figure 27. Normalised splipstream velocities ensemble average at z = 1 m and *y* = 0.25 m at different train speeds.

The different values for the lower train speeds in the boundary layer region could be due to the fact that at these train speeds the probes were working, at some points, below their performance range, and therefore obtaining a very poor acceptance rate, where, depending on

the tests, only 45% to 55% of the data was accepted. In this figure velocities were measured at 1 m above train mid height and at 0.25 m from the model outer side, although results presented here repeat for all train side and top measurements. Taking this into account, on what follows, only results obtained at 16.5 m/s are considered in order to minimise the amount of data to be presented.

4.3 Spatial variation of velocity

As in previous studies (Baker, Dalley et al., 2001; Sterling, Baker et al., 2008), the ensemble mean normalised slipstream velocities, with the origin aligned with the peak of the nose pressure pulse, follow a defined pattern (Baker, Dalley et al., 2001). In all cases, it is possible to identify first a nose peak, followed by an increase in velocity in the train boundary layer and a near wake peak that gradually decays downstream. However, normalised velocity values and flow development will vary depending on the place where measurements were carried out, i.e. measurements taken along a vertical axis from the model side, Figure 28 (a) and (b), or taken in the roof along a horizontal axis, Figure 29.

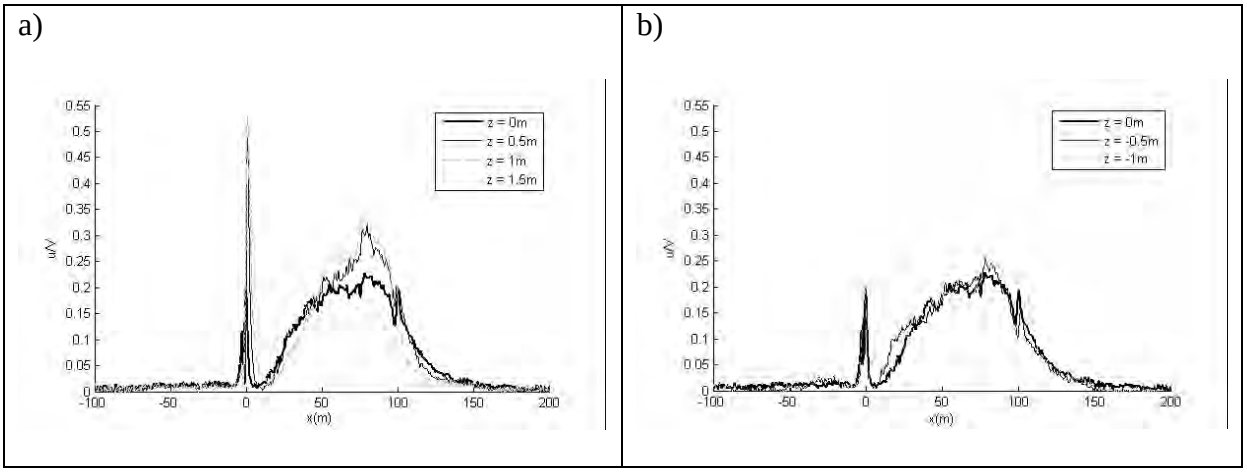

Figure 28. Normalised velocity time histories for measurements taken at *y* = 0.25 m from the model side and at different heights . (a) Above mid train height, (b) below mid train height.

As can be seen in Figure 28(a), at a distance of 0.25 m from the model convex side, the nose peak increased from a normalised velocity value of 0.2 to 0.55 as the measurement point

moved towards the top of the train. Velocities in the boundary layer developed similarly for the first two carriages with increasing *z*. For the last two carriages however, velocities decreased with increasing z. However, for the top measurement at *z* = 1.5 m from train mid height, velocities increased rapidly along the first carriage of the train with a maximum at the end of it and then fell and stabilised in lower values along the rest of the train. Figure 28(b) shows how velocities increased as the measurement point moved down towards the platform (however, this time the nose peak stayed at a normalised velocity value of 0.2 at all heights).

For measurements taken on the roof of the train, at *z* = 1.75 m from train mid height, it can be seen (Figure 29) how velocities increased with increasing *y** (lateral distance from the train centre line) for the first two carriages whilst decreasing for the rear ones. Measurements beyond the train model side (*y** = 1.5 m) show how the slipstream velocities decreased with increasing *y**, as expected.

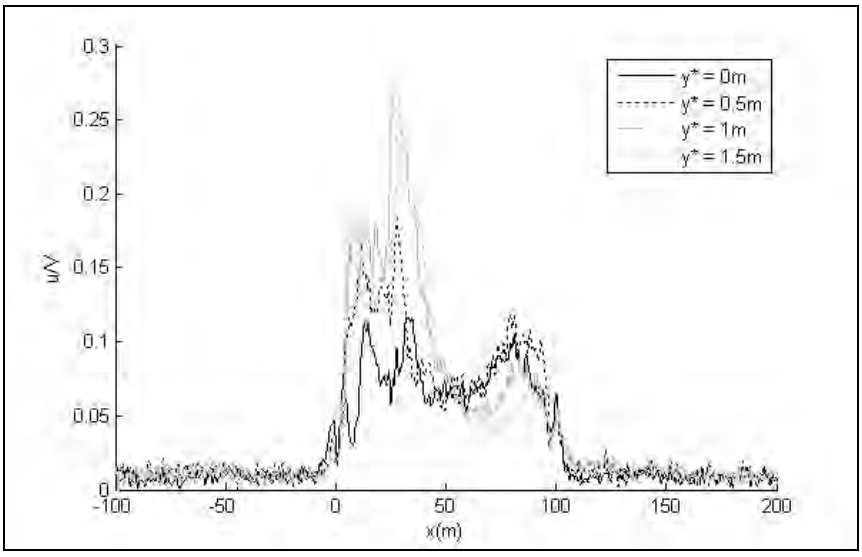

Figure 29. Normalised velocity time histories for measurements taken at *z* = 1.75 m and at different distances from the train centre line.

Evidently, for a given measuring height, velocities decreased with distance from the train side, as seen in Figure 30.

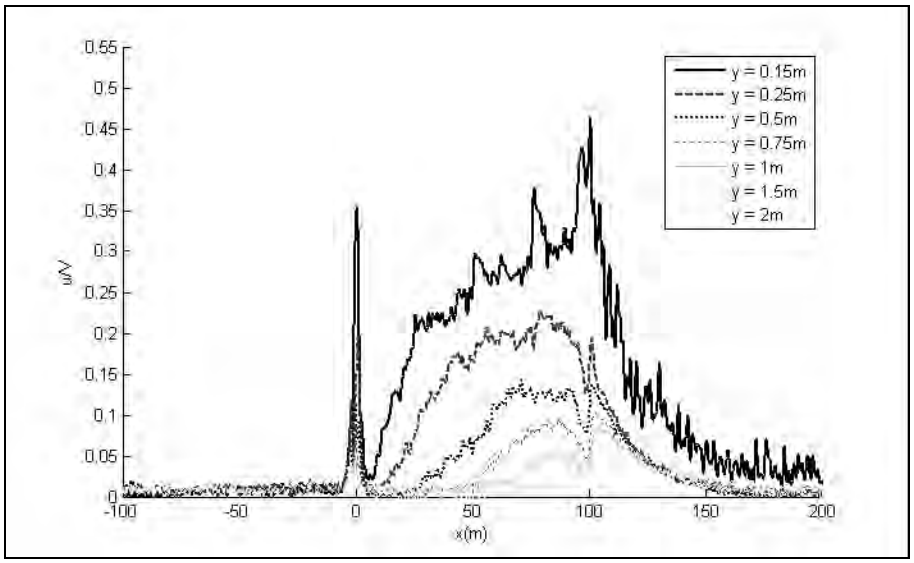

Figure 30. Normalised ensemble mean velocities for measurements at train mid height and at different distances from the model convex side

For a better understanding of the overall normalised velocity flow-field around the train, different contour plots at different cross sections (x given as equivalent full scale distance along the train) of the train were drawn using Matlab. Figures 31(a) to 31(h) below show normalised slipstreams velocities contour plots at the following cross sections: the nose of the train (x = 0 m), the end of the nose (x = 3.5 m), the end of the first carriage (x = 26 m), the end of the second carriage (x = 52 m), the end of the third carriage (x = 78 m), the middle of the fourth carriage (x = 92 m), the beginning of the tail (x = 100 m) in its nose shape and the end of the tail (x = 104 m). Note that in this figure, and in the figures that follow, the shape of the train, indicated by the shaded area is nominal, and represents the bounds of the measurement domain rather than an accurate train shape. These cross sections were selected to carry out the contour plots as it was seen that higher velocities were present at the end of each carriage coinciding with the train inter-carriage gaps, being the highest peak between the third and fourth carriage with a value of 0.7 of the train speed at z = 0.5 m. As seen before, the slipstreams velocities decreased with distance from the model side, becoming almost insignificant at a lateral distance of y = 1 to 2 m from the train side edge. However, it should

be noted that for measurements carried out at the roof of the train, the velocities increased with lateral distance as the measurement point approached the edge of the train; then velocities started to decrease with lateral distance, disappearing again at around y = 2 m from the model side edge.

In terms of the effect of the vertical distance on the slipstream velocities, it was clear that for roof measurements velocities decreased with height from the train top. On the other hand, measurements taken along the vertical axis on the train side increased as the measurement point moved down to the platform and up to the top of the train. Measurements taken closer to the ground plane (z = -0.5 and z = -1) seemed to be very much influenced by the ground and the ambient airflow, and the signal obtained presented more noise, even when the train was away from the measurement point. These contour plots also show how velocities on top of the train started at very low values increasing towards the end of the train nose and having a maximum by the end of the 1st carriage. Then they decreased becoming insignificant by the end of the train. It is important to notice that this velocity maximum was around half the maxima obtained for the train convex side anywhere along the train. It is also possible to see how velocities on the left side of the train were much smaller than on the right side of the train, all along the train (as mentioned in Section 4.1), being only appreciable for the train nose and tail and not lasting more than 0.5 m from the model side. It is noticeable how velocities on the right side of the train presented higher values on the mid-top of the model and close to the ground, along the train, except for the tail were the maxima was located at train mid height and velocities expanded farther from the train side.

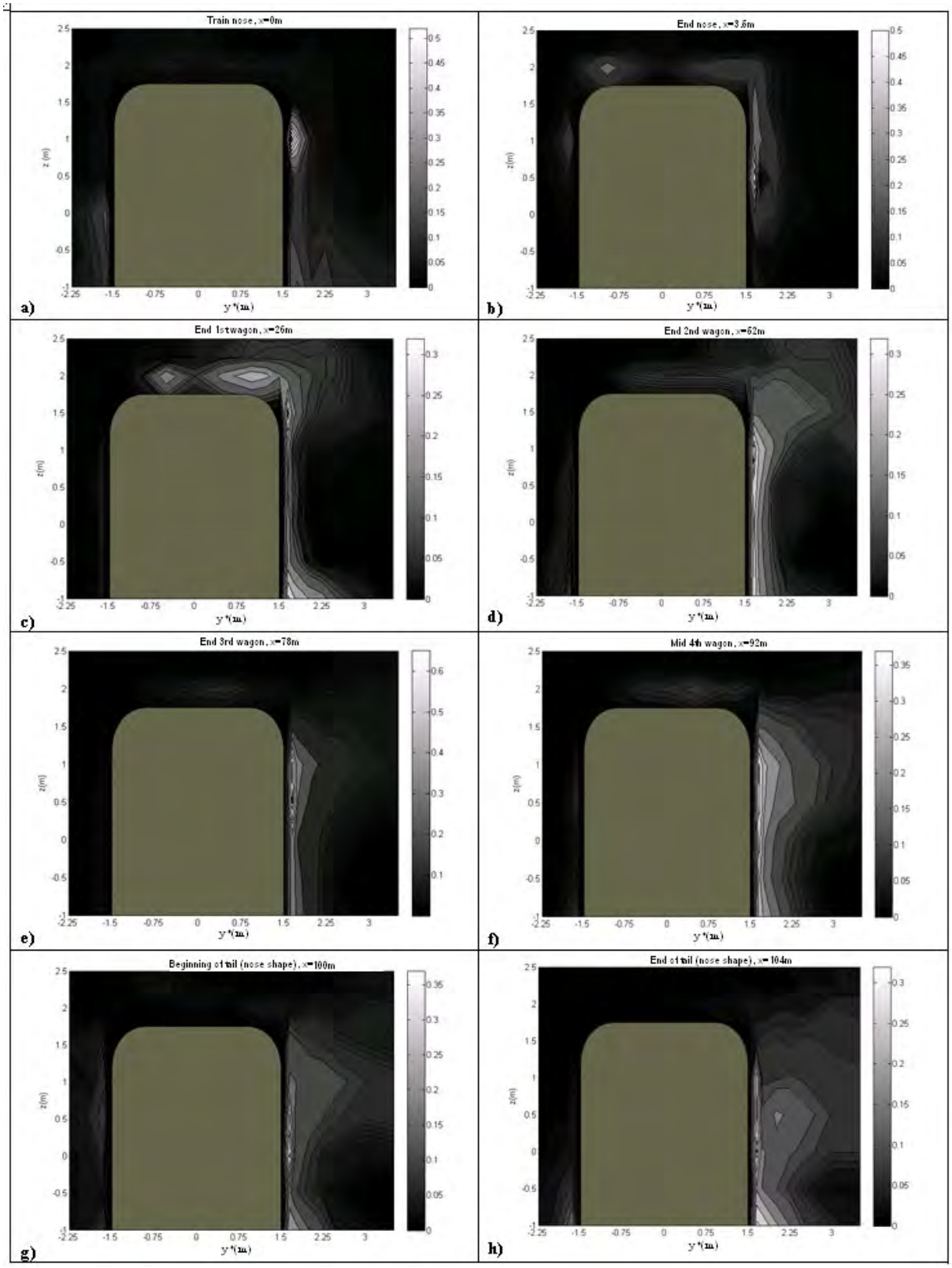

Figure 31. Normalized velocity contour plots at different cross sections along the train (x given as equivalent full scale length along the train). The bottom axis shows equivalent full scale lateral distance and the left axis shows equivalent full scale vertical distance. (a) Train nose, x = 0 m. (b) End of nose, x = 3.5 m. (c) End 1st carriage, x = 26 m. (d) End 2nd carriage, x = 52 m. (e) End 3rd carriage, x = 78 m. (f) Mid 4th carriage, x = 92 m. (g) Beginning of tail, x = 100 m. (h) End of tail x = 104 m.

4.4 Turbulence levels

As in previous studies (Baker, Dalley et al., 2001; Sterling, Baker et al. 2008) the normalised standard deviation of the velocity time histories is used as an indicator of turbulence levels along the train. Figure 32(a) shows, as an example, the normalised average slipstream velocities and standard deviations for measurements taken on the train convex side at train mid height, z = 0, and y = 0.25 m from the train surface. Figure 32(b) corresponds to results for roof measurements carried out at z = 1.75 m and at its centre line, y^* = 0 m.

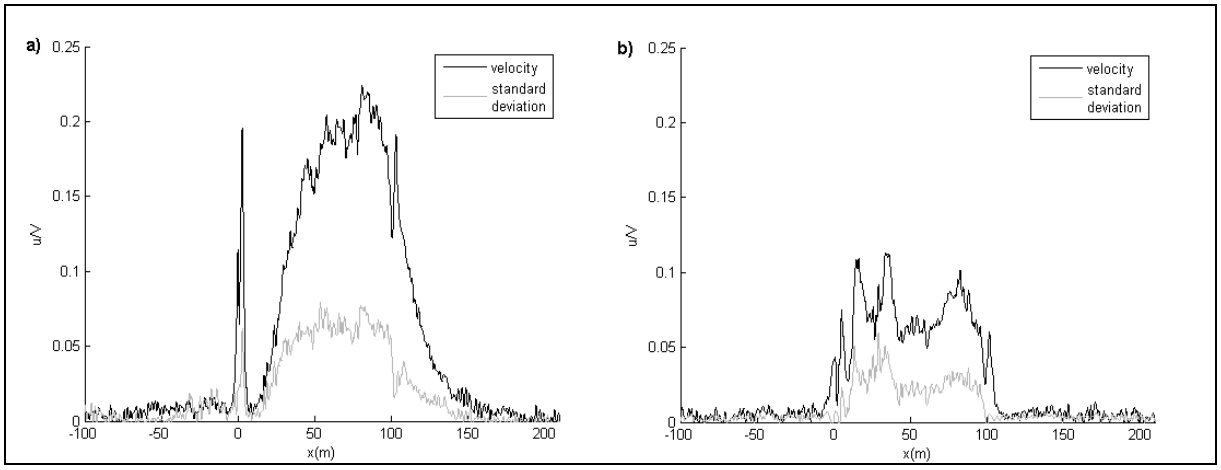

Figure 32. Normalized slipstreams velocity ensemble average (black) and standard deviation (gray). Train speed=16.5m/s. (a) Measurements taken at train mid height (z=0) and y=0.25m from the model convex side. (b) Measurements taken at train centerline (y*=0) and z=1.75m, i.e. 0.25m above the roof.

As stated in references (Baker, Dalley et al., 2001; Sterling, Baker et al. 2008; Baker, 2010), both model and full scale results carried out previously suggest that the nose velocity peak is highly reproducible, with little variation between experimental runs, and can thus be regarded as inviscid. It can be seen that in all cases the ensemble standard deviations are either very small in relation to the ensemble means, or change little from their upstream values. However, in the present experimental set up, this only held true for the roof results but not for the train side measurements, where the standard deviation at the nose of the train took a relatively high value. This could be due to the rejected data due to the positioning of the probes and in some way to the ambient flow altering the position of the nose peak in some of the runs, thus

resulting in more run to run variability. Following the nose peak, as in previous studies (Baker, Dalley et al., 2001; Sterling, Baker et al. 2008) the standard deviation remained small and varied consistently with a growth of turbulence in the boundary layer, for both top and side measurements. The near wake region displayed velocity variability close to the vehicle, and then the standard deviation showed a gradual decrease (as so did the average slipstream velocities) with increasing *x*. This was clear in the side measurements shown above, although the same could not be said for the roof results as the standard deviation fell to zero just at the end of the train. Although, standard deviation results for roof measurements taken at distances of z = 2 m from the train centre line, y^* = 0 m, did show a little increase in the turbulence levels.

Having a closer look to the boundary layer, it could be seen that its thickening was accompanied with an increase in standard deviation and thus in the turbulence level. In order to get a better understanding of the thickening of the boundary layer along and around the train, the boundary layer displacement thickness, d^*, was calculated (Equation 22):

$$d^* = \int \frac{u}{V} dy, \tag{22}$$

for side measurements, where u is the measured velocity and V is the train speed. For top measurements, d* was defined as (Equation 23):

$$d^* = \int \frac{u}{V} dz. \tag{23}$$

The integrations were carried out using simple trapezoidal methods over a range of values of y between 0.15 and 2 m (equivalent full scale distance) for train side measurements, and values of z between 0.25 and 0.75 m for train top measurements.

Note that this definition of the displacement thickness differs from the traditional definition (Equation 24) in which:

$$d^* = \int (1 - \frac{u}{u_e}) dy, \tag{24}$$

where u is the measured velocity and u_e is the free stream velocity. This definition applies to the boundary layer on the surface of a stationary body immersed in a fluid stream of velocity, u_e, whilst the former definition is given for a boundary layer on a surface of a moving body in still air, as defined in Lee and Davis (1972). As explained in Sterling, Baker et al (2008), the two-dimensional definition of the displacement thickness is only marginally appropriate to the three-dimensional flow conditions considered here, but was felt to be a useful indicator of boundary layer development.

The boundary layer displacement thickness was then plotted at different cross sections, where its values were more significant (see Figures 33(a) to 33(d)). As can be seen in the figures, both the roof and the inner concave side of the train presented lower values of the displacement thickness in comparison to those of the outer convex side of the train. The roof displacement thickness was mainly appreciable along the 1st carriage of the train taking its highest value at the end of it, x = 26 m. The inner side displacement thickness was only significant along the train, being mainly noticeable at the end of the 4th carriage (x = 104 m). The outer side displacement thickness varied greatly along the train. As can be seen the boundary layer on the mid-top part of the train side increased as the measurement point moved down the train and similarly at train mid height. The boundary layer at points closer to the platform was quite thick at the end of the first carriage, then it decreased along the 2nd and 3rd carriages to show an increase again at the end of the 4th carriage.

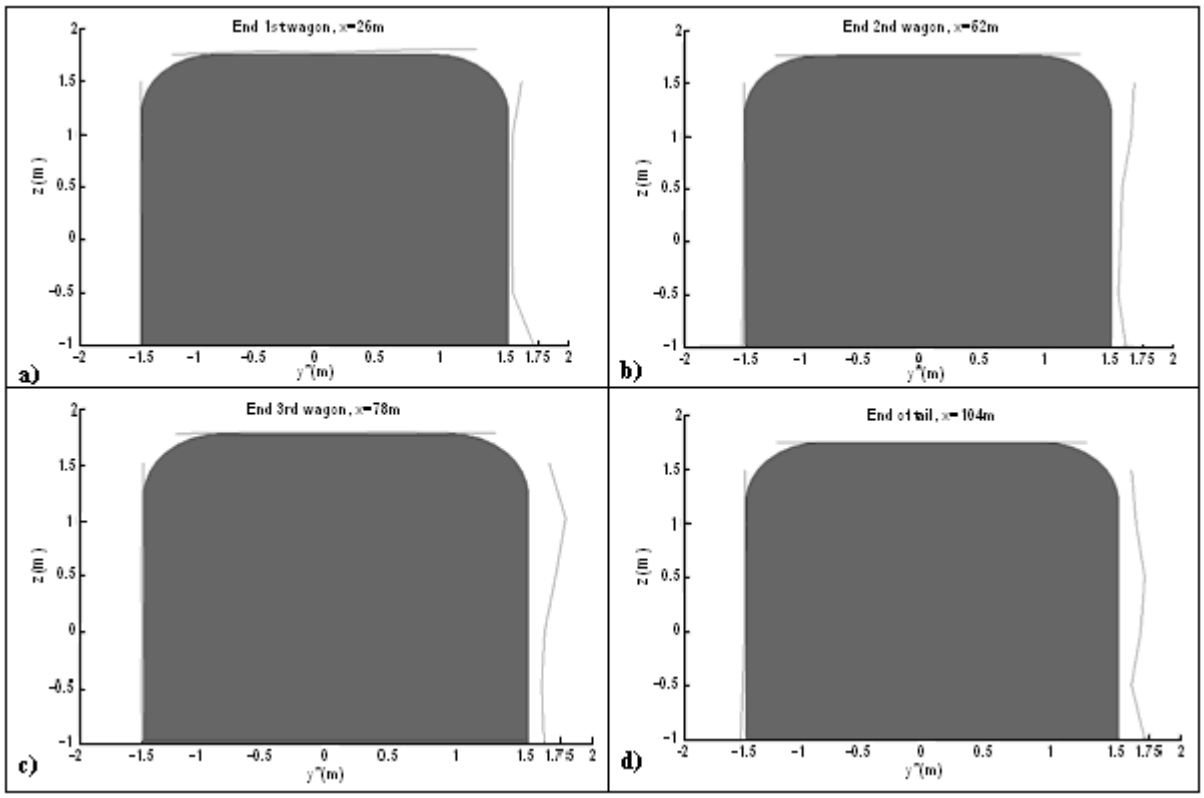

Figure 33. Displacement thickness on train sides and roof. (a) End 1st carriage, *x* = 26 m. (b) End 2nd carriage, *x* = 52 m. (c) End 3rd carriage, *x* = 78 m. (d) end 4th carriage, *x* = 104 m.

To investigate the magnitude of the unsteadiness within the boundary layer the 'turbulence intensity' was also calculated. As explained in Sterling, Baker et al. (2008), this is given by the ratio of the normalised standard deviation of the slipstream velocity ensemble to (1 minus the ensemble mean *u*/V). To help the visualization of the turbulence intensity values, contour plots were constructed at different cross sections along the train, as seen in Figures 34(a) to 34(d). As expected, the higher values of the turbulence intensity were found at the inter-carriage gaps, with the highest value, of 0.4, taking place between the 3rd and 4th carriage at *z* = 1 m and *y* = 0.15 m from the model outer side. Turbulence intensities on top of the train increased along the first carriage getting its maxima (again lower than those registered, at any cross section, for the outer side of the train) at the end of it, *x* = 26 m, and then decreased whilst moving towards the right side of the train until they disappeared at the near end of the 4th carriage, *x* = 104 m. Turbulence intensities for the inner side of the train were mainly

visible at the end of the 2nd carriage, x = 52 m, and along the 3rd, 52 m < x < 78 m, lasting longer closer to the platform. Finally, for the right side of the train, turbulence intensities were located on the top right corner of the train for the 1st carriage and then moved towards the mid-top part of the train for the following two carriages and then they seemed to be concentrated predominately at both mid train height, z = 0, and z = 1 m, along the 4th carriage of the train.

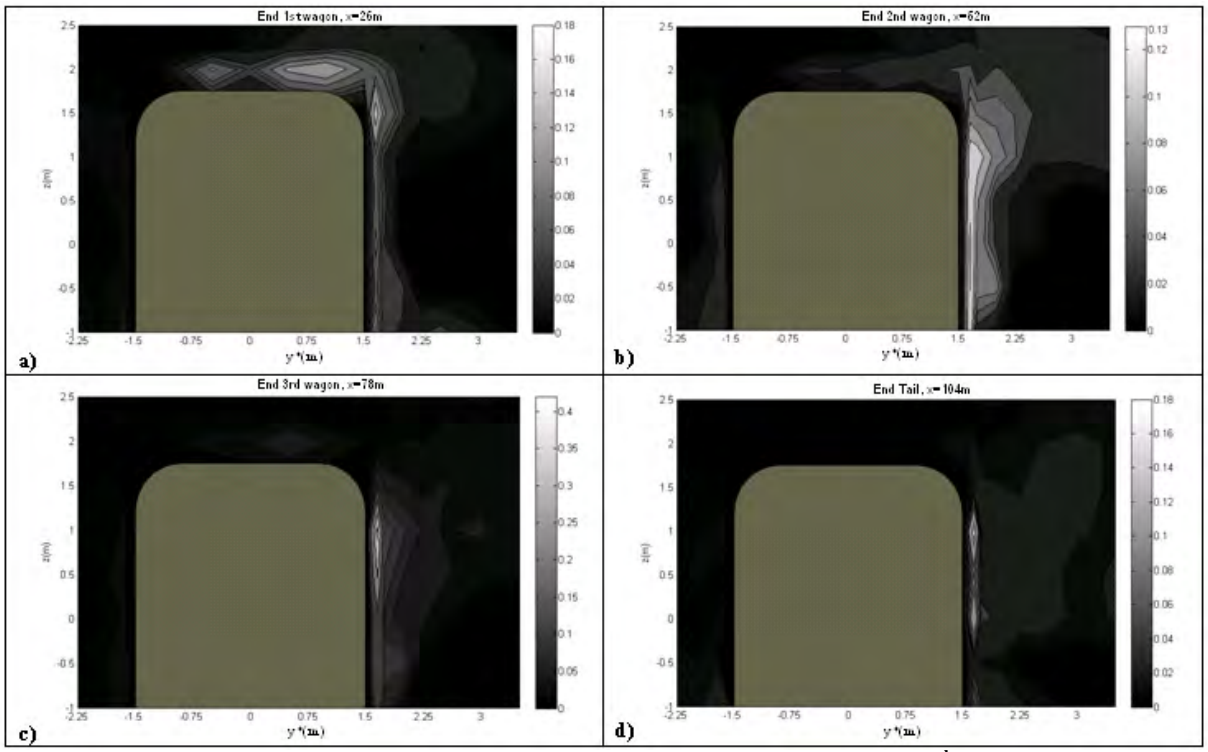

Figure 34. Turbulence intensity contours. (a) End 1st carriage, x=26m. (b) End 2nd carriage, x=52m. (c) End 3rd carriage, x=78m. (d) end 4th carriage, x=104m.

Turbulence intensity contours in the near wake region showed how the turbulence intensity levels fell to 1/3 of the tail turbulence intensity maxima, just after a distance equivalent to a full carriage length, x = 125 m (see Figures 35(a) and 35(b)). However, these results should be handled with care. As it is explained in Sterling, Baker et al. (2008), the velocity measured in the near wake region depends crucially on the phase of the vortex shedding cycle as the measuring instrument is passed, which acts as a warning towards the use of the ensemble averaging technique in the near wake region. In the present experiment, the intermittency of

the near wake peak was clear. For side measurements close to the train, around 65% of the individual runs at the different measuring points (along z) showed a velocity peak just at the end of the train, x = 105 m. However, 5% didn't show any peak at all and 30% showed the velocity peak between x = 105 m and x = 150 m. For top measurements close to the train roof, around 90% of the runs showed the peak at x = 105 m and the rest didn't show a peak at all. In this near wake region it is probably best to look at the wavelet analysis of the individual runs to gain a better idea of the flow structure in this region. The wavelet analysis follows in the next section.

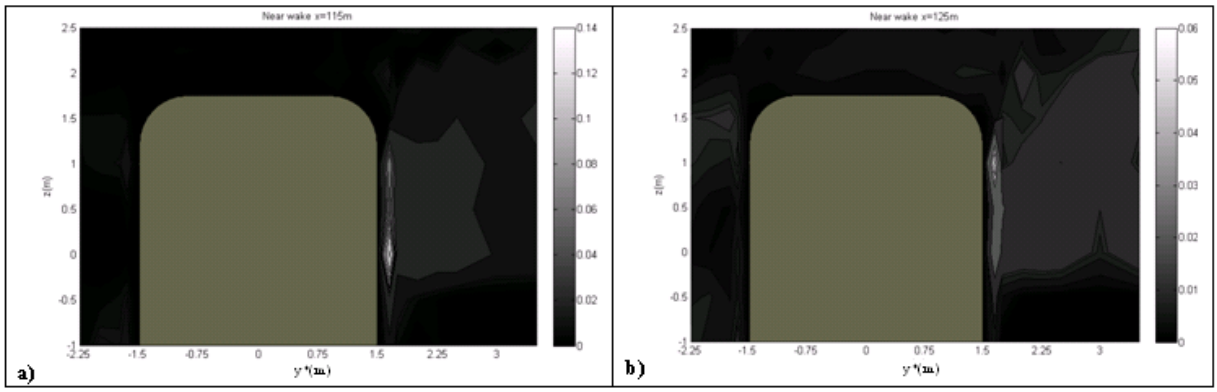

Figure 35. Turbulence intensity contours in the near wake region. (a) x=115m. (b) x=125m.

4.5 Wavelet analysis

Wavelet transforms are useful in the study of turbulence as they enable information about both the frequency content (expressed as a scale or a period) and the spatial structure of the flow to be obtained (Farge, 1992). They are thus ideally suited to the analysis of the highly non-stationary data from the present investigation. As advised in Farge (1992) the continuous wavelet transform was used and the analysis was carried out using a complex valued-wavelet, so that the modulus of the wavelet coefficients follow the signal energy density variations without presenting spurious oscillations. In the present investigation, the complex valued Morlet wavelet was used, because not only the complex nature of this wavelet implied that it was better adapted for capturing oscillatory behaviour, but because the Morlet reflected, as

seen in Figure 36, the type of features present in the time series (which is essential as the wavelet transform is an inner product between the analyzing wavelet at a given scale l and the signal to be analysed). A good summary of wavelet analysis is given by Torrence and Compo (1998) and Valens (2004). The wavelet plots presented here were calculated using the Matlab scripts that can be obtained at Torrence and Compo (n.d.).

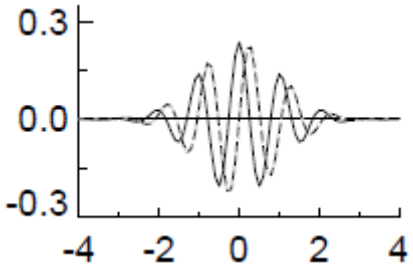

Figure 36. Morlet wavelet. Solid line represents the real part of the wavelet in the time domain, and the dashed line the imaginary part. The scale was s =10dt. (Torrence and Compo, 1998)

The wavelet transform was applied to data obtained from different individual runs at points where the turbulence intensity plots present a maximum. That is, measuring points at y = 0.15 m from the model side and at z values of z = 0 m, z = 1 m and z = 1.5 m.

Out of the 80 laps that were carried out at each measurement point and train speed of 16.5 m/s, it was decided to plot the wavelet power spectrum of 9 different laps (1 every 9 laps – 10% of the total number of laps in any one run). Obviously, as the flow is highly non-stationary, the power spectrum plot differed from one lap to another at each measuring point. However, similar patterns at same scales were identified and it was decided to obtain the average plot for each experimental configuration. Figure 37 below shows the average wavelet power spectrum for a) runs carried out at y = 0.15 m from the model side and at train mid height, z = 0 m, b) runs at y = 0.15 m from the model side and z =1 m above mid height and c) runs at y = 0.15 m from the model side and z = 1.5 m above mid height.

As can be seen in the pictures, the highest powers are at the largest scales and reflect the variations in the overall flow-field. As the period falls, the power also falls. However, in the

three cases it can be seen that as the vehicle is passing the probe at y = 0.15 m from the model side (i.e. well within the boundary layer), there is an enhancement in the power at the smaller scales, reflecting the small-scale turbulence within the boundary layer flow. This effect disappears as the model passes by. It can be seen that for Figure 37(a) from the 1st coach of the train to the last coach there is a slight shift from a period of 0.008 s to a period of 0.004 s and most of the turbulence seems to be located in the last part of the train. However, the opposite holds true for Figure 37(c) the shift is from shorter to longer periods, from 0.002 s to 0.008 s, and the turbulence seems to be located in the first part of the train, 0 m < x < 25 m.

On the other hand, Figure 37(b) presents a more balanced location of the turbulence, where the enhancement of the power is given at periods between 0.002 and 0.008 s for the first and last carriages.

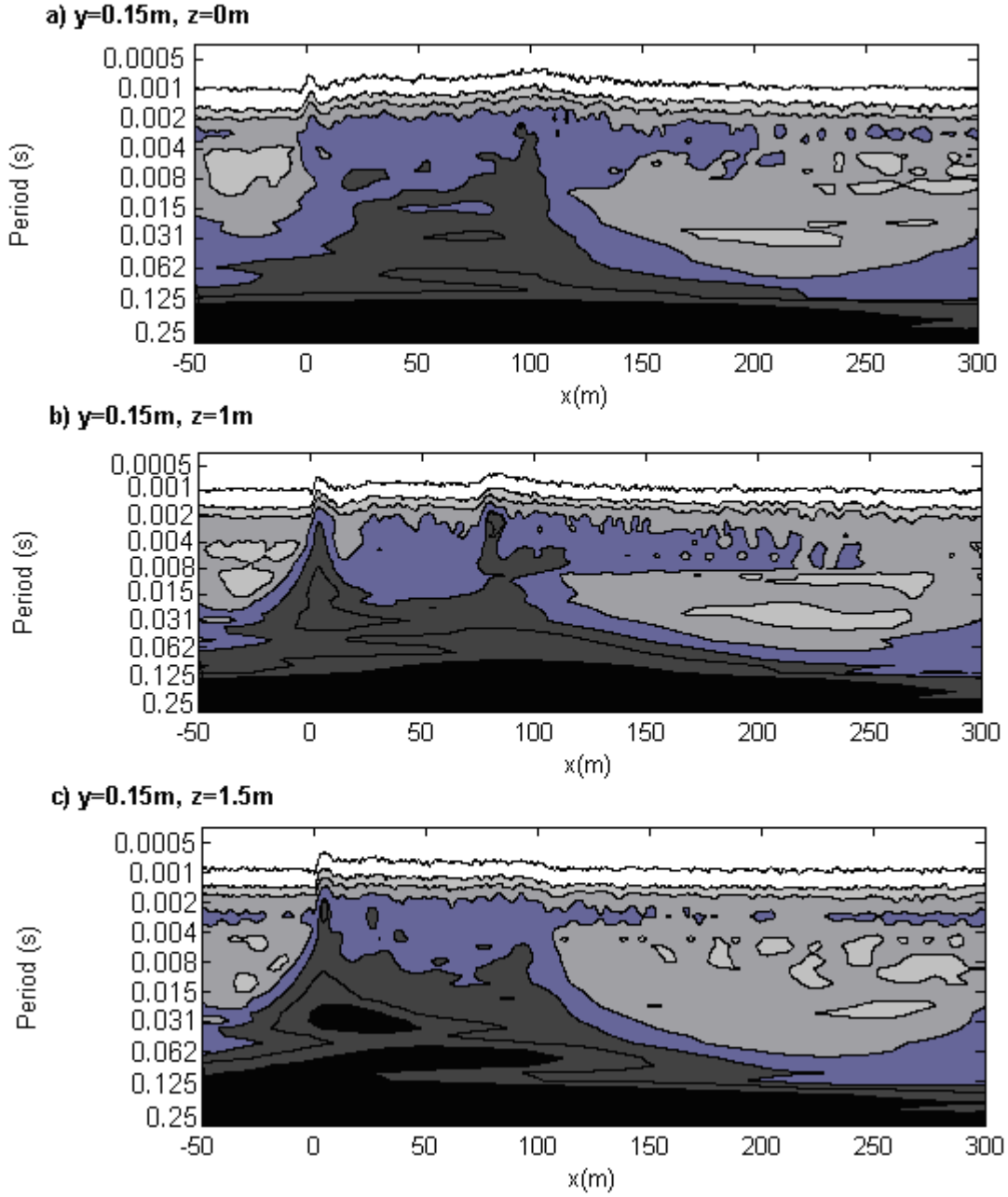

Figure 37. Average wavelet power spectrum for runs at different measuring points, using the Morlet wavelet. The left axis is the corresponding Fourier period (in seconds) to the wavelet scale. The bottom axis is the equivalent full scale length along the train. The nose passes at *x* = 0 m and the tail at *x* = 104 m. The shaded contours represent the contribution of each level to the total power. The levels are (gray scale in which white represents the lowest level and black the highest): [9.3e-10, 1.5e-8, 3e-5, 9.5e-4, 0.0156]

Having said all this it seems that the small scale turbulence within the boundary layer was located initially (as the train passed the probe) at the mid-top of the train and then moved downwards to train mid-height as the end of the train approached the probe.

In terms of the near wake region, just after the train had passed, there was also an enhancement of the power at the lower scales (periods between 0.002 s and 0.004 s), although it remained below the power encountered inside the boundary layer, as expected. It is important to notice that the power present in this region lasted for around a hundred meters after the train had passed, especially at measurements taken at train mid height and z =1 m above mid height.

4.6 Surface Pressure

The movement of trains through the air not only results in significant air flow velocities but also creates a pressure distribution from the flow surrounding it. Generally, when a train passes a pressure pulse is produced (positive peak), by the passage of the train nose, followed by a rapid pressure drop (negative peak), with the entire event occurring in a very short duration. The pressure is generally near ambient along the length of the train, until the tail is reached, where the pressure rapidly falls and then rises (Schetz, 2001; Shui-Hong Lee, 1999; Johnson and Dalley, 2002). The initial rise and fall in pressure as the nose of the train passes is very important for the nose modelling, as this peak to peak change in pressure translates into the maximum force load generated by the moving train on its surroundings (Lee, 1999; Johnson and Dalley, 2002).

Figure 38 shows the ensemble average pressure coefficient time history for measurements taken at different distances from the model outer and inner sides (y = 0.25 and y = 0.75 m) and at different heights (z = -1 m, z = 0 m and z = 1.5 m) for each measuring point. The pressure coefficient is defined as:

$$C_p = \frac{P - P_\infty}{\frac{1}{2}\rho V^2} \tag{5}$$

where *P* is the static pressure, P_∞ is the far-field pressure, and V is the speed of the train.

Similarly to the rejected data present in the slipstream velocities time histories, due to the direction of the flow falling beyond the ±45° cone of acceptance of the probe, the pressure time histories also showed zero values of the measured pressure in all laps. Again, looking at the individual laps within a given run, it was observed that the acceptance data percentage of the overall pressure flow field was very low, around 45-55% depending on the lap under consideration. As found for the velocity flow field, carrying out the ensemble average of the 80 laps, helped diminishing the rejected data significantly, to the point that no rejected data was found in the ensemble average of the pressure time histories, as shown in Figure 38.

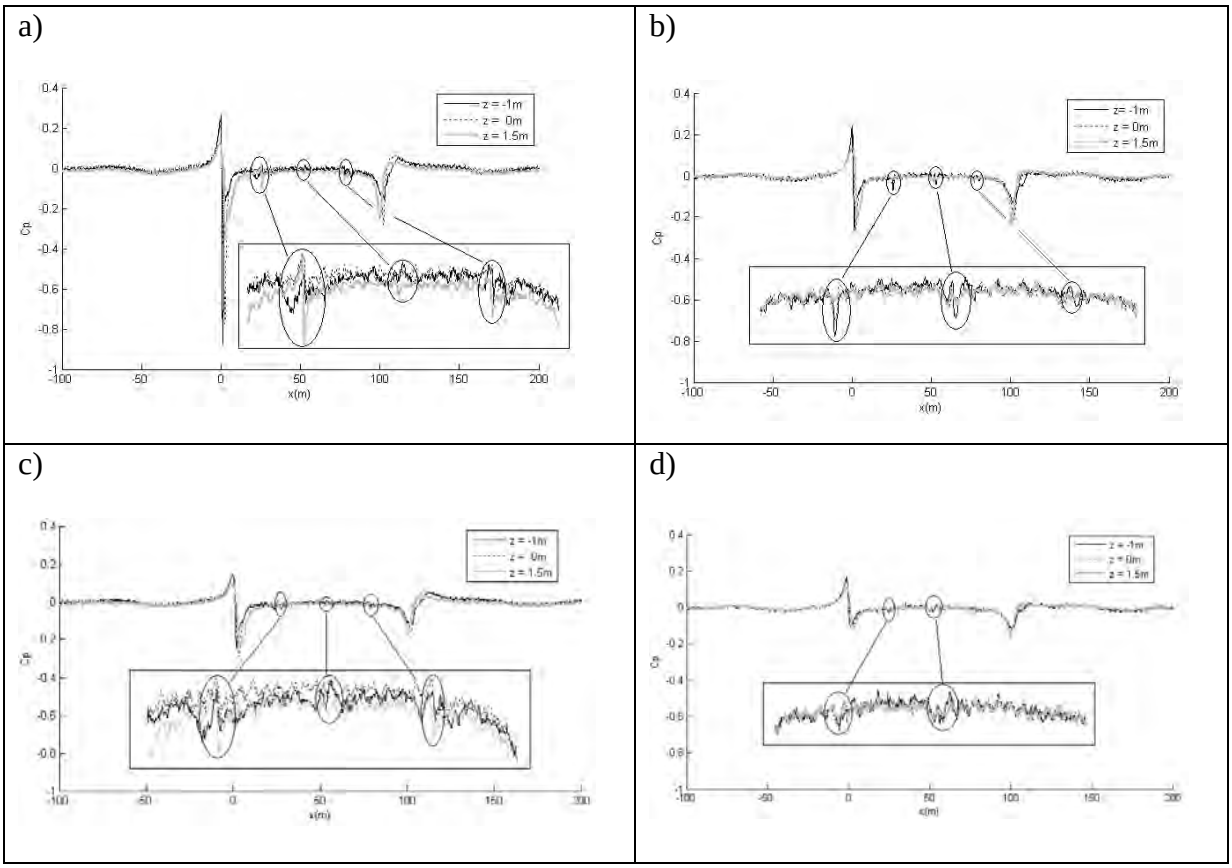

Figure 38. Ensemble average of pressure coefficient time histories for measurements taken at *z* = -1 m, *z* = 0 m and *z* = 1.5 m. a) y= 0.25m from the model outer side, b) *y* = 0.25 m from the model concave side, c) *y* = 0.75 m from the model convex side, d) *y* = 0.75 m from the model concave side.

As can be seen in Figure 38, the effect of each inter-carriage gap on the pressure distribution can be identified as a series of spikes in the graphs (Pope, Baker et al., 2006; Johnson and Dalley, 2002). The influence of these inter-carriage gaps was however different if measurements were taken in the outer convex side or the inner concave side of the train. It is noticeable how for outer side measurements the effect of the gaps was stronger close to the roof of the train (Figure 38(a) and (c)), whilst for the inner side measurements the effect was stronger close to the platform (Figure 38(b) and (d)). As might be expected, the closer to the side of the train the stronger the effect of the gaps. In fact, it was shown that for inner side measurements the effect of the third intercarriage gap was minimal for distances beyond 0.5 m from the train side.

Comparing the nose and wake pressure pulses for the inner and outer side measurements, it appears that the curvature of the train diminished the pressure pulses specially at the nose negative peak and the wake positive peak (becoming near ambient in this area).

It is worth noting the significant pressure drop registered in the nose area at $y = 0.25$ m from the model outer side for measurements below train mid-height and close to the platform, where measurements were very much influenced by the ground and ambient airflow.

Figure 39 shows the pressure distribution along the train for measurements taken at $z = 2.25$ m from train mid height (which corresponds to 0.5 m from the roof of the train) and at different distances from the train centre line, covering the whole roof of the train.

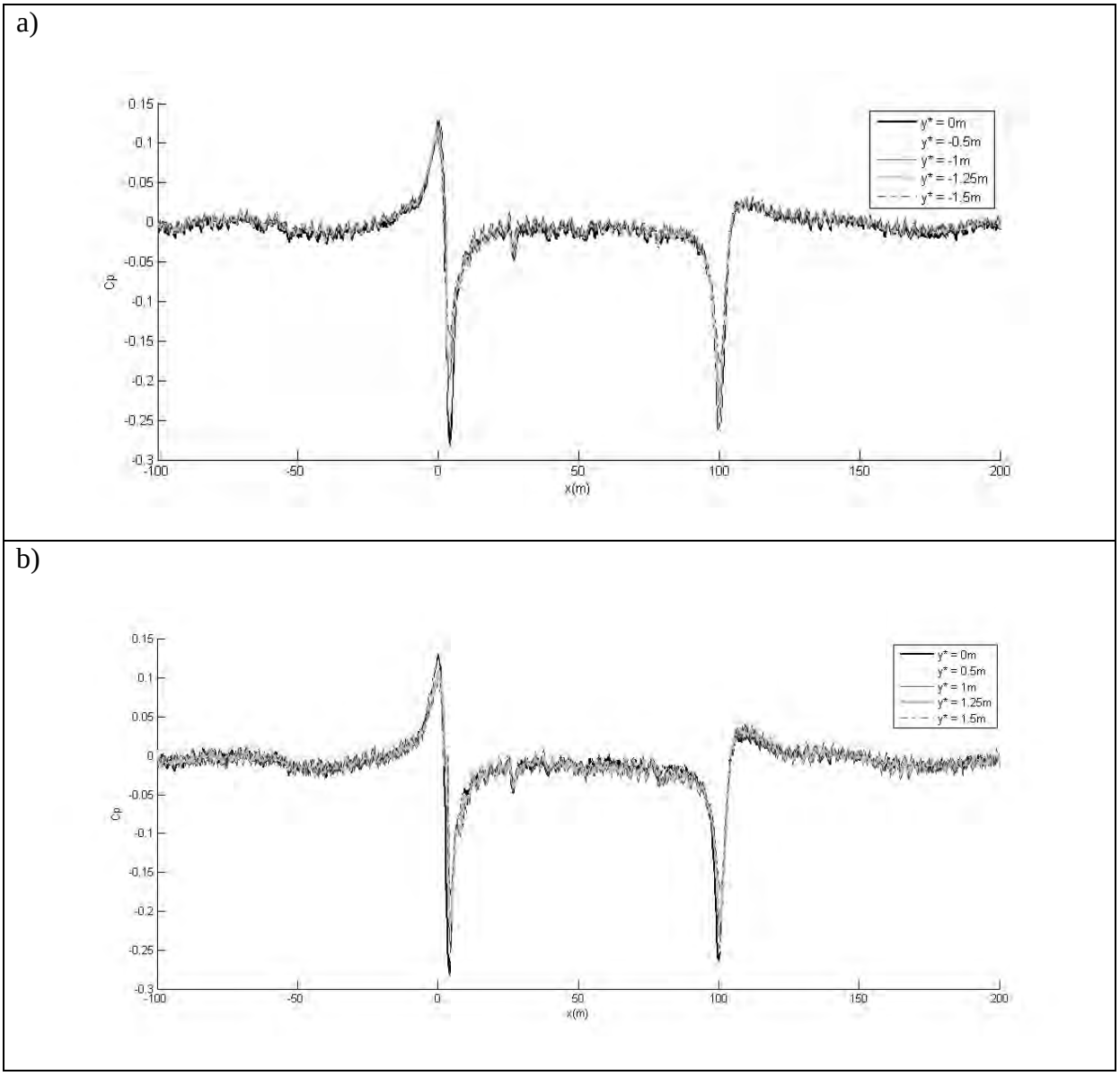

Figure 39. Ensemble average of pressure coefficient time histories for measurements taken at *z* = 2.25 m from mid train height. a) Measurements taken from *y = -1.5 m up to *y** = 0 m, which corresponds to the train centre line. b) Measurements taken form the train centre line *y** = 0 up to *y** = 1.5 m.**

As can be seen in Figure 39, the pressure values registered to the left hand side of the centre line of the train, Figure 39(a), were very similar to those of the right hand side, Figure 39 (b). It is possible to notice that, in both cases, pressures stayed nearly the same for all measuring points, but for the nose and wake negative peaks, where the pressure values obtained

decreased with distance from the train centre line. In terms of pressure fluctuations due to the inter-carriage gaps, only the effect of the first inter-carriage gap was visible.

4.7 Concluding remarks

The results here presented can be summed up as follows:

1. A wind offset of around 0.08 of the wheel velocity was found in all tests. This offset seems to be the result of an ongoing airflow produced by both the train and the movement of the wheel. These wind offset was simply subtracted from the results.
2. The effect of model speed on the experimental results was small if the results were properly normalized.
3. The division of the airflow into a number of flow regions proposed in Baker, Dalley et al. (2001) has been confirmed for this model test. However, the curvature of the rig had a large impact on the inner concave side results, with much lower velocities and lasting less than its convex counterpart.
4. The slipstream velocities results showed that:
    a) On the convex side of the train: velocities increased towards the top of the train and for measurements close to the platform. Higher values were found in the inter-carriage gaps, with the peak velocity registered in between the last two carriages at the right mid-top of the train.
    b) On the roof of the train: Velocities on the roof of the train were smaller than those of the convex side. Higher values were found at the train corners. This is probably due to higher levels of turbulence in the top corner of the train as the roof and side flows come together in this area.
    c) Velocities decreased with distance from the train side.

d) The near wake slipstream velocity peak mentioned in Sterling, Baker et al. (2008) was also present in the ensemble average velocity results all along the side and roof of the train. This peak is an intermittent structure which puts in doubt the use of the ensemble averaging technique in this region.

5. Turbulence results:

a) The curvature of the train also had a large impact on the turbulence results for the inner concave side of the train, with insignificant values of turbulence intensities and much lower values of the boundary layer displacement thickness than its convex counterpart.

b) The standard deviation analysis showed that for train side measurements, the standard deviation at the nose of the train took a relatively high value. This could be due to the low level of data acceptance rate in this area (due to the positioning of the probes) and the ongoing ambient flow altering the position of the nose peak, resulting in high run to run variability.

c) The outer side of the train showed higher values of the displacement thickness in comparison to those of the inner concave side and roof of the train. This also suggests a more rapid boundary layer growth for the convex side than for the concave side and the roof (Baker, Dalley et al., 2001). The boundary layer in the top and bottom parts of the train convex side increased as the measurement point moved down the train.

d) Similarly, turbulence intensities were higher for the convex side of the train than for roof or inner side measurements, with higher values found at the inter-carriage gaps and at mid-top part of the train.

e) Wavelet analysis of the individual runs at different heights along the train outer side showed how the small scale turbulence in the boundary layer was firstly located on the top right corner of the train for the first carriage and then moved down to train mid height when reaching the fourth carriage. The near wake also showed an enhancement of the power at the lower scales, although it remained below the power encountered inside the boundary layer. The power in this region lasted for around a hundred meters after the train had passed.

6. Pressure distribution:

a) The curvature of the train diminished the nose negative pressure pulse and the wake positive pressure pulse, when comparing the pressure distribution results from the convex and concave side measurements of the train.

b) The effect of each inter-carriage gap on the pressure distribution could be identified as a series of spikes in the graphs. For convex side measurements the effect of the gaps was stronger close to the roof of the train, whilst for the inner side measurements the effect was stronger close to the platform. For roof measurements only the effect of the first inter-carriage gap was visible.

CHAPTER 5

5. COMPARISON OF RESULTS WITH EXISTING DATA

To assess the adequacy of the results obtained in the rotating rig with a 1/50th scale model of an idealised four carriage ICE2 train, the results were compared with existing data from experiments carried out on ICE type trains, at model and full scale sizes.

Baker, Dalley et al. (2001) carried out an extensive investigation on the slipstream and wake of a high speed train using a moving model rig (TRAIN rig), owned by Delta Rail, in which a 1/25th scale model of an idealised four carriage ICE2 train was propelled along a straight rail system at speeds of 30 m/s. The velocity field around the model was measured using a rake of hot film anemometers positioned at distances from the model at mid-train height with no platform simulation (Figure 40(a)). The advantage of using such a rig over traditional wind tunnels is its ability to correctly simulate the relative motion between the vehicle and the ground.

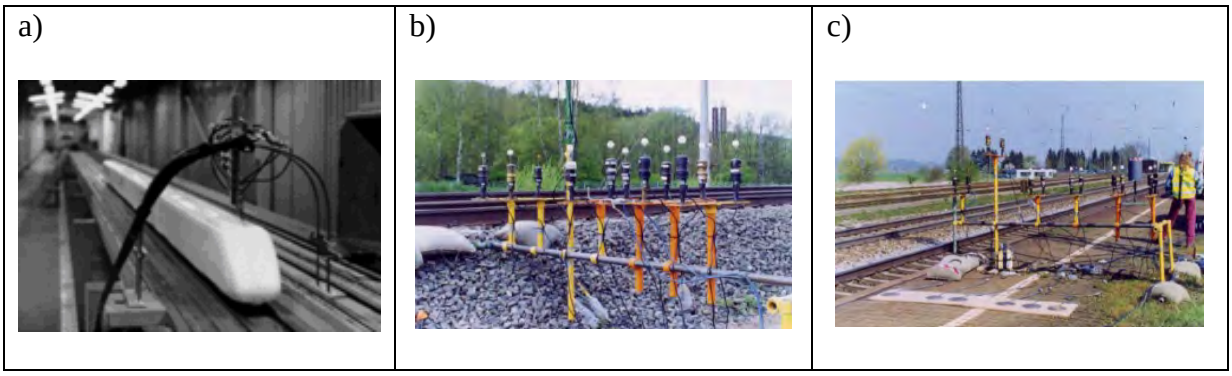

Figure 40. Experimental views. (a) TRAIN rig, (b) DB trackside tests and (c) DB platform tests (Baker, Dalley et al., 2001; Sterling, Baker et al., 2008)

Results from this investigation were also examined in Sterling, Baker et al. (2008), which also gathered results from full scale tests carried out by Deutsche Bahn, DB, (Schulte-Werning, et al., 1999) in Germany using a 14 carriage ICE1 service train travelling at 51 m/s. Slipstream

velocities were measured using gust anemometers both at platform and at trackside (Figure 40(b) and (c)), although only platform measurements are discussed here. The platform tests were carried out at a number of distances from the train side at 1m and 1.34 m above a German height platform, which corresponds to a height of 0.31 m above the rail (as compared to 1 m for the UK platform).

It is worth noting that Johnson and Holding (2003) looked at the influence of this platform height difference on the slipstreams of a 1/25th scale ICE2 model using the Moving Model Rig, and discovered that the higher platform (UK platform, 1 m above the rail) significantly reduced (up to 30%) the contribution to the slipstream of the bogie roughness, affecting the structure of the train slipstream and wake. The peak slipstream air speeds took place in the near wake of the train for German height platforms (0.31 m above the rail), whilst the peak speeds were associated with the train nose passing for UK height platforms (1 m above the rail), as seen in Figure 41.

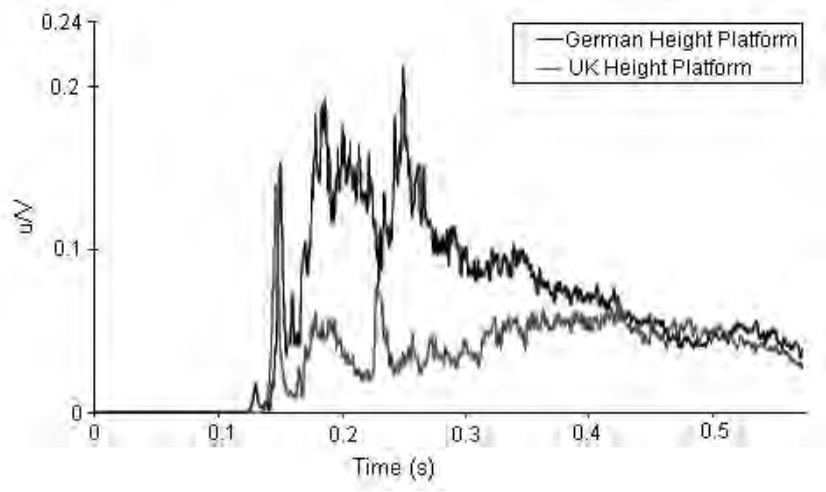

Figure 41. Normalised ensemble averaged slipstream velocities comparison between results obtained in the TRAIN rig for an ICE2 scale model passing a German height platform station (black line) and a UK height platform station (gray line). Train speed = 50 m/s. Measurements taken at equivalent full scale distance of 1m from the train side and 1.335 m above platforms. (Johnson and Holding, 2003)

Full scale data from the DB and BT (Bombardier Transportation) measurements in conjunction with the AEROTRAIN Spanish tests were also available in Quinn, Baker et al.

(2011). Results for the Velaro S103 (quite similar to the German ICE 3 train) were analysed by the authors for a variety of wind conditions. However, results were not directly comparable to the Rotating Rail Rig as the Velaro tests were carried out at 1.525 m from the train side, and at this equivalent full scale distance from the model side in the Rotating Rail Rig, the boundary layer growth was not apparent at any measurement point (not even at platform level). Nonetheless, the Velaro slipstream results showed high resemblance with the flow structure obtained in the rig at distances closer to the train side, as detailed in Section 5.1.

Following the result analysis carried out in Sterling, Baker et al. (2008), a comparison of the ensemble mean slipstream velocities for model and full scale measurements will be carried out followed by a detailed comparison of the flow within specific flow regions.

5.1 Ensemble mean slipstream velocity comparison

Comparing results from the Rotating Rig to those obtained in the TRAIN moving model rig (Baker, Dalley et al., 2001), it was noticeable that the convex side results showed a good resemblance to the TRAIN moving model rig results, as seen in Figure 42. The nose peak obtained in the TRAIN rig at full scale distance of 0.25 m took a normalised value of u/V = 0.23 whilst in the rotating rig this value was 0.2. In addition, the boundary layer values were also remarkably similar. There was a slight difference in the velocity peak at the tail, which was somewhat more apparent in the rotating rail results. However, this peak was noticeable near the ground as reported in Sterling, Baker et al. (2008).

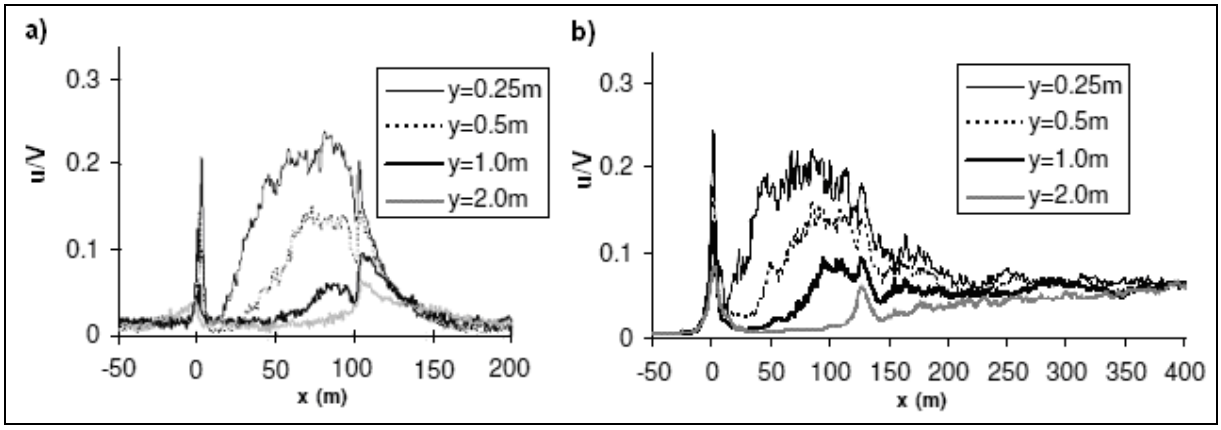

Figure 42. Normalised ensemble average slipstream velocities comparison between results obtained with the rotating rail (a) and those obtained in the TRAIN rig (b). In both cases a four carriage ICE train model was used. The rotating rail used a 1/50th scale model and the TRAIN rig a 1/25th scale model. Measurements were taken at train mid height, z = 0. 20 train passes were ensemble averaged in the TRAIN rig, against 80 for the rotating rail. Again, the x-axis shows equivalent full scale distance along the train, with the tail passing at x = 104 m.

Velocity slipstream results for tests carried out by DB on a full scale 14 carriage ICE1 service train at 1 m above a German height platform (equivalent to 1.31 m above the top of the rail or 0.94 m below train mid height), and various distances from the train side, should have been compared to measurements carried out at z = -1 m from train mid height in the rotating rig. However, as seen in Section 4.3, these measurements were very much influenced by the ground and the ambient airflow, and the signal obtained presented a lot of noise, even for measurements taken far away from the model side. Therefore it was decided to compare the full scale results (reported in Sterling, Baker et al. (2001)) to those obtained in the rotating rig for measurements carried out at z = -0.5 m from train mid height. The results are shown in Figure 43.

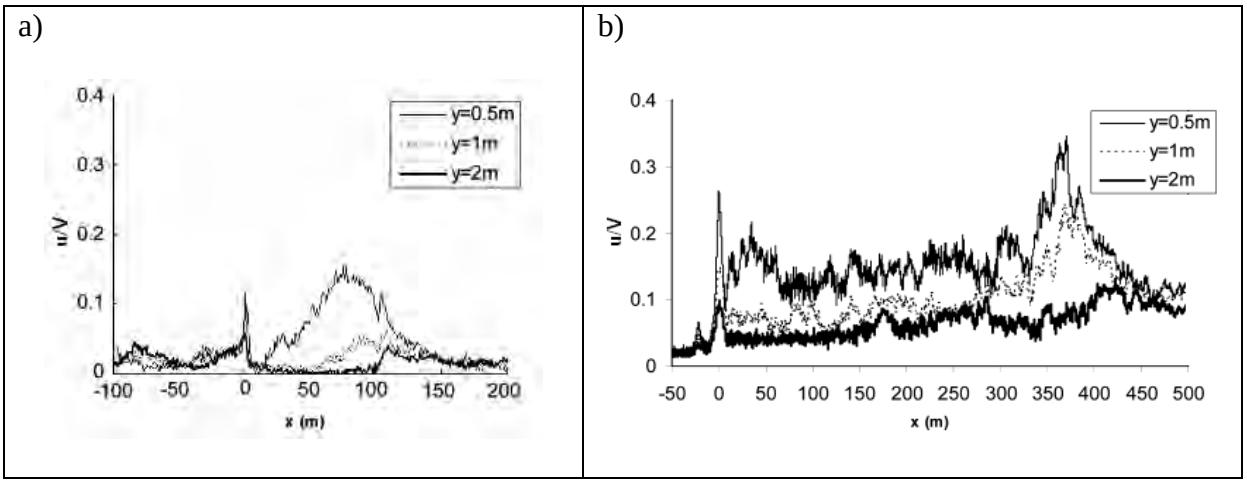

Figure 43. Normalised ensemble average slipstream velocities comparison between results obtained with the rotating rail (a) and those obtained by DB on a full size ICE train (b). The rotating rail used a 1/50th scale ICE2 model and the DB tests used a full size 14 carriage ICE1 service train. Measurements were taken at *z* = -0.5 m from train mid height for the rotating rail tests and at *z* = -0.94 m from train mid height for the DB experiments. 17 runs were ensemble averaged for the full scale tests, against 80 for the model scale tests. Again, the *x*-axis shows equivalent full scale distance along the train, with the tail passing at *x* = 104 m for the rotating rail tests, and *x* = 364 m for the full scale tests.

The model train was only a third of the length of the full scale train, but allowing for this, both the model scale and full scale results showed the same flow regions with a nose peak, a developing boundary layer (except for points beyond 1m from the model side for model scale measurements), an increase in velocity in the near wake region (around x = 100 to 110 m for model scale results and x = 360 to 370 m for full scale measurements) and a decaying far wake. The peak velocity for the full scale measurements was found in the near wake region, whilst it was found in the boundary layer region, in between the last two carriages, for the rotating rig measurements and in the nose region for the TRAIN rig measurements. It is worth noting that for measurements taken on the inner side of the train, the boundary layer velocities were much lower than for the outer side results, and the peak velocity was found in the nose region, responding to the effect of the curvature of the train (as shown before in Figure 26, Section 4.1).

The difference in boundary layer development between the full and model scale tests was noticeable, being more rapid at full scale than at model scale (it can be seen in Figure 43 how at full scale velocities in the boundary layer region increase rapidly right after the nose peak

and stay at similar values along the different carriages, whilst for model scale, velocities in the boundary layer region do not stabilize right after the nose peak, but keep increasing until the very last carriage) probably due to the different configuration of the tests (measurements were taken at different distances from train mid height) and difference in vehicle geometry (one is longer and straight, the other is a third shorter and curved) and, of course, vehicle roughness. The difference in vehicle geometry (i.e. scale) should not be underestimated as a difference in train scale implies a difference in Reynolds number. This difference in Reynolds number has a significant impact on boundary layer development, as this is highly dependent upon Reynolds number (Sterling, Baker et al., 2008). The Reynolds number for the rotating rig tests carried out on a $1/50^{th}$ scale model of an idealised four carriage ICE2 train is 0.58×10^6 (taking V = 16.5 m/s and L = 0.525 m) whilst for the full scale ICE1 service train used in the tests carried out by DB, the Reynolds number is 88.4×10^6 (taking V = 51 m/s and L = 26m). Thus, the difference is Reynolds number is significant and can affect considerably the development of the boundary layer.

However, looking at full scale results (Quinn, Baker et al., 2011) of the Velaro S103ET (aerodynamic shape similar to the German ICE3 train. Length = 200 m) carried out by DB and BT in conjunction with the Spanish AEROTRAIN tests, for measurements carried out at z = 0.2 and z = 1.2 above the top of the rail, and at 1.525 m from the model side, under very low cross wind conditions (wind speed < 2 m/s and yaw angle between -0.5° and 0.5°), it was found that the boundary layer development showed a very developing flow (in terms of continuously increasing velocities throughout the boundary layer region, from after the nose peak until the last carriage), similar to that of the rotating rail found for measurements carried out at distances < 1 m from the model side (beyond 1 m the boundary layer growth was not apparent). This could be due to the significant sensitivity of the train slipstream velocities

even to very low cross winds and yaw angles, as found in Figure 44 in (Quinn, Baker et al., 2011).

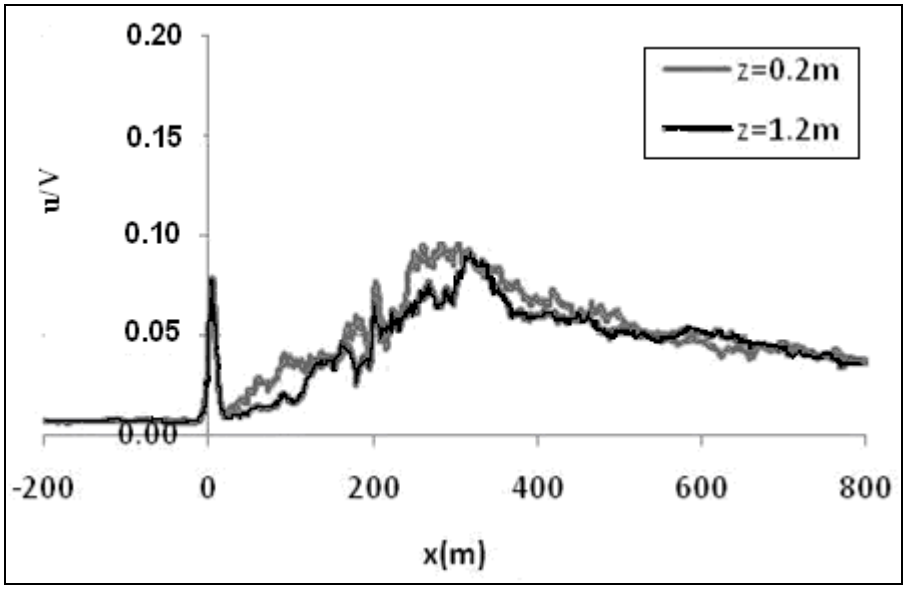

Figure 44. Normalized ensemble average of slipstream velocities for Velaro S103ET tests (20 train passes) carried out by DB and BT in conjunction with the Spanish AEROTRAIN campaign. Measurements were carried out at *z* = 0.2 m (gray curve) and *z* = 1.2 m (black curve) above the top of the rail. Train speed 80m/s. Train length 200m. Low cross wind conditions, yaw angle between -0.5° and 0.5° degrees. (Quinn, Baker et al., 2011).

5.2 Flow regions considerations

In order to assess the flow characteristics of the rotating rail results within specific flow regions, the different flow characteristics were studied around model (Baker, Dalley et al., 2001) and full scale (Schulte-Werning et al., 1999) trains (both considered in Sterling, Baker et al. 2008) within three flow regions: upstream/nose, boundary layer and wake (which will be further divided into a near and a far wake region).

5.2.1 Upstream/nose region

As mentioned in Section 3.5, the rotating rig results for the nose region should be handled with care, as the low level of data acceptance rate in this area (due to the measuring technique) meant that velocities were being rejected all around the nose peak, and in 35% of cases, the peak itself was missing. Furthermore, the ongoing ambient flow altered the position

of the nose peak. Therefore the nose velocity peak that was found to be highly reproducible (little scatter between experimental runs) for model and full scale tests as reported in Sterling, Baker et al. (2008) for ICE2 type trains, instead presented a relatively high standard deviation value in the rotating rail results (Figure 45). In this way, the nose results (without filtering and including rejected data) for the ICE2 scale model measurements carried out in the rotating rail at train mid height and y = 0.25 m from the model side, presented a maximum normalised value of the standard deviation of 0.075 (Figure 45 (a)). It was also found that the nose peak length was shorter in the model scale results, around 5 m (from x = -2.5 m to x = 2.5 m) against 11 m(from x = -5 m to x = 6 m) for the full scale results. At train speeds of 16.5m/s for model scale tests and 51m/s at full scale, this gives a gust duration of 0.3s for model scale against 0.2s at full scale, enhancing in this way the gust effect on passenger instability. Even though at these time scales the gust could cause passenger instability (Jordan et al. 2008), their relatively small magnitude, in comparison to the peaks in the other regions, means that they are unlikely to represent the critical case, as seen in Sterling, Baker et al. (2008).

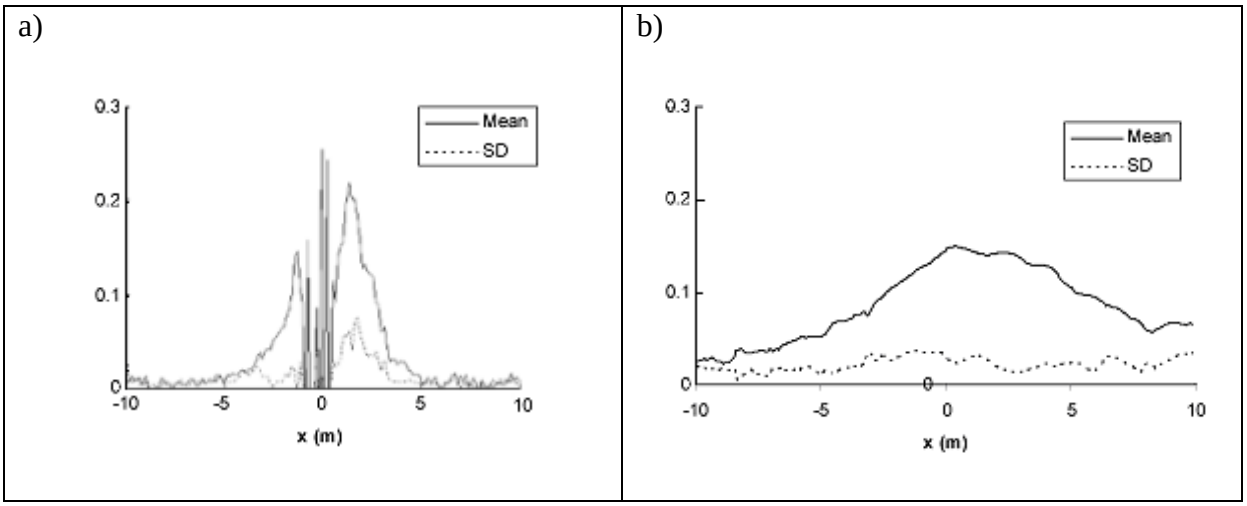

Figure 45. Ensemble mean and standard deviations of slipstream velocities for the upstream/nose region. (a) ICE2 scale model measurements from the rotating rail, y = 0.25 m from the model outer side and train mid height, z = 0 m. Results given without filtering and showing the rejected data. (b) 14 carriage ICE1 service train, platform measurements at y = 1m and z = 1 m.

5.2.2 Boundary layer region

The boundary layer displacement thickness, *d** (Equations (22 and 23) in Section 4.4), has been previously calculated for model and full scale ICE trains as a useful indicator of boundary layer development. Baker, Dalley et al. 2001 studied *d** for a 1/25th ICE2 model scale train in the TRAIN rig facility and Sterling, Baker et al. (2008) later compared these results with full scale size data obtained by Schulte-Werning et al. (1999) on a 14 carriage ICE1 service train in Germany.

Figure 46 shows a comparison between the rotating rail (1/50th scale ICE2 model), the TRAIN rig (1/25th scale ICE2 model) and DB full scale (14 carriage ICE1 service train) results for the boundary layer displacement thickness along the train. It was found that both model scale results showed a substantial boundary layer growth (as indicated by the steep displacement thickness curve in Figure 46), in comparison to the full scale data results, corresponding to the very developing nature of the flow in this region at model scale (which translates into continuously increasing velocities in the boundary layer region). It was also noticeable that full scale data laid above the model scale measurements, even for very small values of *x*. These results suggested a rather different boundary layer development at model scale than at full scale, as found in Sterling, Baker et al.2008. The authors attributed this difference in boundary layer development to Reynolds number effects, since the boundary layer development is highly dependent upon Reynolds number. As mentioned above, there is a considerable difference in Reynolds number at model scale than at full scale, with a value of 0.58×10^6 for model scale tests (rotating rig) and 88.4×10^6 for full scale tests (DB tests). This difference is mainly attributed to model tests being carried out at 1/50th the size of full scale tests. Again, as stated in Sterling, Baker et al. 2008, it was difficult to assess the

Reynolds number effects as model and full scale tests were carried out at different positions from train mid height and the track geometries were different in all tests.

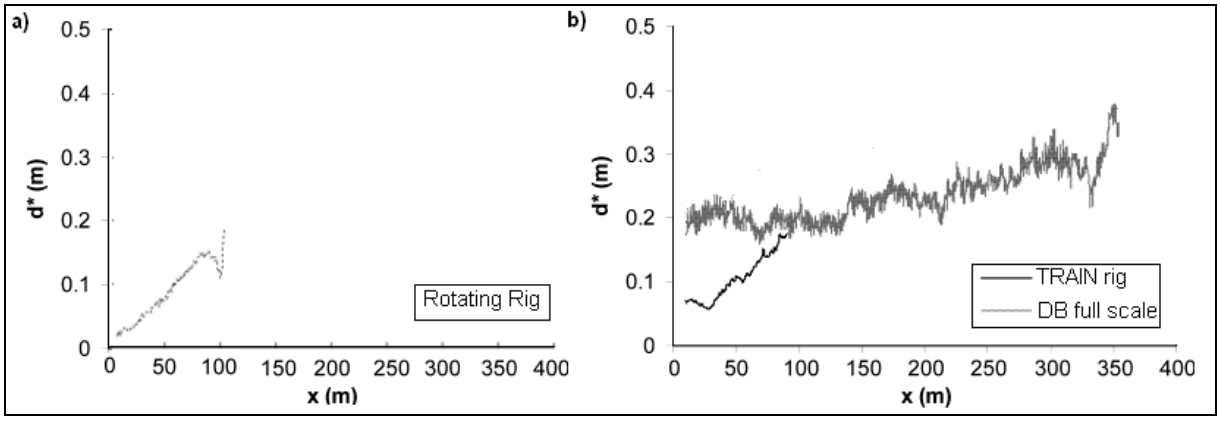

Figure 46. Development of boundary layer displacement thickness along the train for results obtained in the rotating rig with a 1/50th scale ICE2 train model (a), the TRAIN rig, in which a 1/25th scale ICE 2 model was used, and full scale DB results where a 14 carriage ICE1 service train was used (b), from Sterling, Baker et al. (2008). Model scale measurements were taken at train mid height and full scale measurements at *z* = -1 m from train mid height.

Sterling, Baker et al. (2008) calculated the turbulence intensities obtained in full scale measurements and found that the intensities for the 14 carriage ICE1 service train were constant, around 0.04, with distance along the train, reflecting once more the slow rate of boundary layer growth (as indicated by the displacement thickness curve in Figure 46). Taking advantage of the very rapid early development of the velocity in the boundary layer region in full scale experiments, an autocorrelation analysis was carried out (Sterling, Baker et al., 2008) in order to obtain some information on the duration of the gusts in the boundary layer region. The very developing flow (in terms of continuously increasing velocities throughout the boundary layer region, which in turn translate into a substantial boundary layer growth as indicated by the displacement thickness curve in Figure 46) found in the model scale experiments made it impossible to carry out such an analysis, therefore no direct comparisons could be made. For the 14 carriage ICE1 service train results an integral time scale of less than 0.1 s and an integral length scale of the order of 3 to 5 m were obtained

(Sterling, Baker et al. 2008). Gusts with such time and length scales are not sufficient to cause passenger instability (Jordan et al. 2008).

5.2.3 Wake region

Baker (2001) analysed the wake flow of a 1/25th scale model of a lorry and an ICE2 train (experiments carried out in the TRAIN facility) by means of wavelet analysis. A Morlet wavelet base was used, as in the present study (Section 4.5). The analysis was carried out for individual runs of the models on the moving model rig and an ensemble average formed of the wavelet spectra at different dimensionless times, $T = t\mathrm{V}/h$ (where t is the time since the rear of the vehicle passed the measuring point, V is the train speed and h is the train height. Therefore $T = 0$ indicates the passing of the rear of the train).

Baker (2001) plotted the wavelet power multiplied by dimensionless Fourier frequency F (in the case of the Morlet wavelet, the wavelet scale is very close to the inverse of the Fourier frequency, as detailed in Torrence and Compo, (1998)), was plotted against F. The same was done for the rotating rig experiments. Figure 47 shows a comparison between the wavelet spectra of velocity time histories for the 1/50th scale ICE2 train model from the rotating rail and the 1/25th scale ICE2 model from the moving model rig.

To enable a comparison to be made, the rotating rail results were also expressed in dimensionless time T.

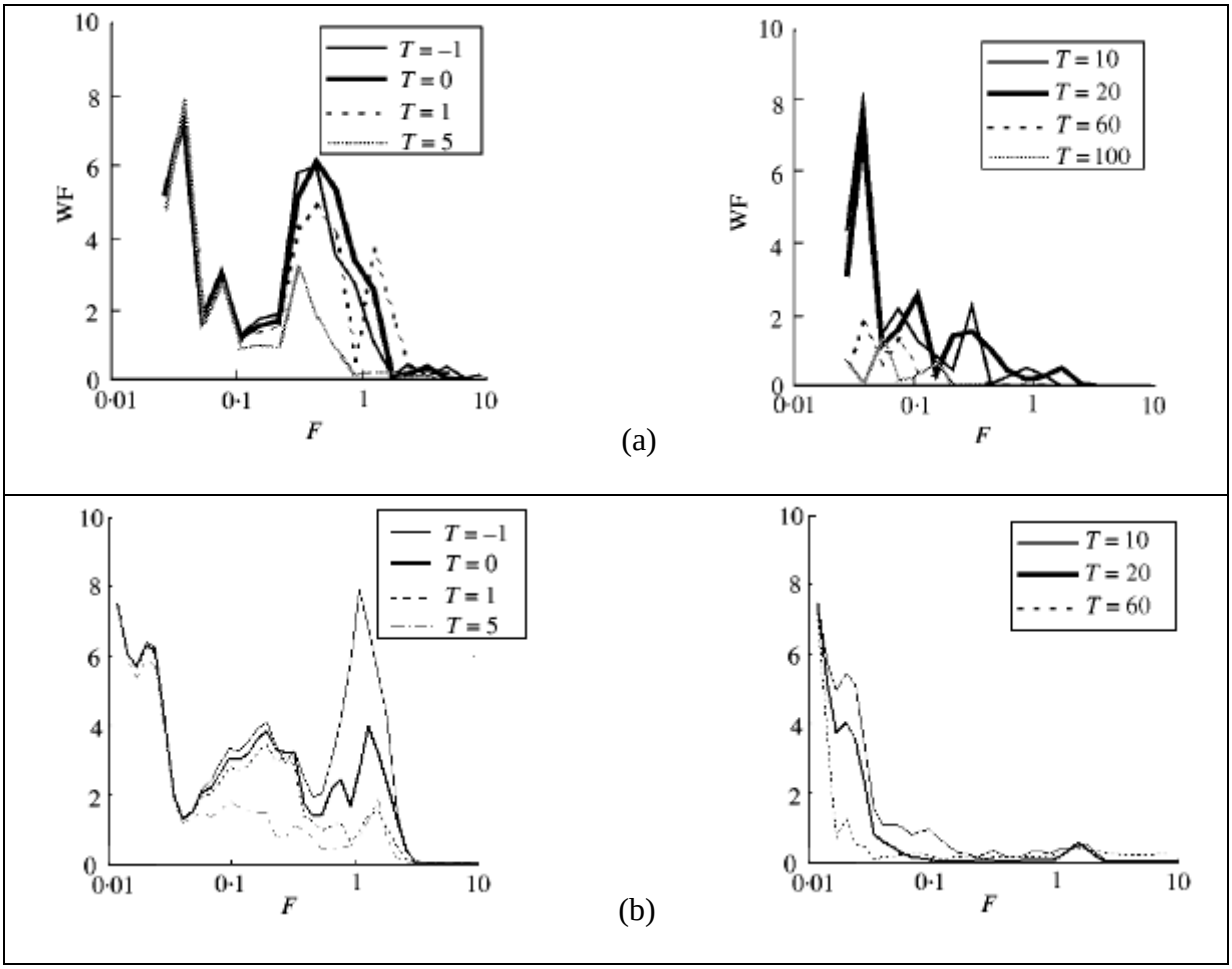

Figure 47. Wavelet spectra of velocity time histories for model train measurements carried out in the TRAIN rig (a), from Baker (2001), and the rotating rail (b). Measurements taken at train mid height and 0.25 m from the model side. Train speed of 30m/s for the TRAIN rig tests and 16.5 m/s for the rotating rail tests. See Baker, Dalley et al. 2001 for experimental details from the TRAIN rig.

It was found that for T < 5, there was a large peak in the spectra at a value of F of about 0.5 for the TRAIN tests. This peak decayed rapidly and disappeared for approximately $T = 10$, see Figure 47(a). In the case of the rotating rail tests (Figure 47 (b)), two large peaks were found for $T < 5$ at values of F of around 0.4 and 1.1. It was very encouraging to find that, similarly to the TRAIN results, both peaks disappeared for $T = 10$. It was also found that for both the TRAIN and rotating rail tests, low frequency oscillations at values of F of around 0.03 persisted downstream of the train (even at values of $T = 20$), which indicated the large scale structure of the far wake region. Therefore the rotating rail results also showed a

difference in wake structure before and after a dimensionless time of $T = 10$, which led Baker (2001) to define the near wake region as the wake region up to 10 vehicle heights downstream the vehicle trailing edge and the far wake region as the wake region beyond that.

5.2.3.1 Near wake

As described in Chapter 2, the large peaks in the spectra found at values of F of around 0.5 to 1, are associated with the separated shear layers from the vehicle. Therefore, as stated in Baker (2001), in the case of high speed trains with a streamlined tail shape, much of the energy in the near wake is associated with the trailing vortex pair at frequencies that are consistent with the fluctuations in the boundary layers on the vehicle surface. These vortices persist until about $T = 10$, before the large structures become dominant.

It was also found, in both model and full scale tests, that the velocity peak in the near wake region was an intermittent structure (as mentioned in Section 4.4), which questions the adequacy of the ensemble average technique to study the flow in this region. Sterling, Baker et al. (2008) were able to realign the data for individual runs (from full scale experiments where a 14 carriage ICE1 service train was used and measurements were taken at 1m below train mid height) and were able to find the velocity maxima for most runs. They found that the gusts length scale was 26.2 m. With an average speed of 51 m/s, this suggested a frequency of oscillation of 1.95 Hz, giving a Strouhal number (with a nominal vehicle height of 3 m) of 0.115. As stated in Sterling, Baker et al. (2008), this indicates the complexity of the wake flow, with the major unsteadiness at Strouhal numbers of 0.1 to 0.15 being dominant close to the ground, with other flow mechanism being significantly higher above the ground (0.5 to 1 in the case of the scale models for measurements at train mid height).

As the nature of the oscillations will be determined to some degree by the nature of the separated boundary layer in the wake, and the boundary layer development is different at

model scale than at full scale (as boundary layer development is highly dependent upon Reynolds number, and this is 150 times smaller at model scale than at full scale), the nature of the wake behaviour may also vary from model to full scale experiments, as shown above. This effect remains to be investigated, although it was clear from the experiments that the model scale results duplicated the main features of the wake flow field.

5.2.3.2 Far wake

As seen in Figure 47, it was also found that low frequency oscillations at values of F of around 0.03 persisted downstream of the train (even at values of T = 20), which indicated the large scale structure of the far wake region. Baker (2001) found that this lower frequency oscillation is either associated with the mechanism of wake pumping, or with large-scale instability of the complete wake structure.

5.3 Concluding remarks

From the comparison of the rotating rig results with the results obtained from model (TRAIN rig) and full scale (DB tests) experiments carried out on ICE type trains, it can be concluded:

1. Overall, the results obtained from the rotating rig measurements are in good agreement with the full scale measurements and reproduce all the important flow features.
2. Not only the division of the airflow into a number of flow regions proposed in Baker, Dalley, et al. (2001) has been confirmed for this model test, but also the convex side results are remarkably similar to the experimental results obtained in the Moving Model Rig (Sterling, Baker et al., 2008), where a 1/25th scale ICE2 train was used.
3. In the upstream/nose region:
    a) Whilst the nose velocity peak was found to be highly reproducible for model and full scale tests (Sterling, Baker et al., 2008), instead presented a relatively

high run to run variability in the rotating rig results due to the measuring technique and the ongoing ambient flow altering the position of the nose peak.

4. In the boundary layer region:
    a) The peak velocity for full scale measurements was found in the near wake region (Sterling, Baker et al., 2008), whilst it was found in the boundary layer region, in between the last two carriages, for the rotating rig measurements and in the nose region for the TRAIN rig measurements (Sterling, Baker et al., 2008). However, for measurements taken on the inner side of the train, the peak velocity was found in the nose region, responding to the effect of the curvature of the train.
    b) Both model scale results (rotating rig and TRAIN rig) showed a substantial boundary layer growth (as indicated by the displacement thickness curve in Figure 46), in comparison to the full scale data results, corresponding to the very developing nature of the flow (which translates into continuously increasing velocities in the boundary layer region) in this region at model scale. This suggest a rather different boundary layer development at model scale than at full scale, probably due to Reynolds number effects (being the Reynolds number at model scale 150 times smaller than at full scale), as mentioned in Sterling, Baker et al. (2008).
5. In the near wake region:
    a) The rotating rail results show a difference in wake structure before and after a distance of 10 vehicle heights downstream the vehicle trailing edge. This confirms the near wake and far wake regions division described by Baker (2001) for other model scale vehicles.

b) For model scale tests (both the rotating rig and the TRAIN rig), the wavelet investigation of the turbulence scales in this region suggests a peak at a Strouhal number of around 0.5-1 at train mid height, taken to be due to shear layer instability. However for full scale measurements, the peak is found at Strouhal numbers of 0.1-0.15, being dominant close to the ground. It may be that the unsteady helical vortex of the train near wake is more important close to the ground, and other types of unsteadiness higher up the vehicle. This indicates the complexity of the wake flow.

c) The near wake velocity peak is found to be an intermittent structure in all types of model and full scale tests.

6. In the far wake region:

a) The rotating rig results also showed, as was the case of the TRAIN results, low frequency oscillations at Strouhal numbers of around 0.03 that persisted downstream of the train, which indicates the large scale structure of the far wake region. This is associated (Baker, 2001) with the mechanism of wake pumping or with large-scale instability of the complete wake structure.

CHAPTER 6

6. COMPARISON OF RESULTS WITH CFD DATA

The main source of CFD (Computational Fluid Dynamics) data on the flow around passenger trains comes from Hemida et al. (2010), where a LES (Large-Eddy Simulation) was carried out to study the transient behaviour of the slipstreams around the rotating model. This paper is shown in full in the Appendices. The ICEM-CFD package was used to create the model geometry and mesh around it. As mentioned in Section 2.4, the LES is computationally more expensive than the Reynolds Average Navier-Stokes (RANS) simulations, but it gives information about the instantaneous flow, which is not possible for RANS. However, Hemida et al. (2010) also investigated the reliability of using the RANS model to predict the slipstream velocity, and performed a RANS simulation using the SST-KOmega model at the same Reynolds number as the LES simulation (77000, based on the train height 0.07 m and speed 16.5 m/s).

6.1 Slipstream velocities comparison

Figure 48 shows the slipstream velocity results, given in terms of the tangential component, for the experimental, LES and RANS results at train mid height and 0.25 m from the model side. Note that the time base was normalised by dividing by L/V, where L is the reference vehicle length and V is the vehicle speed, so that a normalised time, t, of 0 corresponded to the vehicle front passing the instrument rake, and a normalised time of 4 indicated the passing of the final vehicle. The LES results were obtained for both the inner and outer surfaces of the train and once more, as shown in Section 4.5, the difference in velocity distribution due to the rotation of the train was apparent, with significantly lower velocities for the concave (inner)

side of the train than for its convex counterpart. Both the LES and RANS results underestimated the nose peak, which is probably related to the alignment of the Cobra probe, as mentioned in Section 3.5. Furthermore, the LES and RANS results showed a region of negative velocity, indicating separation of the flow close to the nose area. The experimental results did not show this separated flow region as the probe was not able to measure the reversed flow. However, the LES and RANS results were consistent with experiments carried out by Muld, Efraimsson et al. (2009), which also showed this separated flow region close to the nose of the train (PIV measurements carried out on a straight Aerodynamic Train Model consisting of four cars).

Generally, the LES results reasonably agreed with the experimental data. However, the RANS simulation overestimated the slipstream velocities.

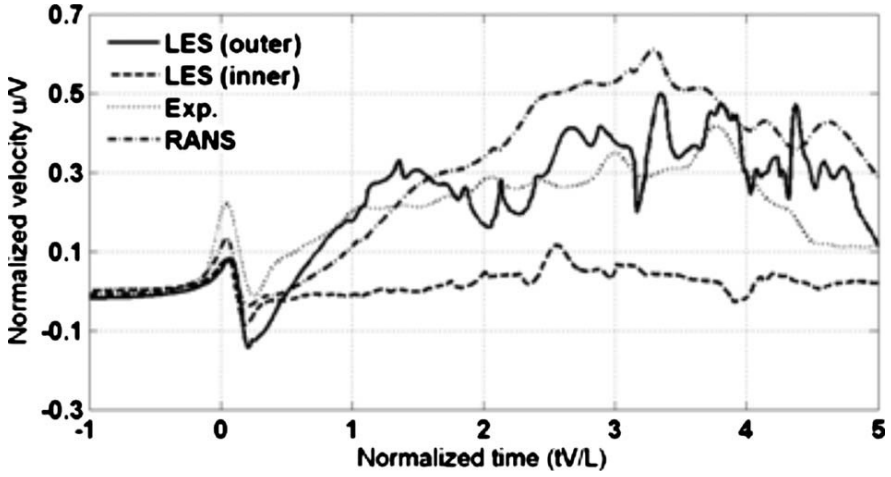

Figure 48. Slipstream velocities results comparison for experimental measurements, LES and RANS simulations of a 1/50th scale ICE2 train model in a rotating rig. Experimental measurements taken at y=0.25m from the model outer side and train mid height. CFD measurements taken at train mid height and *y* = 0.25 m from the model side. Re = 77000. (Hemida et al., 2010)

6.2 Boundary Layer and wake

The CFD results of Hemida et al. (2010) showed a clear influence of the inter-carriage gaps on the boundary layer displacement thickness that was not apparent in the rotating rail results. As can be seen in Figure 49, the normalised displacement thickness (the height of the train is

used to normalise the displacement thickness), based on both the total velocity magnitude and the lateral component, was reduced before the inter-carriage gap and increased behind it. This jump in the displacement thickness was not appreciable at model or in the full scale tests, as seen in Figure 46 in Section 5.2.

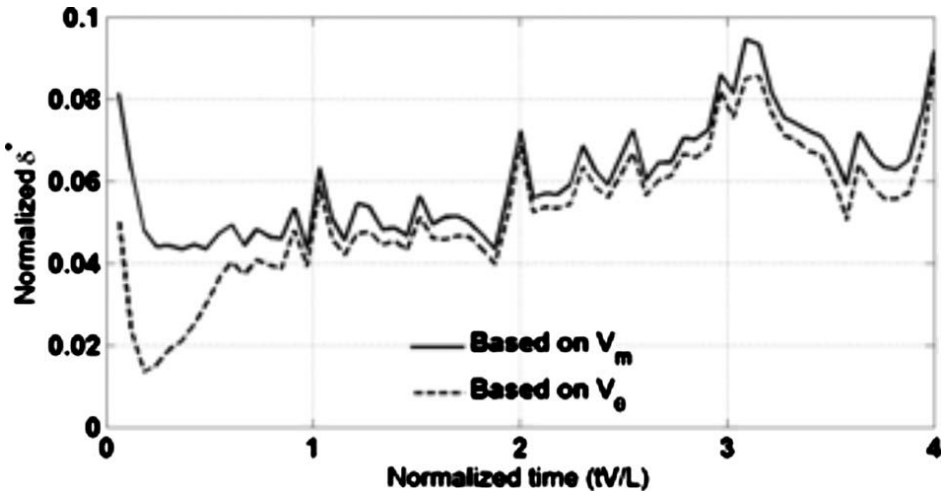

Figure 49. Normalised displacement thickness at half train height on the outer side. Re = 77000 (Hemida et al., 2010)

Hemida et al. (2010) also looked at the boundary layer thickness given as the distance from the surface of the train to the place in the slipstream where the velocity of the flow drops to 95% of the speed of the train, see Figure 50.

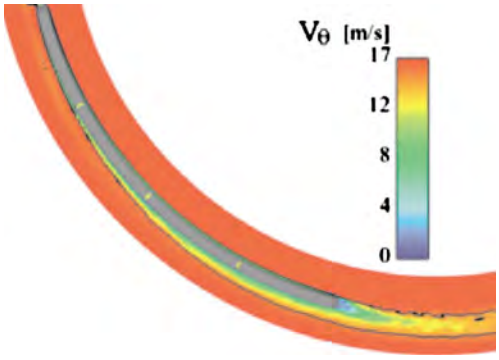

Figure 50. Plane at train mid height colored by the relative tangential velocity, showing the boundary layer thickness. Re = 77000 (Hemida et al., 2010)

By doing so, they found that the boundary layer grew along the train length with a thickness equal to about twice the height of the train near its tail. They also found that the outer part of

the slipstream was dominated by large vortex structures, which grew in size along the train length and extended a long distance in the far wake flow behind the train, which corroborates the findings of Section 5.2.3, for the train wake. In a similar manner, Muld (2010) carried out a Detached Eddy Simulation (DES, a hybrid LES/RANS model) on an ATM geometry (Aerodynamic Train Model) to study the flow structure in the train wake. It was found that the main flow topology consisted of two counter rotating vortices oscillating at a Strouhal number of 0.15. As mentioned in Section 2.2.1, Schulte-Werning et al. (2003) used conventional unsteady RANS CFD techniques to study the forces on the tail cars of high speed trains and identified a steady near wake oscillation with the shedding of longitudinal vorticity from low levels in the rear of the train (see Figure 9, Section 2.2). A well defined oscillation was found at a Strouhal number of 0.14, similar to the 0.11 value found by Sterling, Baker et al. (2008) for full scale tests of a 14 carriage ICE1 service train. It thus seems that the helical vortices in the train near wake undergo some sort of regular oscillation with a Strouhal number of around 0.11 to 0.15. As mentioned in Section 5.2, for model scale tests, the wavelet investigation of the turbulence scales in the near wake region suggested a peak at a Strouhal number around 0.5-1 (taken to be due to shear layer instability). As the model measurements were made higher up the train than the full scale measurements, it may be that the unsteady helical vortex motion is more important close to the ground, and other types of unsteadiness higher up the vehicle. Further work is required in this area.

6.3 Surface Pressure

In the present rotating rail experiments the set up of the probe support (see Figure 20 in Section 3.3) made it impossible to carry out measurements beyond $z/H = 0.2$ (H is the reference vehicle height). However, the CFD simulations of Hemida et al. (2010) allowed measurements to be carried out all around the train, even on its bottom surface. Thus the

authors were able to shed some light on the effect of the supporting cylinders (the bolts that attached the train to the rail) on the surface pressure distribution. Figure 51 shows the pressure distribution expressed in terms of the local pressure coefficient (Equation 5 in Section 4.6) for the top and bottom faces of the train at its centre line.

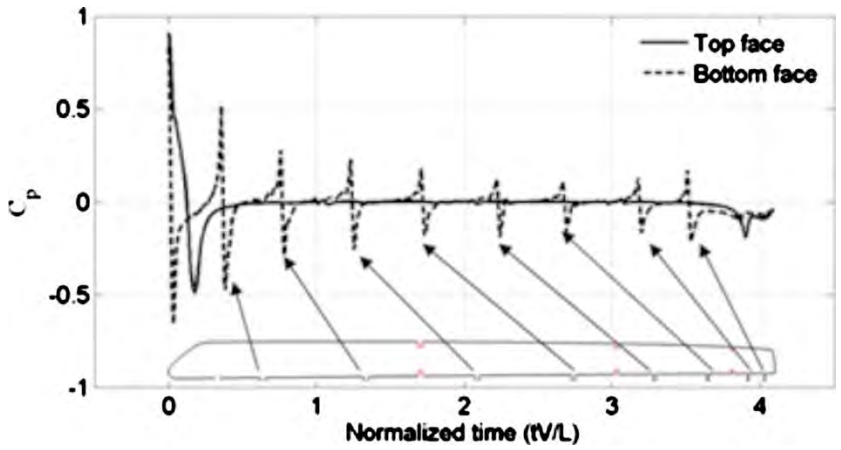

Figure 51. Surface pressure coefficient on top and bottom faces of the train at its centre line. (Hemida et al. 2010)

It was found that the influence of the inter-carriage gaps was not as significant as that of the supporting cylinders. The influence of the supporting cylinders was still visible at measurements of $z/H = 0.1$ and at a distance of $0.1H$ from the outer surface of the train, as seen in Figure 52. This figure shows the time averaged values of the pressure coefficient for measurements carried out at $0.1H$ from the model outer side and at different train heights. It was found that there was no significant change in the value of *Cp* along the train height. However, the influence of the supporting cylinders and inter-carriage gaps was visible close to the platform.

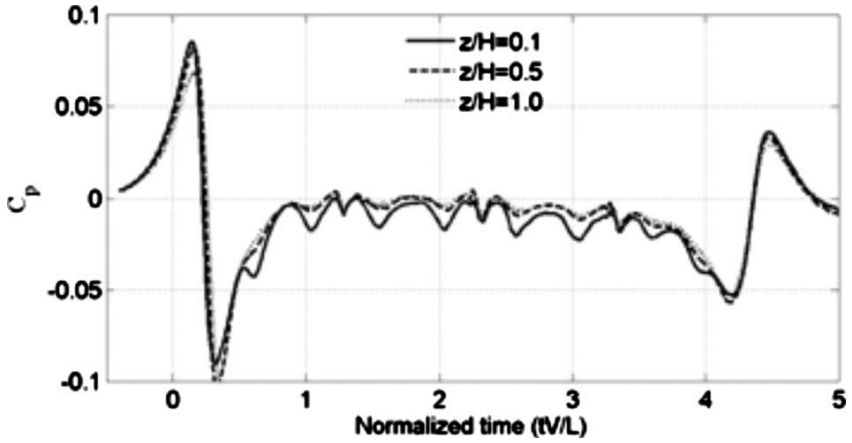

Figure 52. Pressure coefficient at 0.1*H* from the model outer side and at different heights. (Hemida et al. 2010)

The rotating rail results did not show such a strong influence of the supporting cylinders, even for measurements close to the platform, as the rig set up introduced brushes that closed the gap between the train and the platform edge (which were not included in the CFD simulation). Thus the *Cp* distribution results of the rotating rail tests mainly showed the effects of the inter-carriage gaps. As mentioned in Section 4.6, for measurements carried out at 0.07*H* (*y* = 0.25 m) from the model outer side, the effect of the gaps was stronger close to the roof of the train (see Figure 38(a)) than close to the platform.

6.4 Concluding remarks

From the comparison of the CFD data on the flow around the rotating model and the rotating rig results it is possible to conclude:

1. Generally the LES and RANS results reasonably agreed with the experimental data. Results also showed the different flow regions proposed in Baker, Dalley et al. (2001) and showed the impact of the curvature of the rig on the velocities, with lower slipstream velocities on the inner concave side of the train than on its convex counterpart.

2. The LES and RANS results showed a separation flow close to the nose area that was not appreciable in the experimental data, but were consistent however with PIV measurements carried out on an ATM (Muld, Efraimsoson et al., 2009).
3. Differently to the rotating rig results, the CFD results showed a clear influence of the inter-carriage gaps on the boundary layer displacement thickness.
4. Similarly to the rotating rig results, the CFD simulations showed a thicker boundary layer development on the convex side of the train than on the concave side.
5. The outer part of the slipstream was found to be dominated by large vortex structures, which grew in size along the train length and extended a long distance in the far wake flow behind the train, which corroborates the findings of Section 5.2.3 for the train wake.
6. Different types of CFD simulations confirmed the existence of a near wake oscillation at Strouhal numbers of around 0.11 to 0.15, close to the ground, which was also found at full scale tests.
7. The CFD simulations allowed carrying out measurements all around the train (which was not possible at model scale given the configuration of the rig) and it was found that the influence of the under-body of the train on the pressure distribution was higher than that of the inter-carriage gaps, especially close to the ground.

CHAPTER 7

7. CONCLUSIONS AND FURTHER WORK

From the results presented in the preceding sections, the following main conclusions can be drawn:

1. The division of the airflow into a number of flow regions proposed in Baker, Dalley et al (2001) has been confirmed for this model test. However, the curvature that the rig introduces has a large impact on the inner concave side results, with much lower velocities and lasting less than its convex counterpart. Nevertheless, the convex side results are remarkably similar to the experimental results obtained in the Moving Model Rig (Sterling, Baker et al. 2008), where a $1/25^{th}$ scale ICE2 train was used.
2. In the upstream/nose region:
   a) The rotating rig results for the nose region should be handled with care, as the low level of data acceptance rate in this area (due to the measuring technique) meant that velocities were being rejected all around the nose peak. Furthermore, the ongoing ambient flow due to the movement of both the train and the wheel altered the position of the nose peak. Therefore the nose velocity peak presented a relatively high run to run variability.
   b) The LES and RANS results carried out by Hemida et al. (2010) showed a separation flow close to the nose area that was not appreciable in the experimental data, but were consistent however with PIV measurements carried out on an ATM (Muld, Efraimsoson et al., 2009).

3. In the boundary layer region:
    a) The main difference between the inner concave side of the train and the outer convex side of the train is that again, due to the curvature of the rig, velocities for the inner side are much smaller than for the outer side (also found in the CFD simulations carried out by Hemida et al. (2010)). This also translates in much lower values of the displacement thickness and in insignificant values of turbulence intensities.
    b) Velocities on the outer side of the train seem to increase towards the top of the train and when measuring close to the platform. Higher values are found in the inter carriage gaps.
    c) Velocities on the roof of the train are smaller than those of the outer side and seem to be higher at the train corners. This is due to higher levels of turbulence in the top corner of the train as seen in the turbulence intensity contour plots (Figure 34).
    d) The peak velocity for the full scale measurements was found in the near wake region (Sterling, Baker et al., 2008), whilst it was found in the boundary layer region, in between the last two carriages, for the rotating rig measurements and in the nose region for the TRAIN rig measurements (Sterling, Baker et al., 2008). It is worth noting that for measurements taken on the inner side of the train, the boundary layer velocities were much lower than for the outer side results, and the peak velocity was found in the nose region, responding to the effect of the curvature of the train.
    e) Both model scale results (from the rotating rig and TRAIN rig) show a substantial boundary layer growth (as indicated by the displacement thickness curve in Figure 46), in comparison to the full scale data results, corresponding to the very developing nature of the flow in this region at model scale (which translates into continuously increasing velocities in this region). This suggests a rather different boundary layer

development at model scale than at full scale, probably due to Reynolds number effects, as mentioned in Sterling, Baker et al. (2008).

f) As was seen in the TRAIN rig experimental results (Baker, Dalley et al. 2001), the side of the train (in this case, the outer side) shows a more rapid boundary layer growth than the train roof.

g) Turbulence intensities for the roof of the train show higher values for the 1st carriage and then decrease considerably.

h) Turbulence intensities for the outer side of the train show higher values again in the inter-carriage gaps.

i) Wavelet analysis of the individual runs at different heights along the train outer side show how the small scale turbulence in the boundary layer is firstly located on the top right corner of the train for the first carriage and then moves down to train mid height when reaching the fourth carriage.

4. In the near wake region:

a) The rotating rail results show a difference in wake structure before and after a distance of 10 vehicle heights downstream the vehicle trailing edge. This confirms the near wake and far wake regions division described in Baker (2001).

b) Full scale measurements (experimental and CFD) corroborate the existence of helical vortices in the train near wake. These vortices undergo some sort of regular oscillation with the major unsteadiness at Strouhal numbers of 0.1-0.15 being dominant close to the ground. However, for model scale tests (for both the rotating rig and the TRAIN rig) , the wavelet investigation of the turbulence scales in the near wake region suggests a peak at a Strouhal number of around 0.5-1, taken to be due to shear layer instability. As the model measurements were made higher up the train than the full

scale measurements, it may be that the unsteady helical vortex motion is more important close to the ground, and other types of unsteadiness higher up the vehicle. This indicates the complexity of the wake flow.

c) The near wake slipstream velocity peak mentioned in Sterling, Baker et al. (2001) is also present in the ensemble average velocity results all along the side and roof of the train.

d) As in previous full scale and model scale tests (Sterling, Baker et al. 2001), it is found that this peak is an intermittent structure which puts in doubt the use of the ensemble averaging technique in this region.

5. In the far wake region:

   a) It is also found, as for the TRAIN results, that low frequency oscillations at Strouhal numbers of around 0.03 persist downstream of the train, which indicates the large scale structure of the far wake region. CFD results also showed the existence of this lower frequency oscillation. Baker (2001) found that this oscillation is either associated with the mechanism of wake pumping, or with large-scale instability of the complete wake structure.

6. The model scale results duplicate the main features of the wake flow field. Given the height of the train and the train-wheel speed, the flow structures in the wake of the rotating train are not as apparent as those found for full scale tests or at model scale in the TRAIN rig (i.e. vortices found in the rotating rig do not show defined streamwise cores of concentrated vorticity). However, the near wake flow results show a velocity peak of intermittent nature, as found for both model and full scale tests. Furthermore, shear layer instability is also present in the near wake region with major unsteadiness at Strouhal numbers of around 0.5-1 at train mid height (as seen in the wavelet power spectrum of the

results). Although at full scale tests this unsteadiness is found at St of 0.1-0.15 and closer to the ground, this only shows the complexity of the wake structure, and might reflect as well the Reynolds number effect on the boundary layer development, and later separation, at model and full scale tests. In terms of the far wake region, the wavelet analysis results, similarly to previous full scale and model scale tests, also show a low frequency oscillation at a Strouhal number of 0.03 indicating the large-scale instability of the complete wake structure.

7. The effect of each inter-carriage gap on the pressure distribution could be identified as a series of spikes in the ensemble-average pressure coefficient time histories (see figures 38 and 39). For outer side measurements the effect of the gaps was stronger close to the roof of the train, whilst for the inner side measurements the effect was stronger close to the platform. For roof measurements only the effect of the first inter-carriage gap was visible. The CFD simulations of Hemida et al. (2010) showed that the influence of the under-body of the train on the pressure distribution was higher than that of the inter-carriage gaps, especially close to the ground.
8. As seen in previous studies (Baker, Dalley et al., 2001; Sterling, Baker et al., 2008) the effect of model speed on the experimental results is small if the results are properly normalized.
9. The rig provided 80 laps at quite a short period of time (below 1min for wheel speeds of 16.5m/s), showing again the great advantage of the rig against conventional methods.
10. There is however the issue of an actual wind offset of around 0.08 of the wheel velocity that seems to be the result of an ongoing airflow produced both by the train and the movement of the wheel.

11. Another issue to be taken into account is the mismatch of the Reynolds number between model scale and full scale tests. The Reynolds number for the model scale tests of a $1/50^{th}$ scale model of an idealised four carriage ICE2 train in the rotating rig is 0.58×10^6 (taking V = 16.5 m/s and L = 0.525 m) whilst for the full scale ICE1 service train used in the tests carried out by DB, the Reynolds number is 88.4×10^6 (taking V = 51 m/s and L = 26m). This considerable difference in Reynolds number is apparent in the results when comparing full scale and model scale data, as shown in Chapter 5. The boundary layer development is highly dependent upon Reynolds number, which in turn has an impact in the wake behaviour, since the near wake oscillations are determined to some degree by the nature of the separated boundary layer in the wake. To ensure that model scale results are representative of the full scale scenario, the difference in Reynolds number/scale should be minimised as much as possible. Following Schetz (2001), tests should not be conducted at much less than $1/10^{th}$ scale, which in the case of the rotating rig implies using a train almost as long as the perimeter of the wheel and therefore invalid for the tests, so a bigger rig should be sought. CEN (2009) states that the Reynolds number has to be larger than 0.25×10^6 to ensure that values for normalised mean velocity values (over all measured velocity maxima) plus two standard deviations are representative of full scale. In order to do so, the normalised mean velocity values plus two standard deviations should be demonstrated Reynolds number independent in the range $0.6\,Re_{max}$ to Re_{max} within ± 3%. This requirement implicitly specifies the model scale.
12. Overall, the results obtained from the rotating rig measurements are in good agreement with the full scale measurements and reproduce all the important flow features.

These conclusions lead to the following suggestions for further work.

1. The need to understand further the effects on the results introduced by the curvature of the rig, makes it necessary to carry out a series of CFD calculations for larger track and model radii, including also the modelling of the straight track. The results for the different curvatures can then be compared, which should enable a judgement to be made concerning the minimum radius of such a rig that will enable the slipstream results obtained to be representative of the full scale situation and thus to make recommendations for the design of a larger more representative rig that retains the utility of being able to simulate many train passes rapidly whilst being more representative of reality.
2. Probably a bigger rig will remove the wind offset present in this experiment, which affects both the measured velocities and the nose peak location.
3. A bigger rig would be suitable for a bigger train, which would help to increase the Reynolds number of the tests, bringing it closer to that of the full scale scenario. Following Schetz (2001) a rig suitable for a model scale of at least $1/10^{th}$ should be pursued. This would give a minimum $Re = 2.88 \times 10^6$ (with V = 16.5 m/s).
4. The use of CFD will also help to shed some light there where the experimental measuring apparatus (such as the probes for the present investigation) fails to provide information (i.e. flow separation close to the nose area and influence of the under-body on the pressure distribution).
5. It might be useful also to develop a rotating rig in which higher velocities can be tested so that the probes can be working within their working range and not at their very bottom limit. This will help increase the probe's acceptance data percentage.
6. Although increasing the speed, could bring again the issue of the ongoing airflow and different solutions should be sought to remove it.

7. In order to increase the acceptance data percentage in the nose area, different probe arrangements should be tried, i.e. at 45° - 90° to the direction of travel. However this would imply the use of different probes, with different alignments, so that the different flow regions can be adequately captured. Then data from the different probes should be brought together to create a single slipstream velocity figure.
8. The boundary layer development is different at model scale than at full scale, due to Reynolds number effects. More work needs to be done in this area in order to assess the Reynolds number effects on boundary layer development.
9. Although the rig results duplicate the main features of the wake flow field, the nature of the oscillations found in this region are determined to some degree by the nature of the separated boundary layer in the wake, and the boundary layer development is different at model scale than at full scale. Therefore, more work is needed in this area to understand better the effect of the boundary layer development in the wake behaviour.

REFERENCES

Anderson, J., Pettersson, V., Thune, E., Viktorsson, H., and Oisjoen, D. (2009). Simulation of the Slipstream and wake of a High-Speed Train in Crosswinds. Bachelor's Thesis. Department of Applied Mechanics. Chalmers University of Technology.

ANSYS, Inc.(2009). Ansys Fluent 12.0/12.1 Documentation [online]. Available from https://www.sharcnet.ca/Software/Fluent12/index.htm. [Accessed 19th March 2009].

Baker, C. J. (2001). "Flow and dispersion in ground vehicle wakes." Journal of Fluids and Structures **15**: 1031-1060.

Baker, C.J. (2010). "The flow around high speed trains". Journal of Wind Engineering and Industrial Aerodynamics, **98**: 277-298.

Baker, C. J., Dalley, S. J., Johnson, T., Quinn, A., and Wright, N. G. (2001). "The Slipstream and Wake of a High Speed Train," Proceedings of the Institution of Mechanical Engineers F, Journal of Rail and Rapid Transit, **215**: 83-99

Baker, C. J., M. Sterling, et al. (2004). The Slipstreams and Wakes of Ground Vehicles. Proceedings of the Bluff Body Aerodynamics and its Applications Conference, Ottawa.

Baker, C.J., Sterling, M., Figura-Hardy, G.I., Johnson, T., Free, P., Munley, G., Bowman, I., Pope, C., and Gawthorpe, R. (2006). The effect of train slipstreams on passengers and trackside workers. Proceedings of the 7th World Congress on Railway Research, Monteral.

Basara, B. (2000). Computations of automotive flows using the second moment closure. European Congress on Computational Methods in Applied Sciences and Engineering, Barcelona.

Barlow, R. S. and J. P. Johnston (1988). "Structure of a turbulent boundary layer on a concave surface." Journal of Fluid Mechanics Digital Archive **191**(-1): 137.

Bearman, P. W. (1997). "Near wake flows behind two and three dimensional bluff bodies." Journal of Wind Engineering and Industrial Aerodynamics **69-71**: 33-54.

Bearman, P. W. and E. D. Obasaju (1982). "An experimental study of pressure fluctuations on fixed and oscillating square-section cylinders." Journal of Fluid Mechanics **119**: 297-321.

Bearman, P. W. and D. M. Trueman (1972). "An Investigation of the Flow Around Rectangular Cylinders." Aerodynamics Quarterly **23**: 229-237.

Belotserkovskii, O. M. (2004). Turbulence: New Approaches, Cambridge International Science Publishing.

Bradshaw, P. (1969). "Analogy between streamline curvature and bouyancy in turbulent shear flow." Journal of Fluid Mechanics **36**(pt 1): 177-191.

Bradshaw, P. (1973). "Effects of streamline curvature on turbulent flow." AGARDograph **169**.

Cebeci, T. and A. M. O. Smith (1974). Analysis of turbulent boundary layers, New York, Academic Press, Inc. (Applied Mathematics and Mechanics, No. 15).

CEN 2009. Railway applications – Aerodynamics – Part 4: Requirements and test procedures for aerodynamics on open track, CEN EN 14067-4:2005+A1.

Chen, J., B. S. Haynes, et al. (2000). "Cobra Probe Measurements of Mean Velocities, Reynolds Stresses and Higher-Order Velocity Correlations in Pipe Flow." Experimental Thermal and Fluid Science **21**: 206-217.

Duncan, W. J., A. S. Thom, et al. (1970). Mechanics of fluids, London: Edward Arnold.

De Guzman, M. M., C. A. J. Fletcher, et al. (1994). "Computational Investigation of Cobra Probe Operation." International Journal of Numerical Methods for Heat and Fluid Flow **4**: 425-445.

Department for Transport. (2012). High Speed Rail: Investing in Britain's Future-Decisions and Next Steps.

Doshi, M.R., and Gill, W.N. (1970). "A note on the mixing length theory of turbulent flow". AIChE Journal, **16**(5): 885-888.

Eskridge, R. E. and J. C. R. Hunt (1979). "Highway Modeling. Part I: Prediction of Velocity and Turbulence Fields in the Wake of Vehicles." Journal of Applied Meteorology **18**(4): 387-400.

Eskridge, R. E. and R. S. Thompson (1982). "Experimental and Theoretical Study of the Wake of a Block-Shaped Vehicle in a Shear-Free Boundary Flow." Atmospheric Environment **16**(12): 2821-2836.

EU 2008. Technical Specification for Interoperability Relating to the 'Rolling Stock' Sub-System of the Trans European High-Speed Rail System (HS RST TSI), 2008/232/EC.

Farge, M. (1992). "Wavelet Transforms and Their Applications to Turbulence." Annu. Rev. Fluid Mech., **24**: 400-450.

Figura-Hardy, G. (2007). RSSB Slipstream Safety-Analysis of existing experimental data on train slipstreams including the effects on pushchairs. RSSB.

Gatski, T.B., Hussaini, M. Y., Lumley, J.L. and John, L. (1996) Simulation and Modelling of turbulent flows. Oxford University Press.

Gilhome, B. R., J. W. Saunders, et al. (2001). "Time Averaged and Unsteady Near-Wake Analysis of Cars." Vehicle Aerodynamics and Technology **SP-1600, SAE 2001-01-1040**: 191-208.

Gretler, W. and M. Baltl (2000). "Numerical calculation of fully developed turbulent flow in curved channels: An extended algebraic Reynolds-Stress model." Forschung im Ingenieurwesen. **66**: 138-146.

Griffin, O. M. (1981). "Universal Similarity in the Wakes of Stationary and Vibrating Bluff Structures." Journal of Fluids Engineering, **103**: 52-58

Hemida, H., Gil, N., Baker, C. (2010). "LES of the Slipstream of a Rotating Train." Journal of Fluids Engineering. **132**.

Hemida, H., and Krajnovic, S. (2008). "LES Study of the Influence of a TrainNose Shape on the Flow Structures Under Cross-Wind Conditions." ASME Journal of Fluids Engineering, **130** (9): 091101.

Hemida, H., and Krajnovic, S. (2009). "Exploring Flow Structures Around a Simplified ICE2 Train Subjected to a 30° Side Wind Using LES." Engineering Applications of Computational Fluid Mechanics, **3**(1)**:**28–41.

Hemida, H., and Krajnovic, S. (2010). "LES Study of the Influence of Yaw Angles and Nose Shape on Flow Structures Around Trains," J. Wind Eng. Ind.Aerodyn., **98**(1): 34–46.

Higgins, M. (2003). "Laboratory and On-Track Testing of 'Laserthor' Railhead Cleaner," Railway Safety Research Programme, RSSB.

Hinze, J. O. (1976). Turbulence, New York; London (etc.): McGraw-Hill.

Hoffmann, P. H., K. C. Muck, et al. (1985). "The effect of concave surface curvature on turbulent boundary layers." Journal of Fluid Mechanics Digital Archive **161**(-1): 371.

Holloway, A. G. L. and S. Tavoularis (1992). "The effects of curvature on sheared turbulence." Journal of Fluid Mechanics **237**: 569-603.

Hooper, J. D. and A. R. Musgrove (1997). "Reynolds Stress, Mean Velocity, and Dynamic Static Pressure Measurement by a Four-Hole Pressure Probe." Experimental Thermal and Fluid Science **15**: 375-383.

Johnson, T., Dalley, S., and Temple, J. (2004). *"Recent Studies of Train Slipstreams. In The Aerodynamics of Heavy Trucks, Buses and Trains. Series: Lecture Notes in Applied and Computational Mechanics,"* **19**, Springer-Verlag, Berlin.

Johnson, T., and Dalley, S. (2002). 1/25 scale moving model test for the TRANSAERO Project. *Notes on Numerical Fluid Mechanics*, **79**, Springer-Verlag, Berlin.

Johnson , T. and Holding, J. (2003). Better understanding of high speed train slipstream velocities. World Congress on Railway Research, Edinburgh, UK.

Jordan, S.C. (2008). An investigation of the slipstream and wakes of trains and the associated effects on trackside people and objects. PhD thesis, University of Birmingham, Uk.

Jordan, S., Johnson, T., Sterling, M., and Baker, C. (2008). "Evaluating and modelling the response of an individual to a sudden change in wind speed." Build. Environ, **43**(9): 1521-1534.

Jordan, S., Sterling, M., and Baker, C. J. (2009). "Modelling the response of a standing person to the slipstream generated by a passenger train." Proceedings of the Institution of Mechanical Engineers, Part F: Journal of Rail and Rapid Transit, **223**(6):567-579.

Kim, N. and D. L. Rhode (2000). "Streamwise Curvature Effect on the Incompressible Turbulent Mean Velocity Over curved surfaces." Journal of Fluids Engineering **122**: 547-551.

Lakshminarayana, B. (1986). "Turbulence Modeling for Complex Shear Flows." AIAA Journal **24**: 1900-1917.

Lawson, N.J, Garry, K.P., and Faucompret, N. (2007). An investigation of the flow characteristics in the bootdeck region of a scale model notchback saloon vehicle. Proceedings of the Institution of Mechanical Engineers, Part D: Journal of Automobile Engineering. **221**: 739. DOI: 10.1243/09544070JAUTO155.

Lee, W. W., and Davis, R.T. (1972). "Laminar boundary layers on moving continuous surfaces." Chemical Engineering Science, **27**(12):2129-2149.

Lyn, D. A. and W. Rodi (1994). "The flapping shear layer formed by flow separation from the forward corner of a square cylinder." Journal of Fluid Mechanics **267**: 353-376.

Lyn, D. A., W. Rodi, et al. (1995). "A laser-Doppler velocimetry study of ensemble-averaged characteristics of the turbulent near wake of a square cylinder." Journal of Fluid Mechanics **304**: 285-319.

Pope, C.W., Baker, C.J., Bowman, N.R., and N'Kaoua, J. (2006). Safety of slipstream effects produced by Trains: Pilot CFD analysis of the effect of crosswinds on train slipstreams. MIRA Vehicle Aerodynamics Conference

Majumdar, S., W. Rodi, et al. (1992). "Three Dimensional Finite Volume Method for Incompressible Flows with Complex Boundaries." Journal of Fluids Engineering **114**: 496-503.

Mathworks, Inc. (2008) Butterworth Filter [online]. Available from http://www.mathworks.es/help/toolbox/signal/ref/butter.html [Accessed 17th October 2008]

Meroney, R. N. and P. Bradshaw (1975). "Turbulent Boundary Layer Growth Over a Longitudinally Curved Surface." AIAA Journal **13**(11): 1448.

Mousley, P. and S. Watkins (2000). "A Method of Flow Measurement About Full-Scale and Model-Scale Vehicles." Society of Automotive Engineers **SP-1524**: 263-271.

Muck, K. C., P. H. Hoffmann, et al. (1985). "The effect of convex surface curvature on turbulent boundary layers." Journal of Fluid Mechanics Digital Archive **161**(-1): 347.

Muld, W. (2010). Analysis of Flow Structures in Wake Flows for Train Aerodynamics. Academic Dissertation. Royal Institute of Technology. Department of Mechanics

Muld, T., Efraimsson, G., Henningson, D., Herbst, A., and Orellano, A. (2009). Detached Eddy Simulation and Validation on the Aerodynamic Train Model. EUROMECH Colloquium, Berlin, Germany.

Polikar, R. (2001). Wavelet tutorial [online]. Rowan Uniersity. Available from http://users.rowan.edu/~polikar/WAVELETS/WTutorial.html [Accessed 20th November 2008].

Pope, S. B. (2000). Turbulent Flows, Cambridge University Press.

Pope, C. (2006). Safety of slipstreams effects produced by trains. A report prepared by Mott Macdonald, Ltd., for RSSB.

Quinn, A.D., Baker, C.J., Sterling, M., Sima, M., Weise, M., Hoefener, L., and Eisenlauer, M. (2011). The effect of cross winds on the slipstreams of high speed trains. Proceedings of the 13th International Conference on Wind Engineering, Amsterdam.

Quinn, A.D., Hayward, M., Baker, C.J., Schmid, F., Priest, J.A., and Powrie, W. (2010). "A full-scale experimental and modelling study of ballast flight under high-speed trains." Proceedings of the Institute of Mechanical Engineers, Part F: Journal of Rail and Rapid Transit, **224**, 61.

Rayney, D. (2011). The application and Effect of the Rayleigh Wave Speed Principle on High Speed Rail Travel. Written Evidence. Transport Committee, House of Commons.

Rodi, W. (1997). "Comparison of LES and RANS calculations of the flow around bluff bodies." Journal of Wind Engineering and Industrial Aerodynamics **69-71**: 55.

Schetz, J. A. (2001). "Aerodynamics of High-Speed Trains." Annu. Rev. Fluid Mech. **33**: 371-414.

Schulte-Werning, B., C. Heine, et al. (2003). "Unsteady wake flow characteristics of high speed trains." Proc. Appl. Math. Mech. **2**(1): 332-333.

Schulte-Werning, B., Matschke, G., Gregoire, R., and Johnson, T. (1999). "RAPIDE: A project of Joint Aerodynamics Research of the European High-Speed Rail Operators," World Congress on Railway Research, Tokyo.

Shaw, C.T., Garry, K.P., and Gress, T. (2000). Using singular systems analysis to characterise the flow in the wake of a model passenger vehicle. Journal of Wind Engineering and Industrial Aerodynamics. **85**: 1-30.

Shui-Hong Lee, H. (1999). Assessment of potential aerodynamic effects on personnel and equipment in proximity to high-speed train operations. Report for the U.S.Department of Transportation. DOT-VNTSC-FRA-98-3.

So, R. M. C. (1975). "A turbulence velocity scale for curved shear flows." Journal of Fluid Mechanics. **70, part1**: 37-57.

So, R. M. C. and G. L. Mellor (1973). "Experiment on convex curvature effects in turbulent boundary layers." Journal of Fluid Mechanics. **60**: 43-62.

Sodja, J. (2007). Turbulence models in CFD. Report. University of Ljubljana. Department of physics.

Sterling, M., Baker, C.J., Jordan, S. C., and Johnson, T.A. (2008). "A Study of the Slipstreams of High Speed Passenger trains and freight trains." Proceedings of the Institution of Mechanical Engineers F: Journal of Rail and Rapid Transit, **222:** 177-193.

Taylor, G. I. (1936). "Fluid Friction between Rotating Cylinders. II. Distribution of Velocity between Concentric Cylinders when Outer One Is Rotating and Inner One Is at Rest." Proceedings of the Royal Society of London. Series A, Mathematical and Physical Sciences **157**(892): 565-578.

Temple, J., and Johnson, T. (2003). Review of Slipstream Effects on Platforms. AEA Technology Rail report for RSSB.

Torrence, C. and Compo, G.P. (n.d.) Wavelets [online]. Department of Atmospheric and Oceanic Sciences: University of Colorado Boulder. Available from http://atoc.colorado.edu/research/wavelets/ [Accessed 11th November 2008].

Torrence, C. and Compo, G.P. (1998). "A practical guide to wavelet analysis." Bull. AM. Met. Soc. **79** (1): 61-78.

Townsend, A. A., Ed. (1976). The structure of turbulent shear flow, Cambridge University Press.

Turbulent Flow Instrumentation Pty Ltd. (n.d.) Cobra Probe [online]. Available from http://turbulentflow.com.au/Products/CobraProbe/CobraProbe.php#CobraOperation [Accessed 21st February 2008].

Valens, C. (1999). A Really Friendly Guide to Wavelets [online]. Available from http://pagesperso_orange.fr/polyvalens/Clemens/wavelets/wavelets.html [Accessed 25th November 2008].

Versteeg, H. K. and W. Malalasekera (1995). Introduction to computational fluid dynamics: the finite volume method, Harlow: Longman.

Watkins, S., Mousley, P., & Hooper, J.D. (2002). Measurement of fluctuating flows using multi-hole probes. Proceedings of the 9th International Congress of Sound and Vibration, Orlando, Florida, USA, 8-11 July, International Institute of Acoustics and Vibration (IIAV).

APPENDICES

Two papers are included in this section.

1. Gil, N., Baker, C.J., Roberts, C., and Quinn, A. (2010). "Passenger train slipstream characterization using a rotating rail rig" Journal of Fluids Engineering. **132(6)**, 061401.
2. Hemida, H., Gil, N., and Baker, C.J. (2010). "LES of the slipstream of a rotaring train." Journal of Fluids Engineering. **132(5),** 051103.

The first paper, written by the author of this thesis, presents most of the model scale train slipstream results obtained with the rotating rail rig. These results have been included in Chapter 4 of the present document.

The second paper details the Large Eddy Simulation of the slipstream of the model scale train of the current investigation. The role of the author of this thesis in this paper was to provide the rig test results that served as comparison for the LES results. Results from this paper have been used in Chapter 6.